

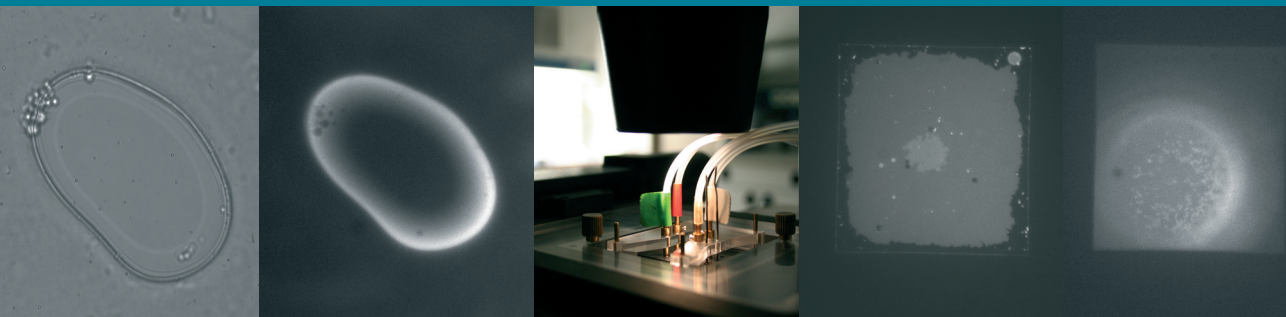
# Nanopore Modifications with Lipid Bilayer Membranes for Optical Tweezers DNA Force Measurements

## Dissertation

*submitted in partial fulfillment of the requirements for the degree of  
Doktor der Naturwissenschaften (Dr. rer. nat.) by*

**Lukas Galla**

*Faculty of Physics  
Bielefeld University  
April 2015*



# **Nanopore Modifications with Lipid Bilayer Membranes for Optical Tweezers DNA Force Measurements**

---

## **Dissertation**

*submitted in partial fulfillment of the requirements for the degree of  
Doktor der Naturwissenschaften (Dr. rer. nat.) by*

**Lukas Galla**

*Faculty of Physics  
Bielefeld University  
April 2015*

*„Die Neugier steht immer an erster Stelle eines  
Problems, das gelöst werden will.“*

---

(Galileo Galilei)

# Erklärung

---

Hiermit erkläre ich,

1. dass mir die geltende Promotionsordnung der Fakultät für Physik der Universität Bielefeld bekannt ist.
2. dass ich die vorliegende Dissertation selbst angefertigt, dabei keine Textabschnitte von Dritten oder eigener Prüfungsarbeiten ohne Kennzeichnung übernommen und alle von mir benutzten Hilfsmittel und Quellen in der Arbeit angegeben habe.
3. dass Dritte weder unmittelbar noch mittelbar geldwerte Leistungen von mir für Vermittlungstätigkeiten oder für Arbeiten erhalten haben, die im Zusammenhang mit dem Zustandekommen oder dem Inhalt dieser vorliegenden Dissertation stehen.
4. dass ich diese vorliegende Dissertation oder wesentliche Teile davon nicht als Prüfungsarbeiten für eine staatliche oder andere wissenschaftliche Prüfung eingereicht habe.
5. dass ich die gleiche, eine in wesentlichen Teilen ähnliche oder eine andere Abhandlung nicht bei einer anderen Hochschule als Dissertation eingereicht habe.

Eingereicht am: 14. April 2015

*Lukas Galla*

# Referees

---

**PROF. DR. DARIO ANSEMETTI**

*Experimental Biophysics and Applied Nanoscience*

Faculty of Physics, Bielefeld University

**PROF. DR. ANDREAS HÜTTEN**

*Thin Films and Physics of Nanostructures*

Faculty of Physics, Bielefeld University

## Abstract

---

Driving small molecules, such as DNA, electrophoretically through a nanometre-sized pore provides single-molecule sensitivity and analytical properties (e.g. sequencing) without prior molecular amplification and necessity for labeling. Theoretical and experimental investigations indicate that the forces, which contribute to this translocation process, depend on an interplay of ionic screening and hydrodynamics. Therefore, it is of essential importance to study and characterize these threading forces to gain a deeper understanding of the underlying mechanisms.

Utilizing optical tweezers, the experimental results presented here have expanded the force measurements in solid-state nanopores to include a surface modification by a lipid bilayer coating. It was demonstrated that the DNA threading forces increased by 80 % compared to an uncoated nanopore of the same size. Thus, these findings led to a more comprehensive theoretical description of polyelectrolyte dynamics in the highly confined environment of a nanopore.

In addition, a fundament of preparation techniques was explored and established, to demonstrate that it is possible to produce nanopore-spanning and thus, freestanding lipid bilayer membranes. It was shown that these lipid bilayers were stable for hours and suitable for the incorporation of  $\alpha$ -hemolysin (a pore-forming protein). Furthermore, free translocation experiments with DNA-oligomers through this biological pore were conducted successfully. Based on this technological fundament, it will be feasible to conduct optical tweezers threading force measurements on these biological pores, in order to provide prospective influential insights, as well as additional contributions to an unambiguous theoretical model.

# Contents

|          |  |            |
|----------|--|------------|
| <b>1</b> | <b>Introduction and Motivation</b>                         | <b>1</b>   |
| <b>2</b> | <b>Background and Theory</b>                               | <b>5</b>   |
| 2.1      | Biomolecules.....  | 5          |
| 2.1.1    | DNA .....  | 5          |
| 2.1.2    | Proteins and Biological Pores .....                        | 7          |
| 2.1.3    | Lipids and Lipid Bilayer Membranes.....                    | 11         |
| 2.2      | Langmuir-Blodgett Films.....                               | 14         |
| 2.3      | Optical Trap.....  | 16         |
| 2.4      | Fluorescence Detection.....                                | 20         |
| 2.5      | Nanopores.....   | 21         |
| 2.6      | DNA-Nanopore Force Interaction.....                        | 26         |
| 2.6.1    | Experimental DNA Threading Force Measurement.....          | 26         |
| 2.6.2    | Theoretical Dynamics of DNA in a Solid-State Nanopore..... | 30         |
| <b>3</b> | <b>Materials and Methods</b>                               | <b>33</b>  |
| 3.1      | Chemicals and Materials.....                               | 33         |
| 3.2      | Experimental Setup.....                                    | 35         |
| 3.2.1    | Optical Tweezers.....                                      | 35         |
| 3.2.2    | Fluorescence Microscopy.....                               | 38         |
| 3.3      | Nanopore Modification.....                                 | 39         |
| 3.3.1    | Preparation of Lipid-Coated Nanopores.....                 | 39         |
| 3.3.2    | Langmuir-Blodgett Transfer.....                            | 41         |
| 3.3.3    | Giant Unilamellar Vesicles.....                            | 44         |
| 3.3.4    | Ionovation Bilayer Slide.....                              | 45         |
| <b>4</b> | <b>Results and Discussion</b>                              | <b>49</b>  |
| 4.1      | Lipid Bilayer-Coated Nanopores.....                        | 49         |
| 4.1.1    | Characterization of Coated Nanopores.....                  | 50         |
| 4.1.2    | DNA-Threading Experiments with Lipid-Coated Nanopores..... | 57         |
| 4.2      | Pore-Spanning Freestanding Lipid Bilayer Membranes.....    | 63         |
| 4.2.1    | Langmuir-Blodgett Monolayer Transfer.....                  | 63         |
| 4.2.2    | Bursting of Giant Unilamellar Vesicles.....                | 68         |
| 4.2.3    | Ionovation Bilayer Slide.....                              | 85         |
| <b>5</b> | <b>Summary and Outlook</b>                                 | <b>93</b>  |
|          | <b>Bibliography</b>  | <b>97</b>  |
|          | <b>Acknowledgments</b>                                     | <b>111</b> |
|          | <b>Appendix</b>  | <b>113</b> |

# 1 Introduction and Motivation

---

Biophysics is an interdisciplinary research field, where biological issues about life in its variety and complexity are studied by physical and mathematical laws providing detailed predictions about mechanisms that drive idealized biological systems. Therefore, numerous physical techniques are developed and utilized to measure diverse properties, such as mechanical forces, electric charges, ion currents, binding and decay rates and optical, electromagnetic or acoustical spectra. Unlike other scientific fields, biophysics is mostly based on an inductive approach, i.e. the study of single specific details in order to expand upon a valid theory that can then be transferred to increasingly complex structures, leading to an overall understanding. One specific detail within this complex field is (e.g.) the investigation of single molecules to minimize or prevent disturbing influences on ensemble data.

One molecule of particular interest is deoxyribonucleic acid (DNA), which forms the genome and provides the blueprint for all organisms<sup>[1]</sup>. The capability to swiftly and precisely gain knowledge about DNA composition is crucial to many biological sciences<sup>[2]</sup>. Since a new era of synthetic genomics and personalized medicine is currently underway, the demand for highly efficient DNA sequencing technologies is rising. Straightforward decoding of genetic material will shed light on uncharted biological functions and phenotypic variations. Thus, metagenomic endeavors<sup>[3,4]</sup> are enabling new methods in genetic engineering and thereby, in turn, providing the creation of artificial life in the service of humanity<sup>[2]</sup>. Such future synthetic organisms may pave the way for systems capable of absorbing excessive carbon dioxide from the atmosphere or for generating petrol substitutes<sup>[2]</sup>. In addition, sequencing human, bacterial and viral genomes at economic conditions, would lead to a quantum leap in health care systems due to improved diagnosis, understanding and treatment of diseases<sup>[5]</sup>. There are many aspects that need to be taken into account in DNA sequencing, such as read length, bases per second and raw accuracy when discussing the methodology<sup>[2]</sup>. Sanger sequencing (introduced in 1977) is one of the most seminal inventions in the field of biology<sup>[6]</sup>. The evolution of this technique (nearly 25 years later) resulted in alternative approaches that utilize bioluminescence sequencing by synthesis<sup>[7]</sup>. At present, there exist a variety of sequencing techniques, each with their own benefits and disadvantages. Even though this short read, high-throughput, next generation sequencing techniques has transformed our understanding of microbiology<sup>[8]</sup>, they all require extensive biochemical labeling as well as sample preparation and even more importantly, they do not support long read lengths<sup>[9,10]</sup>. Therefore, DNA sequencing by the fast growing field of nanopore (NP) technology can be an alternative method for producing long-read sequence data<sup>[11,12]</sup>.

Certainly, nearly everyone knows of the struggle to thread a yarn through the eye of a needle. As a matter of fact, it is even more difficult, if the needle's eye is as small as a thousandth part of a single human hair and the thread is a single DNA strand. This image by Decker<sup>[13]</sup> illustrates the dimensions which are involved in context of translocation through an nanometre-sized pore. The NP approach provides single-molecule sensitivity and analytical properties that are achieved by driving molecules electrophoretically through a NP without prior molecular amplification and necessity

for labeling<sup>[11,14,15]</sup>. The basic functioning can be described as a coulter counter system, where two chambers, containing aqueous electrolytes, are separated by an insulating membrane and are only connected by the NP. When a voltage is imposed across such a NP, which offers a highly confined channel structure, the resulting ionic current can be measured and the translocation of single nucleic acid polymers can be studied at high throughput<sup>[11,15]</sup>. By an even deeper insight, it should also be feasible to detect DNA in such a way that the sequence of obtained signals reflects the native order of nucleobases in a polynucleotide<sup>[11]</sup>. In addition, the prediction of long reads of (kilobase length) polymers provides a unique analytical capability that makes inexpensive, rapid DNA sequencing possible and offers the prospect of a next generation technique that will be able to sequence a diploid mammalian genome for ~ \$ 1 000 in about 24 h<sup>[11]</sup>. Therefore, the NP-based technology has the potential to revolutionize the basic research and clinical medicine, as well as to tap into new sectors of customers who need genetic fingerprinting for food safety, forensic science or agricultural biotechnology<sup>[5,9]</sup>.

In general NPs can be classified into two categories: solid-state NPs and biological NPs. The key difference is the presence of a pore forming structure versus only the opening itself. Solid-state NPs are mostly based on artificial membranes made of varying materials, such as silicon, silicon-nitride, silicon-dioxide or new 2D-materials<sup>[16]</sup>, like graphene, molybdenum disulfide or carbon nanomembranes. In this context, the NP represents an absence of material in a highly confined volume, creating a hole or channel structure. In contrast to this, biological NPs are very small specific shaped objects (most commonly proteins), which exhibit a natural channel structure, and thus in turn have to be incorporated into membrane systems (such as lipid bilayer membranes or artificial membranes). The application of the pore-forming *Staphylococcus aureus* toxin  $\alpha$ -hemolysin as a biosensor was pioneered by Bayley and colleagues<sup>[11,17]</sup> and has become the protein of choice for this type of research<sup>[13]</sup>. In 1996 Kasianowicz et al. reported the first demonstration of the transit of nucleic acids through such an  $\alpha$ -hemolysin pore<sup>[18]</sup>, followed by hosts of publications, where many aspects of this translocation process were examined in detail<sup>[19–24]</sup>. The new field of engineered protein pores or DNA-origami pores is an additional driving force for the further development of biological NPs<sup>[25–27,28]</sup>.

As described so far, sequencing polynucleotides with NPs promises exciting potential advantages, however, the encoding of the base sequence has been hampered by the high translocation velocity together with the effect that the recorded signal is influenced by several nucleotides<sup>[9,11,29]</sup>. Several approaches have been made to slow down translocation speeds, such as the utilization of DNA hairpin structures, protein attachment to one end of the DNA<sup>[22,30,31]</sup> or the theoretical explored translocation by thermophoresis<sup>[32]</sup>. In 2010, the Akeson group<sup>[33]</sup> presented the use of DNA polymerase that drives a DNA template through a NP in single-nucleotide steps as DNA is synthesized. This concept was further developed by Cherf et al.<sup>[34]</sup> and Manrao et al.<sup>[35]</sup> in 2012. In these studies, the authors independently showed that information about the sequence can be acquired by the use of *phi29 DNA polymerase* to slow DNA translocation to a speed that is sufficient to reading base-specific current levels. Currently, the company Oxford Nanopore Technologies is pushing this concept even further and into commercialization by two NP sequencing platforms (GridION and

MinION), delivering high-throughput and ultra-long sequence reads at low costs<sup>[36]</sup>. Even though there is still a need for further improvements (especially increasing the relative high error rates)<sup>[37]</sup>, Ashton et al. and Ammar et al. presented data showing that it is feasible to resolve the structure and chromosomal insertion site of a composite antibiotic resistance island in haplotypes<sup>[12]</sup> as well as encode two specific genes variants and haplotypes<sup>[38]</sup>. This was achieved by a single 24 h sequencing run of the MinION sequencer and without the necessity for statistical phasing.

It is noteworthy, that developments in the field of optical sensing methods<sup>[39]</sup> and glass capillaries for NP sensing are also in progress and may provide additional positive impact to this research field<sup>[40-42]</sup>. In addition, the recently introduced graphene NPs also present an intriguing alternative to biological and “*conventional solid-state*” NPs, because with its thickness of only a single carbon atom graphene is the ultimate NP membrane material<sup>[43-45]</sup>.

As introduced, several different scientific disciplines contribute to the field of NP research, each of them specified in another detail. The wide variety of experimental studies analyzing DNA translocation through NPs has progressively led to the need for a fundamental understanding of the translocation process<sup>[13]</sup>. In order to characterize this mechanism, the magnitude of the involved force is of essential importance<sup>[46]</sup>. These forces play a significant role in biological polymer transport, e.g. in gene transfer between bacteria and transport of RNA through nuclear membranes<sup>[46]</sup>. Theoretical and experimental investigations of the physics of electrophoresis indicate that the involved forces depend on an interplay between ionic screening and hydrodynamics<sup>[47]</sup>. Therefore, the versatility of NPs can be particularly enhanced by their integration into optical tweezers (OT) systems, providing controlled positioning of single molecules with respect to the NP and direct monitoring of the forces acting on them<sup>[48]</sup>. The first measurements of forces acting on a single polynucleotide molecule in a solid-state NP, by a combination of optical tweezers and ion current detection, were reported in 2006 by Keyser et al.<sup>[46]</sup>. The authors showed that it was feasible to slow down and even arrest the translocation of a DNA molecule by the opposing forces generated by the utilized optical trap. For this purpose, one end of the DNA is attached to a microbead, which in turn can be trapped in a laser focus. Once the distance between such a bead-DNA complex and the NP is close enough, the DNA molecule is inserted into the pore by the voltage driven electrophoretic force and can then be measured by the partial deflection of the bead away from the trapping focus. In 2009 van Dorp et al. reported, that the stall force gradually decreased with increasing diameter of the NP<sup>[47]</sup>. This finding disagreed with the expectation governed by simple electrostatics, unambiguously demonstrating the large impact of the hydrodynamic environment.

In addition, NP-based OT studies can be utilized to detect and characterize local structures along single molecules for (e.g.) directly probing RNA secondary structures via sequential unfolding of duplex regions<sup>[48]</sup> or for studying the translocation dynamics of a single protein molecule that is attached to a double-stranded DNA<sup>[49]</sup>. In this work, Spiering et al. could show in 2011 that the observed distinct asymmetric and retarded force signals depend on the protein charge, the DNA elasticity and its counterion screening. Furthermore, the translocation dynamics reflect the stochastic

nature of thermally activated hopping between two neighboring states in the NP<sup>[49]</sup>.

Despite the aforementioned and numerous other sophisticated studies, an unambiguous theory of the hydrodynamic influences on the DNA translocation process has not been reported<sup>[47]</sup>. This problem will be addressed in this thesis by the study of NP surface modifications, using lipid bilayers and by characterizing the involved impact on optical tweezers DNA force measurements. As it was suggested by Luan et al. in 2010, the transport of DNA through a NP can be controlled by the charge state of the utilized membrane material, and thus the physical translocation mechanisms can be altered by either chemical or electrical surface modifications<sup>[50]</sup>. One possible way of such a modification by coating the NP with a fluid lipid bilayer, was reported by Yusko et al. in 2011. This study demonstrated the incorporation of mobile ligands in the bilayer and slowed the translocation speed of targeted proteins sufficiently enough to record time-resolved translocation events<sup>[51]</sup>. Nevertheless, the impact of such a coating on the electrophoretic force acting on the DNA has remained, so far, unknown. The surprising results presented in this thesis close this gap and indicate that the nanostructure of the DNA (hydrophilic phosphate groups and hydrophobic grooves) has to be taken into account for understanding the dynamics of polyelectrolytes in the highly confined environment of a NP. Additionally, these experimental findings will be described and discussed by a quantitative theoretical model (developed by Peter Reimann and Andreas J. Meyer from the *Condensed Matter Theory Group* at Bielefeld University), which incorporates a hydrodynamic slip effect on the DNA surface. The second aim of this thesis is the further development of methods for investigating and producing freestanding and stable lipid bilayer membranes that are suitable for both incorporation of biological pores and later optical tweezers measurements. Three different approaches are examined and their individual capabilities and limits are discussed.

Subsequent to this first introductory chapter, the next section recapitulates the required basic biological, physical and theoretical fundamentals followed by a summary of the utilized materials and a detailed description of the experimental setups and fabrication protocols for each approach, respectively. Finally, the experimental results are presented and discussed and a summary, including future prospects, is provided. In addition, the appendix contains a list of publications, conference participations and the authors' curriculum vitae.

## 2 Background and Theory

---

This first chapter is about the basic physical, biological and chemical background theory, which are fundamental for understanding the conducted experiments. After the description of important biomolecules the three mainly used experimental setups are introduced, followed by an overview of the investigated types of nanopores and the corresponding forces between a DNA-molecule and a nanopore.

### 2.1 Biomolecules

The biological key components used in this thesis are DNA, phospholipids and protein-pores like toxins. The following three chapters present these molecules and their special characteristics.

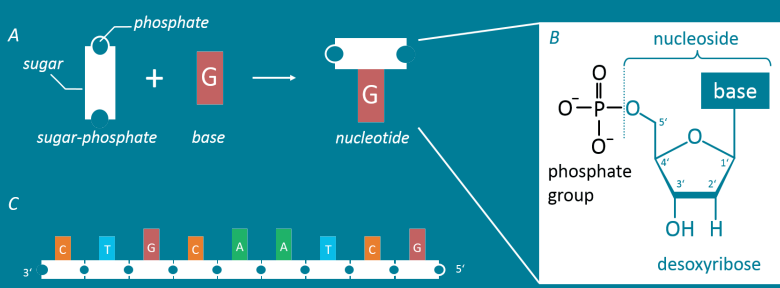
#### 2.1.1 DNA

The DNA (deoxyribonucleic acid) can be described as a cellular library. This library contains all information, which is necessary for the setting and structure of a cell or a complete organism. Classical geneticist like Gregor Mendel and Thomas Hunt Morgan identified that this huge amount of information is organized in subunits, the so-called genes<sup>[52]</sup>. In a modern working definition a gene can be described as a locatable region on a stretch of DNA, which corresponds to a unit of inheritance. This in turn is associated with regulatory, transcribed and other functional sequence regions, whose code is essential for the accurate function of an organism<sup>[53,54]</sup>. Because of the great importance of this (information carrying) molecule in context of full understanding living organisms, DNA is - among other molecules, which bind to and interact with the DNA (e.g. ligands) - a substantial part of the applied and theoretical biophysics research.

DNA was first isolated and identified by Friedrich Miescher in 1869<sup>[55,56]</sup>. Building on several other discoveries concerning the molecular composition of the DNA, James Watson and Francis Crick suggested (based on a single X-ray diffraction image taken of Rosalind Franklin and Raymond Gosling) in their famous Nature-article in 1953 first the correct structural description of the DNA, wherefore they received the Nobel Prize in 1962<sup>[57]</sup>. The DNA is made up of two long antiparallel oriented biopolymer strands which are coiled around each other forming a chainlike double helix structure. Each polymer strand consist of single subunits, respectively monomers - the so called nucleotides - which in turn can be subdivided in three basic molecular components: a phosphate group, a sugar base and an organic base (see Figure 2.1 A). The sugar is desoxyribose (pentose), consisting of five carbon atoms, which are numbered in line from 1' to 5'. The negatively charged phosphate group is connected via a phosphodiester bond to the 5' carbon atom and the base is linked to the 1' carbon atom of the sugar (Figure 2.1 B). The base components of DNA nucleotides can be either a purine like adenine (abbreviated A) or guanine (G) or a pyrimidine like cytosine (C) or thymine (T). To form a polymeric strand the single nucleotides are connected via

another phosphodiester bond, which links the hydroxyl group located at the 3' carbon atom of the pentose with the phosphate group located at the 5' carbon atom of the neighboring nucleotide. Thereby alternating phosphate and sugar residues build up the backbone of a DNA strand<sup>[58]</sup> (see Figure 2.1 C). The asymmetric ends of a single DNA strand are named 5' end and 3' end, whereby the 5' end has a terminal phosphate group and the 3' end a terminal hydroxyl group. This certain directionality, known technically as 5' prime to 3' prime, is an important characteristic. A polynucleotide strand is synthesized by the enzyme DNA polymerase by repeatedly adding a new nucleotide to the 3' end, whereby the sequence is based on an existing DNA strand (so-called templates).

**FIGURE 2.1** Schematic (A) and chemical formula (B) of a single nucleotide, showing their sugar, phosphate and base. In addition, a single strand is sketched (C). This figure was created inspired by<sup>[1]</sup>.



As mentioned above, almost all DNA molecules exist in form of two antiparallel single polynucleotide strands, held together by non-covalently hydrogen bonds between the opposing bases (see Figure 2.2 A). Furthermore there is just one enabled combination for pairing two bases; either adenine with thymine (via two hydrogen bonds) or guanine with cytosine (via three hydrogen bonds). Because of this restriction one strand has a nucleotide sequence which is complementary to the second strand and a backbone with opposite directionality. At physiological conditions the two strands coil around each other forming a double helix<sup>[57]</sup>. This is a very robust configuration that can accommodate any sequence of nucleotides without altering its basic structure<sup>[1]</sup>. Among the hydrogen bonds between opposing bases the double helix is stabilized by the lightly twisted stacking of the base pairs<sup>[59]</sup>. The DNA exist in many different conformations, whereat the most common one in functional organisms is the so-called B-DNA<sup>[58]</sup>. The double helix has a diameter of 2.4 nm, is right handed and shows a full turn at 3.4 nm corresponding to 10.4 involved base pairs. The distance between two base pairs is 0.34 nm<sup>[60]</sup>. The alternating base pairs are nearly covered by the negatively charged backbone, but as the strands are not full symmetrically arranged with respect to each other, they form grooves (see Figure 2.2 B). The major groove is 2.2 nm wide and the minor groove is 1.2 nm wide. As a consequence this regions are possible binding sites for DNA binding molecules like polymerases or transcription factors<sup>[61]</sup>.

As DNA was introduced as a kind of molecular library, the obvious question is how the information is stored. The secret consists of the specific base sequence that encodes the biological information. Three sequent bases (e.g. TCA, CAG, TTT) are called codon and code for a specific amino acid<sup>[62]</sup>. A long row of codons represents a region of the DNA that is named gene, whereat each gene is responsible for the composition and structure of protein molecules (which are made of amino acids).

To differentiate between genes there exist stop or nonsense codons, signifying the end of a coding region<sup>[63]</sup>. DNA molecules exist in aqueous solution not in a linear extended form, but like a protein-stabilized clew (though the DNA-backbone is strong negatively charged). This statistical behavior is caused by the interplay with surrounding molecules and other entropic effects.

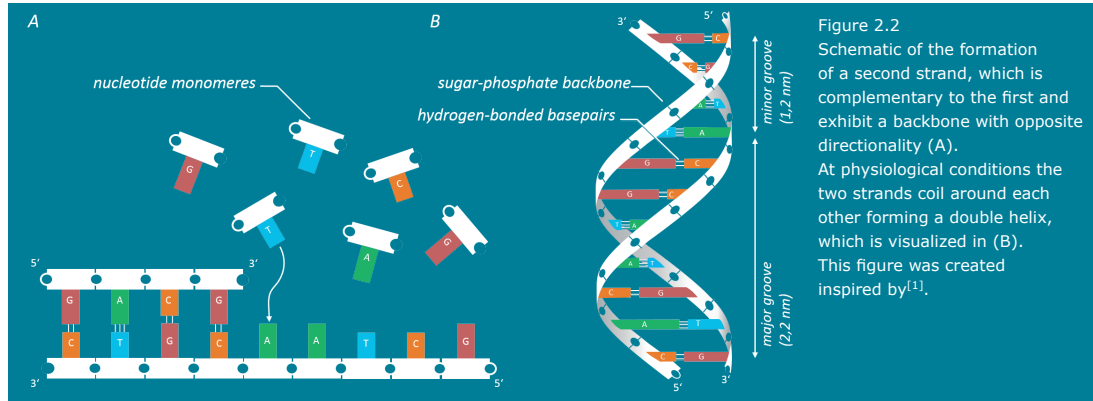


Figure 2.2 Schematic of the formation of a second strand, which is complementary to the first and exhibit a backbone with opposite directionality (A). At physiological conditions the two strands coil around each other forming a double helix, which is visualized in (B). This figure was created inspired by<sup>[1]</sup>.

A wide variety of structural proteins (e.g. histones) exist in cellular environments, which organize the double-stranded DNA (dsDNA) into a very compact structure<sup>[1]</sup>. Hence, without folding a dsDNA molecule it would not fit into a single cell, because of its immense length (about 2 m for the human genome). Therefore, the investigation of the stability and mechanical properties of DNA molecules plays an essential part for a profound understanding of biological processes. In addition, such specific knowledge (e.g. obtained by force spectroscopy methods) is of high interest for medical and biotechnological applications.

### 2.1.2 Proteins and Biological Pores

Looking through a microscope at cells and analyzing their optical components or biochemical and electrical activities is essentially like observing proteins<sup>[1]</sup>. The cell's dry mass consists mostly of proteins and to get a sense of the dimensions, a single haploid yeast cell for example contains the total number of  $\sim 50$  million proteins<sup>[64]</sup>. As one can imagine this class of molecules represents not only the building blocks from which cells are made of, but also execute the bulk of physiologic functions in an organism. Some proteins are responsible for carrying messages, act as signal integrators or operate as tiny molecular machines with moving parts. Yet others form channels or pumps in membranes for controlling exchange of small molecules. There are proteins like enzymes, providing complex molecular surfaces in cellular environment, which are responsible for promoting many chemical redox reactions. There are much more examples for specialized proteins acting for instance as hormones, elastic fibers, toxins, antibodies, antifreeze molecules or source of luminescence<sup>[1]</sup>. The chemical composition of a number of proteins was first described by the chemist Gerardus Johannes Mulder, who published a paper in 1838 entitled "On the composition of some animal substances"<sup>[65]</sup>. His results - after elemental analysis of common animal and plant proteins - surprisingly led to the conclusion that nearly all proteins

had the same composition, namely  $C_{400}H_{620}N_{100}O_{120}P_1S_1$ . He also hypothesized that all proteins are made up of one fundamental substance and identified much smaller molecules (compared to proteins) that came to be called amino acids, because they consist of both amino and carboxylic acid characteristics<sup>[66]</sup>. The right inset in Figure 2.3 A shows the general structure of an amino acid: A central carbon atom (C) is bonded to a carboxyl group (-COOH), a hydrogen atom (-H), an amino group (-NH<sub>2</sub>) as well as to a side chain (residue: R). This side chain differs from amino acid to amino acid and causes a great variety of chemical and physiological properties (e.g. polarity, hydrophobic or hydrophilic characteristics, acid-base equilibrium, etc.). The chemical structure of a side chain can be simple (e.g. a single hydrogen atom in case of the amino acid Glycine) as well as more complex (e.g. aromatic rings as observed for Tryptophan or Phenylalanine). The single amino acids are covalently linked via a peptide bond (see left inset in Figure 2.3), which forms when the nitrogen atom from the first amino acid shares electrons with the carbon atom (from the carboxylic group) of the second amino acid. Within this condensation reaction a water molecule (H<sub>2</sub>O) is released<sup>[1,52]</sup>. A whole protein consists of a long single stranded chain of these amino acids and is called polypeptide. This primary sequence, as shown in Figure 2.3 A, is unique for each type of protein. This primary sequence is not directly responsible for the proteins biological function, but its three dimensional spatial structure.

**FIGURE 2.3**

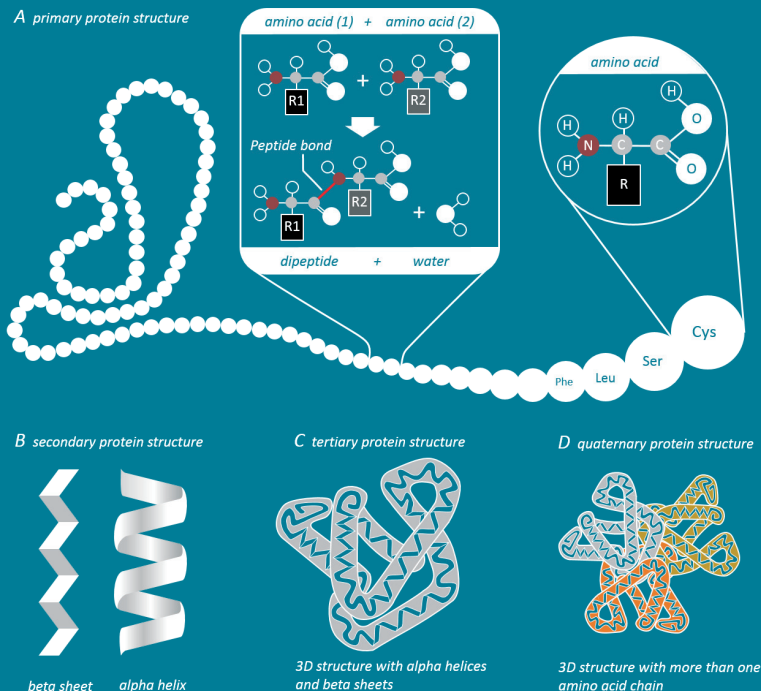
*A primary protein structure*

The primary protein structure consists of a long single-stranded chain of amino acids (A). The chemical structure of a single amino acid is depicted in the round inset. Two adjacent amino acids are connected via a peptide bond (square inset).

The secondary protein structure describes repeatedly recurring conformations such as the  $\alpha$ -helix and the  $\beta$ -sheet (B).

The tertiary protein structure describes the three-dimensional conformation (C).

If a protein is build of more than one polypeptide chain, this conformation is called quaternary protein structure (D).



For example, receptor-ligand interactions are based on the formation of very specific binding pockets that identify distinct target molecules (lock-and-key principle). The folding of an amino acid chain (leading to the spatial structure) is constrained by bond angles and supported by many different non-covalent bonds (*hydrogen bonds*,

*ionic bonds and van der Waals attractions*) that are formed between one part of the chain and another. A single non-covalent bond is weak in contrast to covalent bonds (30 to 300 times weaker)<sup>[4]</sup>, but by acting of many weak bonds in parallel they can precisely hold two chain regions together. Such shapes of repeatedly reoccurring conformation are described by the secondary protein structure. In Figure 2.3 B the structure of the  $\alpha$ -helix and the  $\beta$ -sheet is schematically illustrated. The tertiary protein structure (image C) describes the exact three-dimensional conformation of the whole chain. Among the weak forces noted above a fourth weak force has a central role in defining single folding steps as well as the final folded conformation. In an aqueous environment the nonpolar side chains of some amino acids tend to be forced together, thus minimizing their disturbing effect on the hydrogen-bonded network of water molecules<sup>[4]</sup>. As a result, the final protein conformation is the structure which exhibits the minimized free energy. The quaternary protein structure (image D) describes the ability of some proteins to form larger protein complexes with more than one polypeptide chain involved. The same weak forces enabling the initial protein folding and forming of binding pockets are also responsible for the complex structure<sup>[52]</sup>.

The following introduces the two most important proteins in context of this thesis.

### **Binding of biotin to streptavidin**

The binding of the biomolecules biotin and streptavidin is one of the strongest non-covalent interactions known in nature<sup>[67,68]</sup>. Based on its resistance to organic solvents, denaturants and extremes of temperature and pH, this binding is extensively used in molecular biology and bionanotechnology to link biomolecules or to immobilize them onto surfaces. The high affinity results from several factors<sup>[67]</sup>. There is an extensive network of hydrogen bonds and van der Waals interactions between streptavidin and biotin as well as specific ordering of some surface polypeptide loops that bury the biotin in the interior of the streptavidin binding pocket. This binding pocket is formed by the secondary structure of a streptavidin monomer, which is composed of eight antiparallel  $\beta$ -sheets and leads to the formation of an antiparallel  $\beta$ -barrel tertiary structure (see Figure 2.4).

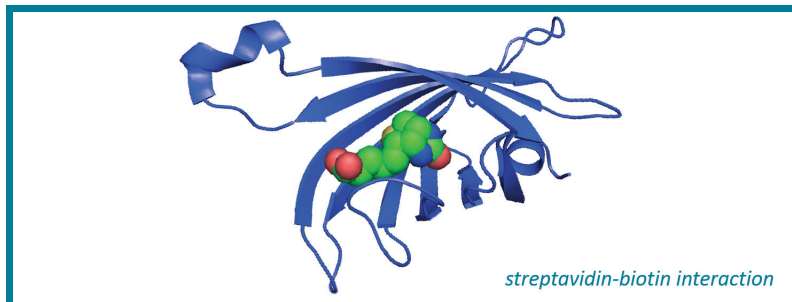


**FIGURE 2.4**

Schematic illustration of the biotin-streptavidin binding. The streptavidin (blue ribbon representation) exhibits a binding pocket in which the biotin (colored space filling picture) is located<sup>[69]</sup>.

The biotin binding-site is located at the end of each barrel and is made of residues from the interior of the barrel. In addition, the association of four identical streptavidin monomers, forming a tetrameric complex structure, preserve the ability for the contribution of one subunit to support the binding of a neighboring subunit (by means of a Tryptophan side chain)<sup>[67]</sup>. Due to its strong interaction (with a dissociation

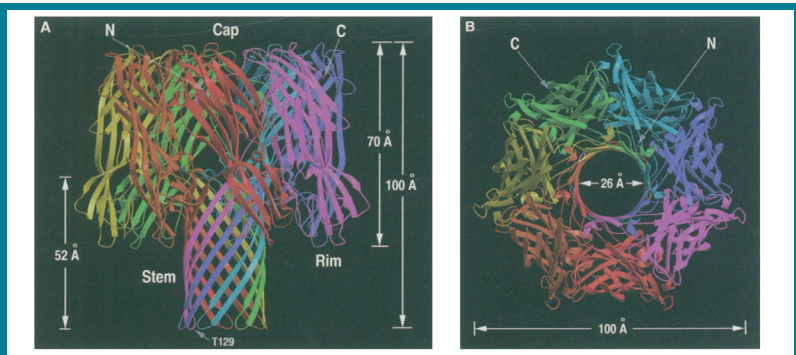
constant of about  $10^{-14} \text{ mol/l}$ )<sup>[70]</sup> this binding construct is utilized to immobilize dsDNA (attached to biotin) onto the surface of a microsphere (coated with streptavidin). With this method it is possible to perform optical tweezers force measurements with individual dsDNA strands, without breaking this binding, and thus be able to detect forces in the high piconewton regime<sup>[71,72]</sup>.

### Pore forming toxin $\alpha$ -hemolysin

Biological membranes contain a great variety of membrane proteins, which play a crucial role for different processes, such as for signal transduction and neurotransmitter transport. Thus, these proteins are considered as a target for more than half of all pharmaceutical drugs<sup>[73,74]</sup>. Some diseases such as pneumonia, meningitis or infections of the urinary tract are immediately caused by the protein toxin  $\alpha$ -hemolysin, which is produced and secreted by virulent strains of *Escherichia coli* bacterial species<sup>[75-77]</sup>. Among *E.coli* hemolysin can be segregated by many different kinds of bacteria such as *Staphylococcus aureus* or *Vibrio parahemolyticus* and other pathogens. One of the most studied protein pores is  $\alpha$ -hemolysin of *Staphylococcus aureus*. This is a self-assembling 232.4 kDa toxin that can bind in its monomeric form to a cellular membrane, where it oligomerizes into a water-filled transmembrane channel<sup>[78-80]</sup>. The pore-forming property induces uncontrolled permeation of water, ions and small organic molecules through the membrane resulting into cell death via irreversible osmotic swelling (leading to cell wall rupture and eventually cell lysis), dissipating the transmembrane potential or discharge of essential molecules like ATP<sup>[78]</sup>. Blood cells of different types (human platelets, monocytes a.o.)<sup>[81]</sup> are highly susceptible to membrane permeation by  $\alpha$ -hemolysin. The first crystallographic structures of an assembled  $\alpha$ -hemolysin were presented by Song et al. in 1996 where they show the heptameric organization of its protomers<sup>[82]</sup> (see Figure 2.5).

**FIGURE 2.5**

Ribbon representation of the  $\alpha$ -hemolysin heptamer structure, which was published by Song et al. in 1996<sup>[82]</sup>. Each protomer is shown in a different color. A: view perpendicular to the sevenfold axis. B: view from top of the heptamer and parallel to the sevenfold axis.



The protein pore exhibits a mushroom-like shape, with a  $\beta$ -barrel stem (52 Å), that protrudes from the cap domain through the lipid bilayer membrane into the cells interior. The cap consists of a large vestibule (nanocavity with diameter of 4.6 Å) that is connected to the cell's exterior by a large opening (2.6 Å). The narrowest part of the channel is located at the base of the stem with a constriction diameter of 1.4 Å (see also Figure 2.16 A). This protein channel is highly suitable for various biotechnological applications, because of several vital properties<sup>[78]</sup>. Once assembled  $\alpha$ -hemolysin is stable over a wide range of temperature and pH, it can bind to various

biological and synthetic lipid bilayer membranes and the channel is in an open state at usual conditions. In addition, the binding process is of spontaneous nature, and thus requires no specific ionic conditions<sup>[78]</sup>. It is also feasible to implement trigger by external stimuli by means of genetic engineering, which lead to switching between the open and close state<sup>[83,84]</sup>. When  $\alpha$ -hemolysin is incorporated in a lipid bilayer membrane, the channel can be used as stochastic sensor. This can be achieved by applying a voltage bias and detecting variations in the transmembrane ionic current, while molecules (with suitable size) are passing through it. More detailed information about  $\alpha$ -hemolysin acting as a biological nanopore sensor for investigation of linear macromolecule translocation is presented in 2.5.

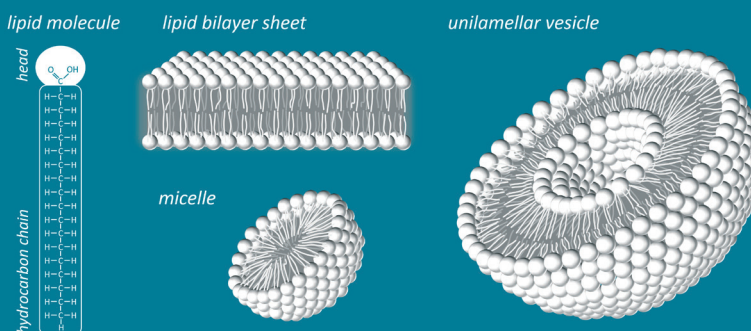
### 2.1.3 Lipids and Lipid Bilayer Membranes

Next to DNA and proteins, lipid molecules constitute the third part of biomolecules – apart from water – and represent the main mass fraction of most living organisms. The investigation of modern lipid chemistry started in the 17th and 18th centuries with initial observations by Robert Boyle, Poulletier de la Salle, Antoine François de Fourcroy and others<sup>[85]</sup>. In the 19th century the chemist Michel Chevreul identified oleic, butyric, capric and stearic acids and cholesterol as components of animal fats<sup>[86]</sup> and showed that fats were comprised of glycerol and fatty acids<sup>[85]</sup>. Another milestone in analyzing fats and oils as well as describing their structure-property relationships was the introduction of the iodine value in 1884 by Arthur van Hübl<sup>[87,88]</sup>, which was used to determine the amount of unsaturation in fatty acids.

All various types of lipid molecules in cellular membranes are of amphiphilic nature, i.e. they have hydrophilic (water-attractive, polar) head as well as a hydrophobic (water-repellent, nonpolar) tail (see Figure 2.6). The most abundant membrane lipids are phospholipids, which have a polar head group and two hydrophobic hydrocarbon chains<sup>[1,52]</sup>. These tails are normally fatty acids, which differ in length and amount of cis-double bonds (i.e. it is unsaturated). These differences are essential, because they provide various possible packing arrangements and thus affecting the fluidity of the membrane<sup>[1]</sup>. The formation of bilayer structures (arranged spontaneously in an aqueous environment) as pictured in Figure 2.6 is directly induced by the shape and amphiphilic properties of each single lipid molecule. Here, hydrophilic molecules can form either electrostatic interactions or hydrogen bonds with water molecules (why they are dissolvable), whereas hydrophobic molecules cannot form any favorable interaction with adjacent water molecules, and thus are insoluble in water. Once such molecules are dispersed in an aqueous environment they force the neighboring water molecules to rearrange into icelike cages that enclose them<sup>[1,89]</sup>. These cage structures in turn cause an increase of free energy, because of the higher order of the water molecules. To minimize the free energy costs, the hydrophobic molecules (or hydrophobic parts of amphiphilic molecules) arrange as cluster in order to influence the merest number of water molecules<sup>[1,52]</sup>. This is the driving energy for the spontaneously aggregation of lipid molecules to hide their hydrophobic tails and directing their hydrophilic heads towards the water. Thus, they can form spherical micelles (with only the tails inwards) as well as bilayer sheets or vesicles (with tails sandwiched between the head groups), which are illustrated in Figure 2.6. The

specific form depends on the shape of the single lipids (cylindrical or conical), which in turn depends on the number of tails, the number of double bonds and the size of the head<sup>[4]</sup>.

**FIGURE 2.6**  
Lipid molecules (in the left) have a nonpolar hydrocarbon tail and a polar head. Within aqueous solution they can be packed in different arrangements as micelles or vesicles. A shell of a cell mainly consists of lipid bilayer structures. The Sketch was created inspired by<sup>[52]</sup>.

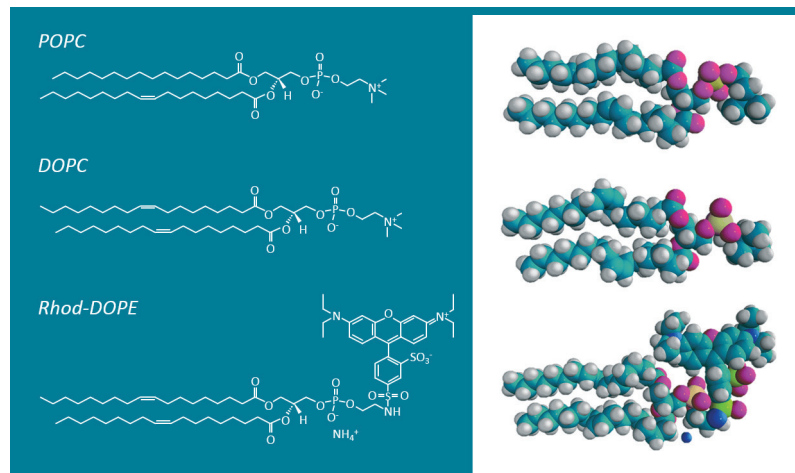


The energetic most favorable arrangement is also the driving force for another important property of phospholipid bilayers: self-healing feature. Once a small tear appears in a bilayer, this would generate a free edge with water which is eliminated (or previously prevented) by spontaneously rearrangement of the lipids. Unilamellar vesicles also have a favorable form, because the bilayer exhibit no edge towards water by closing in on itself<sup>[1,89]</sup>. Beside this self-sealing phenomenon it is also noteworthy that these bilayers are fluid, i.e. individual lipid molecules are able to diffuse within a bilayer. This property is crucial for the functionality of most cellular membranes<sup>[52]</sup>. In general, lipid membranes allow for maintaining an internal milieu that differs from the external surrounding. In addition, eukaryotic cells contain several internal membrane systems, which encloses specific compartments and thus enables spatial separated biochemically reactions<sup>[90]</sup>. Furthermore, membranes work in selective manner, i.e. they supply little permeability for ions and contain incorporated protein channels. These proteins act like checkpoints and ensure a controlled exchange of various solutes. Some checkpoints also allow for signal transduction across the membrane border without material transport, which is realized by conformational changes of specific receptor molecules<sup>[91]</sup>. By accomplishment of ionic, pH or electrical charge gradients across the membrane it is also feasible to ensure fast signal responses as well as to store energy<sup>[90]</sup>. Cargo transport between different compartments within a cell (or between different cells) is accomplished by small vesicles, which are able to perform budding, fission and fusion into an external membrane<sup>[91]</sup>. The ability to generate artificial vesicles with various lipid compositions provides a very important tool in biological, biophysical and pharmaceutical research to study the versatility of membrane functions.

### Phospholipid structure

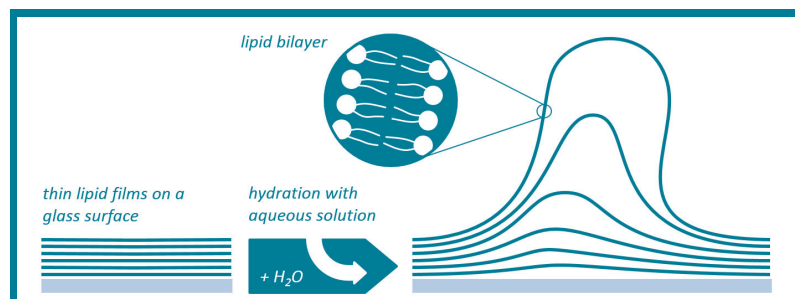
Figure 2.7 pictures the three primarily used types of phospholipids<sup>[92]</sup>. POPC (*1-palmitoyl-2-oleoyl-sn-glycero-3-phosphocholine*) is naturally present in eukaryotic cell membranes, and thus is a widely used lipid for biophysical experiments (e.g. the study of lipid rafts<sup>[93,94]</sup>). It has one monounsaturated tail of 18 carbon atoms and a second saturated tail of 16 carbons. DOPC (*1,2-dioleoyl-sn-glycero-3-phosphocholine*) has

the same relevance as POPC and differs in its chemical structure only in the second tail, exhibiting a second monounsaturated tail of 18 carbons. Rhod-DOPE (*1,2-dioleoyl-sn-glycero-3-phosphoethanolamine-N-(lissamine rhodamine B sulfonyl)*) is a compound of the phospholipid DOPE, which is labeled with Rhodamine B. It provides a very stable fluorescent signal<sup>[95]</sup> and commonly used in studies of characterizing membrane lipid phases<sup>[96]</sup>.



### Lipid swelling and electroformation

Angelova et al. reported in 1986 the first observation of lipid swelling and liposome formation on platinum electrodes in water solutions in presence of DC electrical fields<sup>[97]</sup>. The basic concept (without an applied electric field) is illustrated in Figure 2.8, where the swelling occurs simply by a hydration step. Conducted at low-voltage electric field conditions this technique is usually called electroformation and promotes the formation of truly unilamellar vesicles<sup>[98]</sup>. For electroformation of giant unilamellar vesicles (GUVs), a lipid solution (in an organic solvent) is dried on conductive material (wire or plates) before the hydration step is performed, which is supported by the presence of (today usually alternating) electric field.



Herein, that the size of the generated GUVs exhibits a (experimental condition dependent) wide distribution between  $1 \mu m$  and  $500 \mu m$ . Furthermore, the GUV yield and size decrease drastically if ions are present in the aqueous solution<sup>[99]</sup>. The

formation of small unilamellar vesicles (SUVs) with a size<sup>[100]</sup> between 20 nm and 100 nm is performed by ultrasonication of an aqueous dispersion of phospholipids. Usually a probe sonicator is used for small volumes, ensuring sufficient high energy<sup>[100]</sup>. For assisting GUVs or SUVs to adsorb (and burst) on artificial surfaces like silicon-nitride electrostatic interaction is known to play an important role<sup>[101]</sup>. Cha et al. reported that even for neutral (zwitterionic) lipids, electrostatic interaction is essential for controlling the adsorption and fusion of lipid vesicles to form supported phospholipid bilayers on surfaces. The production of lipid monolayers follows a different approach, which is introduced in the next chapter.

## 2.2 Langmuir-Blodgett Films

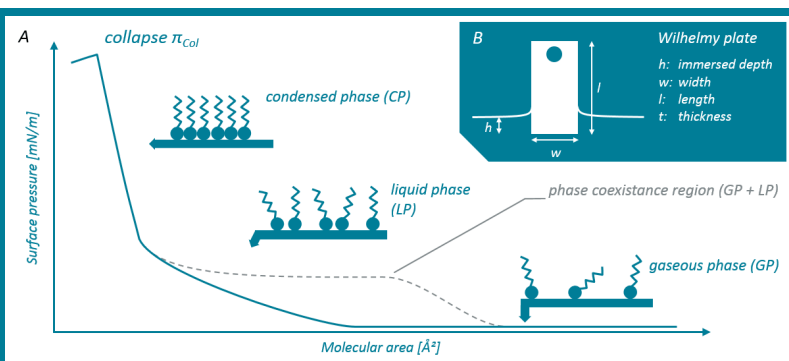
The effects of oil on water surfaces was known to the ancients. The phenomenon of such spread films in calming ripples on a surface was part of the common lore of fisherman and sailors<sup>[102]</sup>. However, Benjamin Franklin was the first who showed scientific interest in quantifying these mono-molecular thin films. He reported in his paper<sup>[103]</sup> in 1774 that:

*"...the oil, though not more than a teaspoonful...spread amazingly...making all that quarter of the pond, perhaps half an acre, as smooth as a looking glass".*

This work has been constituted as "the first recorded scientific experiment in surface chemistry"<sup>[102]</sup>. The first modern contribution to the investigation of molecular films was given by Agnes Pockels, who began her studies in the family kitchen when she was only 18 years old. In her famous letter to Lord Rayleigh, published in 1891 in Nature<sup>[104]</sup>, she declared the importance of cleanliness and described the development of many techniques, which are now standard tools. Besides the through technique, she also presented the first surface pressure-area diagram<sup>[105]</sup>. According to further studies carried out independently by Rayleigh, Hardy and Devaux, Irvin Langmuir published in 1917 his important series "The constitution and fundamental properties of solids and liquids"<sup>[106,107]</sup>.

**FIGURE 2.9**

Standard isotherm (or surface pressure-area diagram) illustrating the gaseous, liquid and condensed phases and additional the temperature and lipid dependent phase coexistence region. The inset shows the dimensions of the Wilhelmy plate.



He introduced the film balance technique and showed that it is possible to elucidate the size and shapes of molecules and their orientation at the interface (e.g. that only the hydrophilic headgroups were immersed in the subphase)<sup>[102]</sup>. The technique of transferring monolayer films onto solid substrates, which is applied in this thesis,

was developed and first published<sup>[108]</sup> in 1934 by Katherine Blodgett. Because Blodgett and Langmuir worked closely together, this transferred films are now universally referred as “*Langmuir-Blodgett films*” (LB films)<sup>[102]</sup>. In Figure 2.9 a standard surface pressure-area diagram (isotherm) illustrates the different observable phases during reduction of the area, which is available for the lipid molecules.

According to the initial spreading of lipids onto the subphase, the molecules behave as a two-dimensional gas (gaseous state, GP), if no external pressure is applied. By compressing the area, some ordering of the monolayer film can be observed (slightly increasing pressure) and it behaves like a two-dimensional liquid (liquid phase, LP). When the barrier closing is continued, additional ordering takes place (see the sketches in Figure 2.9 and Figure 2.10) and the monolayer behaves as a quasi-solid (condensed phase CP). It is characteristic for the CP to exhibit a usually linear dependence between surface pressure and molecular area<sup>[109,110]</sup>. At the end of the CP the collapse pressure  $\pi_{col}$  is reached at which the pressure increases no longer, because the exerted forces turn out to be too strong for confinement in two-dimensions. This results in ejection of the lipid molecules out of the monolayer plane<sup>[109]</sup>. The value of  $\pi_{col}$  depends on the substance (lipid molecule structure), the temperature, the pH of the subphase, the rate of compression and others. This dependency (except the rate) also applies to a more or less expressed plateau in the isotherm, which refers to a phase coexistence region (GP and LP). The introduced surface pressure  $\pi_{LB}$  is the inverse of the surface tension, which is defined as the work required to produce a surface isothermally per unit area of surface<sup>[110]</sup>. In case of high intramolecular forces between molecules (e.g. water), the mandatory work to create the surface, including the surface tension, is large. Hence, this high surface tension causes water to form a spherical shape to minimize its surface area and by this its surface tension. This relationship is essential for experimentally measuring the surface pressure by means of a Wilhelmy plate. This plate (a strip of chromatography paper) is pulled down into the subphase by surface tension, when it is suspended at an air-water interface (see inset in Figure 2.9). The forces acting on the plate are gravity, surface tension (acting downwards into the subphase) and buoyancy (acting upwards). With the dimensions introduced in Figure 2.9 the net force  $F_{LB}$  downwards can be described by:

$$F_{LB} = (\rho_p l w t) \cdot g - (\rho_l h w t) \cdot g + 2 \cdot (w + t) \cdot \gamma \cdot \cos \theta$$

*Force = weight - upthrust + surface tension*

Where  $\rho_p$  is the density of the plate,  $\rho_l$  the density of the subphase,  $g$  the acceleration due to gravity,  $\gamma$  the surface tension of the liquid and  $\theta$  the contact angle of plate to subphase. The net force is measured by an electronic micro-balance sensor in such manner that the immersed depth  $h$  remain constant during recording. The change of the net force in presence of a monolayer onto the subphase can be described by:

$$\Delta F_{LB} = F_{LB, \text{water}} - F_{LB, \text{monolayer}} = (\gamma_{\text{water}} \cos \theta - \gamma_{\text{monolayer}} \cos \theta) \cdot 2(w + t)$$

Assuming that the contact angle  $\theta$  is zero (ideal wetting of the Wilhelmy plate) and  $t \ll w$ , the change in force can be termed:

$$\Delta F_{LB} = (\gamma_{\text{water}} - \gamma_{\text{monolayer}}) \cdot 2(w + t) \approx \pi_{LB} \cdot 2 \cdot w$$

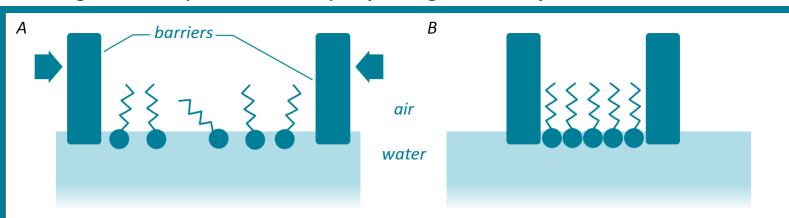
$$\pi_{LB} = \frac{\Delta F_{LB}}{2 \cdot w} (\gamma_{\text{water}} - \gamma_{\text{monolayer}}) = \text{surface pressure of the monolayer}$$

As it is visible in the last equation, for estimation of the surface pressure (induced by

surfactants like lipid molecules) the surface tension of the pure subphase (e.g. water) has to be recorded first.

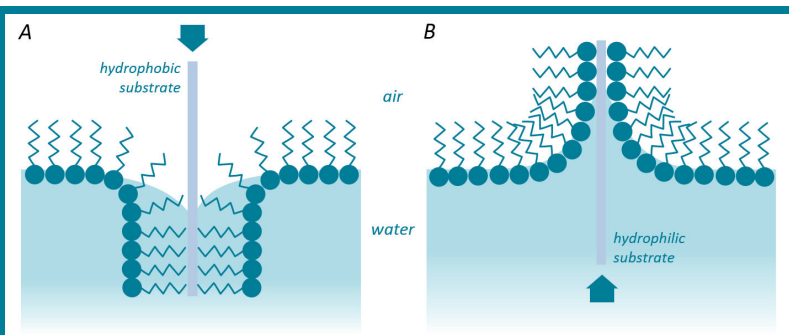
To transfer a lipid monolayer onto a solid substrate, the surface (transfer) pressure has to be kept constant during the whole transfer process. This ensures that the deposited LB film features a homogeneous and uniform lipid molecule distribution. In addition, the transfer pressure value is usually chosen to be in the middle of the CP resulting in a dens packed monolayer (see Figure 2.10 B).

**FIGURE 2.10**  
Schematic illustrating the expanded (A) and compressed (B) monolayer on a water surface.



The most common transfer is conducted by lowering the substrate vertically into the subphase or raising it out of the subphase, respectively. The direction is determined by the surface properties of the substrate. For deposition onto a hydrophobic substrate the first transfer is performed by dipping it through the air-water interface. For a hydrophilic substrate the procedure is vice versa (compare to Figure 2.11).

**FIGURE 2.11**  
Illustration of the deposition of a first monolayer onto a hydrophobic (A) and hydrophilic (B) substrate. Due to the different affinity of the substrate to the hydrophobic tails or hydrophilic headgroups of the lipid molecules the dipping has to be performed in opposing directions.



### 2.3 Optical Trap

Since the observation of trapping dielectric particles in a single-beam gradient force in 1986 by Ashkin et al.<sup>[111]</sup>, the field of optical tweezers research has grown tremendously nowadays addresses biological, physical and chemical issues as well as soft condensed matter physics processes<sup>[112,113]</sup>. Optical forces are ideally qualified for manipulation of mesoscopic systems, which can be categorized by forces ranging from femtonewtons to nanonewtons, length scales ranging from nanometres to micrometres, and time scales ranging upward from a microsecond<sup>[112]</sup>. In biologic context, these ranges cover various of intra- and intercellular processes, such as reproduction and signaling<sup>[112]</sup>. However, the basic observations and studies leading to the development of optical tweezers (OT) were already reported by Arthur Ashkin in 1970 at AT&A Bell Laboratories<sup>[114]</sup>. He discovered as first the contactless

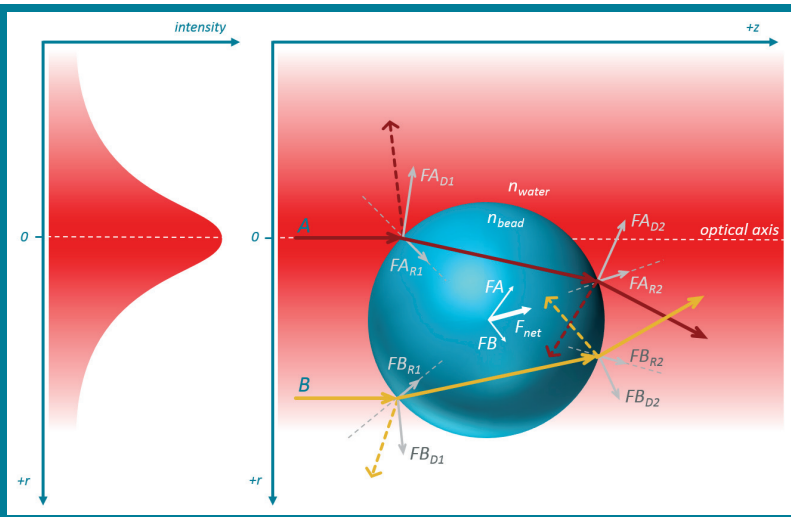
acceleration of freely suspended particles via forces of radiation pressure, which were induced by visible laser light. Moreover, he also observed that once a microparticle was hit by the laser beam, it was simultaneously accelerated in the direction of the laser light (caused by radiation pressure) and radial deflected into the beam axis (gradient force)<sup>[114]</sup>. With this finding it was possible to manipulate and trap a particle could in two dimensions. The establishment of a stable three dimensional trap turned out to be more complicated. The main issue implied the complete compensation of the radiation pressure. The first attempts using two equal laser beams with opposing directions<sup>[114]</sup> and a vertical setup design utilizing gravity (optical levitation)<sup>[115]</sup>, led to a functioning 3D-trap, but suffered from an inflexible setup and performance fluctuations of the laser beam. Finally, a very elegant solution was found by Ashkin, Dziedzic, Bjorkholm und Chu in their initially mentioned publication in 1986. They used a single strongly focused laser beam, whereas the axial gradient force was found to be very large, and thus compensating the radiation pressure and dominating the axial stability of a trapped particle<sup>[111]</sup>. This system emerged to be an straightforward and robust setup for stable trapping of objects either much smaller than the used wavelength of light or much larger<sup>[112]</sup>. Only one year later first biophysical applications were reported, demonstrating a selective and damage-free trapping of bacteria, viruses and living cells by utilization of an infrared-laser<sup>[116,117]</sup>. Even though Ashkin had also the vision of trapping atoms, it felt to Chu to refine this technique for cooling and trapping neutral atoms (awarded with the Nobel Prize in physics in 1997). To date, optical tweezers have been utilized to study viscoelastic properties or binding kinetics of single biopolymers (like DNA)<sup>[118,119]</sup>, cell membranes<sup>[120]</sup>, aggregated protein fibers (like actin)<sup>[121]</sup>, regulation of cytoskeleton-plasma membrane adhesion<sup>[122]</sup> and composite structures (like chromatin and chromosomes)<sup>[123]</sup>. Furthermore, it was feasible by OT to characterize forces exerted by molecular motors (like myosin, kinesin)<sup>[124,125]</sup> and to continuously sorting fluid-borne particles (like a sieve) by using an array of optical traps<sup>[126]</sup>. In the following section the basic functional principle of the optical trap is presented in more detail.

### **Functional principle of the optical tweezers**

As stated above particles either significantly smaller than the wavelength of light (Rayleigh-scattering regime) or significantly larger (Mie-scattering regime), can be trapped in stable manner. Small particles generate an electric dipole moment by reacting to the light's electric field, which, causes intensity gradients in the electric field toward the beam's focus<sup>[112,127]</sup>. Larger objects behave like lenses and refract the rays of light, and thus redirecting the momentum of their photons. The resulting recoil forces them toward the higher photon density near the beam's focus<sup>[112]</sup>. In this thesis microbeads with a size of about  $3 \mu\text{m}$  are utilized and plain geometrical optics can be used for explanation. The occurring radial gradient forces and radiation pressure (two dimensional trap) are schematically illustrated in Figure 2.12 for a microbead situated off the beam axis. The used laser (with TEM00 mode) exhibits a Gaussian intensity profile with  $I = I_{\text{max}} \exp(-2r_{\text{off}}^2/w_{\text{beam}}^2)$ , where  $I$  is the intensity of the beam in the distance  $r_{\text{off}}$  of the optical axis (maximal intensity). The beam  $w_{\text{beam}}$  width is not constant in axial direction and depends on the degree of focusing and the beam quality. Figure 2.12 shows two exemplary rays (A and B) symmetrically located about

the bead axis are and furthermore, the refractive index of the bead is higher than the index of the surrounding aqueous medium ( $n_{\text{bead}} > n_{\text{water}}$ ), which is an essential condition for a stable trapping.

**FIGURE 2.12**  
Occurrence of the involved forces when a microbead is in the proximity of a linear laser beam. As visualized by two rays (A and B), and the resulting forces induced by reflection and deflection, the bead is accelerated towards the beam axis and forwards in the +z direction. The schematic was drawn inspired by<sup>[114,128]</sup>.



A is the stronger ray (closer by the beam axis) and undergoes reflection and deflection at the entry in the bead as well as the exit out of the bead. These effects causes the radiation pressure forces  $FA_{R1}$  and  $FA_{R2}$  (which refer to the entry and exit reflection forces). The so-called gradient forces  $FA_{D1}$  and  $FA_{D2}$  refer to the entry and exit deflection forces and their radial components are much larger than for  $FA_{R1}$  and  $FA_{R2}$ . All forces (depicted so far) contribute to an acceleration in the +z direction and in addition, the net radial force for the stronger ray A is directed toward the beam axis. This results in the net force of FA (marked in the center of the bead) for the ray A. The description of the symmetrical but weaker ray B is analogous to above and results in a net force of FB which is also directed along +z and exhibits a net radial force component, which is directed away from the beam axis but weaker as the above. By combining FA and FB the resulting net force  $F_{\text{net}}$  acting on the microbead accelerate it as a whole towards the beam axis (with the highest light intensity) and forward in +z direction.

As stated above, the trapping in three dimensions is realized by strongly focusing the laser beam<sup>[111]</sup>. In Figure 2.13 this laser beam is once again visualized by two rays (A and B), which undergoes reflection and deflection at the bead-medium interfaces (the corresponding forces are similar to the ones in Figure 2.12). The resulting net force  $F_{\text{net}}$  is shown for three different situations (I, II and III). When the bead is situated above the laser focus  $f$ , the net force accelerates it downwards in direction of the focus. This behavior is the basic development in comparison with the former approach, because this force is a backward trapping force and opposes the direction of the laser beam<sup>[111,128]</sup>. The resulting net force is in any case oriented towards the beam focus (as for the situations bead under the focus (II) and bead beside the focus (III)), if the refractive index of the bead is higher than the index of the medium

and the bead is located in close vicinity of the laser beam. Once the net force vanishes, i.e. all radiation pressure and radial gradient forces neutralizing each other, the microbead is in a balanced state and thus, trapped in very close proximity to the laser focus in all three dimensions. Such a trapped bead can now be precisely manipulated with respect to the surrounding, by either moving the objective and the laser focus, or by moving the surrounding chamber while the objective position is fixed.

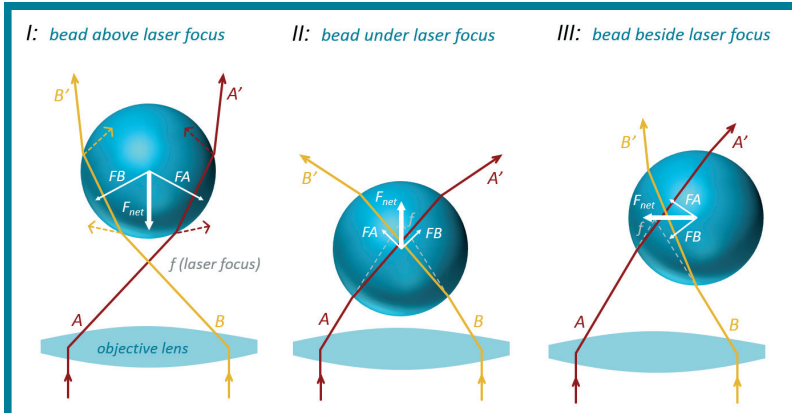


**FIGURE 2.13**

Three dimensional trapping by the use of a strongly focused laser beam. As schematically visualized by two rays, the resulting net force is for all depicted situations (I, II and III) directed towards the laser focus. The schematic was drawn inspired by<sup>[114,128]</sup>.

For biophysical applications, optical traps are commonly generated by infrared laser light with a wavelength of  $1064\text{ nm}$ . One advantage of this wavelength is, that biological objects (like cells or bacteria) and the surrounding medium absorb such light much less, which avoids heating or damaging of biological tissue<sup>[129]</sup>. Furthermore, a higher wavelength causes a smaller beam intensity at the trapped object, but still produces large forces under damage-free conditions<sup>[117]</sup>. A technical benefit of infrared systems is the easy separation of this light from visible light, and thus do not affect visual or video based monitoring and analysis.

### **OT force measurement and calibration**

A trapped particle can not only be utilized to execute forces onto other objects via movement of the trap position relative to the surrounding chamber, but it is also feasible to measure precisely the forces acting on the particle itself. This force measurement as well as the force calibration are very well explained in other publications<sup>[128,130,131]</sup>. Here, only the main basics are presented.

Once a particle is trapped, it is situated in a photonic potential  $V(x_{dev})$ , which can be approximately characterized as harmonic within the proximity of the laser focus:

$$V(x_{dev}) = \frac{1}{2} k_{stiff} x_{dev}^2$$

If an external force acts on the trapped particle, this leads to a deviation  $x_{dev}$  out of the balanced state, which in turn depends proportionally on the applied force. The proportionality factor  $k_{stiff}$  stands for the strength (or stiffness) of the optical trap and is comparable to the spring constant in Hooke's law:

$$F = -k_{stiff} \cdot x_{dev}$$

This linearity is true for typical applications and particle diameters of several micrometres and is valid for deviations of about 0.6-fold of the particle radius<sup>[132]</sup>. Therefore,

the displacement  $x_{dev}$  out of the balanced state has to be detected for accurate estimation of the external force. In addition, the factor  $k_{stiff}$  is usually recorded and calibrated experimentally.

The estimation of the deviation  $x_{dev}$  can be performed either by using the forward scattered or backscattered light or via video-based analysis. All measured parameters of these three methods (intensity of scattered light, exact beam position and pixel displacement of the imaged bead) allow for a conversion into the real physical deviation, by calibration with a prior determined mechanical displacement of the particle. This can e.g. be executed by moving the particle onto a solid surface and further movement of the optical trap. The three introduced methods and their (dis-)advantages are discussed in more detail in chapter 3.2.1.

The additional required factor  $k_{stiff}$  can be determined by applying a well-defined external force on the particle and simultaneously measuring the particle displacement. In aqueous medium the drag force via Stokes' law can be used:

$$F_{drag} = 6\pi \cdot r_{particle} \cdot \eta_{medium} \cdot v_{medium}$$

where  $r_{particle}$  is the radius of the particle,  $\eta_{medium}$  the viscosity of the surrounding medium and  $v_{medium}$  the flow velocity relative to the particle. This flow velocity can be precisely adjusted by moving the sample chamber (with respect to the fixed trap position) via a piezo stage. Therefore, a new force calibration for each new trapped particle can easily and quickly be acquired<sup>[128,130]</sup>.

## 2.4 Fluorescence Detection

George G. Stokes coined in 1852 the term „fluorescence“ after observing blue luminescence in the mineral fluorite as well as discovered the redshift<sup>[133]</sup>. Nowadays fluorescent detection of labeled molecules is a standard technique for optical observation and monitoring. Even molecules, which are smaller than the achievable optical resolution like labeled lipids, can be optically detected by the fluorescent emission of photons<sup>[134]</sup>. In the following a very brief introduction of the basic principles of photophysics is presented. For more detailed information, readers are encouraged to consult this publications<sup>[133-136]</sup>.

Once a dye (in the ground state  $S_0$ ) absorbs a photon of appropriate energy, a valence electron is promoted from  $S_0$  to some vibrational level in the excited singlet state ( $S_1$  or  $S_2$ ). This process of absorption is exceptionally fast and in the order of one femtosecond ( $10^{-15}$  sec). The excited system can transit back into the ground state by emitting (i.e. losing) a photon (see Figure 2.14). Due to a decrease of energy during the excitation, the energy of the emitted photon (fluorescence) is slightly lower in comparison to the energy of the exciting photon and the transition takes place on the nanosecond level ( $10^{-9}$  sec). This phenomenon is called Stokes or red shift. In addition to the relaxation process via fluorescence, there exist several other involved relaxation processes. The transition between the excited singlet ( $S_1$ ) state into the triplet state ( $T_1$ ) is called intersystem crossing and is possible due to intermolecular interactions. Once in the triplet state, the relaxation via photon emission is also feasible and called phosphorescence. The triplet state exhibit a long lifetime before decay to  $S_0$ , because this transition is spin-forbidden and thus unlikely. Further relaxation

processes exhibiting no radiation include internal conversion (collisions with other molecules close by) and rotational relaxation, for instance.

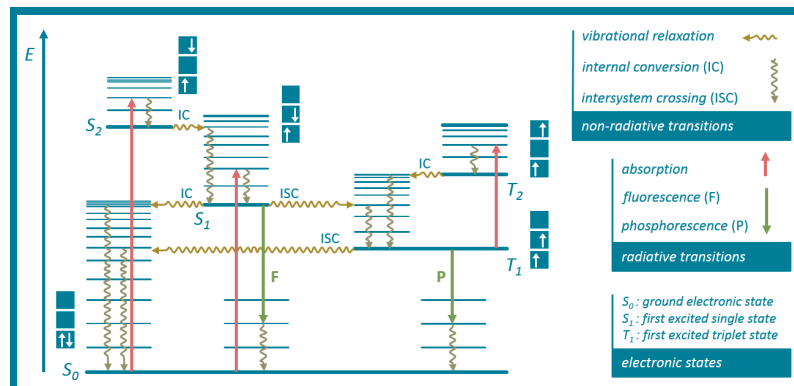


**FIGURE 2.14**

The Jablonski diagram illustrates and clarifies the basic principles of molecular photophysics by means of a graphic representation of the electronic states and (non-)radiative transitions. This schematic was created according to<sup>[133]</sup>.

More information about the experimental conditions for conducting fluorescence microscopy detection of Rhodamine B labeled phospholipid molecules is presented in chapter 3.2.2.

## 2.5 Nanopores

The term nanopore is used to describe a small hole of nanometre dimensions, which can be utilized as single-molecule detector. Such pores are either biological pore-forming proteins or tiny holes in synthetic materials such as silicon, silicon-nitride or graphene. The basic concept is exceptional simple: a single molecule is threaded through a NP, which connects two separated chambers and enables the detection of the molecules (via measuring current modulations while a transmembrane voltage is applied). The separating (and NP containing) membrane can be of artificial, biological or biomimetic nature. Thus, potential applications for NPs are biosensing, diagnostic and separation<sup>[13,15]</sup>. The main advantages of this nanotechnology are high sensitivity (to the single-molecule level), low costs and label-free detection, avoiding molecular amplification<sup>[15]</sup>. The first application of NPs for DNA sequencing was envisioned by Church, Deamer, Branton, Baldarelli and Kasianowicz in an outstanding patent application, that was submitted in 1995 and awarded in 1998<sup>[137,138]</sup>. The original abstract is as follows:

*"A method is disclosed for characterizing a linear polymer molecule by measuring physical changes across an interface between two pools of media as the linear polymer traverses the interface and monomers of the polymer interact with the interface, where the physical changes are suitable to identify characteristics of the polymer."*

Since then many research groups have extensively studied these NP-based methods. In the following, both kinds of synthetic and biological NPs are introduced and an overview of the impact of these NPs onto the field of *next generation sequencing* will be given.

### Solid-state nanopores

The manufacture of NPs from solid-state materials exhibits obvious advantages in comparison to their biological counterpart such as control of diameter and channel length, high robustness and durability as well as adjustable surface properties<sup>[13,138]</sup>. In addition they allow for integration into devices and high density arrays, and thus can be executed in parallel<sup>[13]</sup>. In 2001 Golovchenko and co-workers presented a novel technique - ion beam sculpting - by which they could produce single nanopores in thin silicon-nitride membranes<sup>[139]</sup>. Working with silicon-nitride and silicon-dioxide as membrane material benefit from their extremely well-developed and studied properties over the course of fifty years of microelectronics<sup>[13,139]</sup>. They utilized a focused ion beam to mill a tiny hole in such a membrane and also discovered, that pores could shrink and enlarge, depending on the applied ion rate and temperature. Today such silicon chips with thin silicon-nitride membranes (with or without a NP) are laboratory consumables at low costs. In Figure 2.15 A and B such a chip is shown, whereas the thin membrane is located on the bottom of the funnel-shaped etched window structure. The thickness of the membrane is variable and lies typically in a range between 10 and 500 nm. Today there are different techniques accessible (with varying NP size limits) for milling a NP into membranes. For example, a focused electron beam can generate a pore with a shape of an hourglass and a diameter of about 1 nm, whereas NPs produced by ion beams exhibit a more conical shape<sup>[140,141]</sup>. Using gallium ions NP diameters of about 5 to 20 nm are feasible<sup>[142]</sup> and by application of a helium ion beam NP diameters of down to 4 nm can be realized<sup>[143]</sup>.

**FIGURE 2.15**

Solid-state silicon chip with a thin silicon-nitride membrane at the bottom of the window structure (A and B, SEM images of the manufacturer SPI Inc.).

Sketch of a lipid bilayer-coated solid-state NP (C) taken from<sup>[51]</sup>.



One possible way of modifying the surface properties of a solid-state NP was published by Yusko et al. in 2011<sup>[51]</sup>. Inspired by the olfactory sensilla of insect antennae, they reported that a coating of nanopores with a fluid lipid bilayer is possible. With this method the surface chemistry can be tailored and allows for additional fine-tuning (and dynamic alteration) of pore diameters in subnanometre increments<sup>[51]</sup>. Moreover, the lipid bilayer coating also prevents NPs from clogging and minimizes non-specific binding.

Among these types of solid-state NPs there are several other approaches, like glass-capillaries with nanometre-sized openings<sup>[37,42,144]</sup> and NPs milled in graphene, which will certainly play a significant role in the field of NP research in the next decade.

### Artificial or natural protein nanopores

The patent application mentioned above was not only restricted to solid-state NPs, but also included "all ion permeable passages"<sup>[137]</sup>, including all types of protein pores. Only one year after patent filing, Kasianowicz et al. reported in 1996 the first demonstration of the transit of nucleic acids through an  $\alpha$ -hemolysin pore<sup>[18]</sup>. According to

this initial report a high number of publications followed, where many aspects of this translocation process have been examined in detail<sup>[19]</sup>. For example the characteristic signatures of the ionic current change during translocation of polynucleotides of various compositions are investigated<sup>[20,21]</sup>, including the effect of intramolecular hairpins<sup>[22]</sup> or ligands for derivatized DNA strands on the transit process<sup>[145]</sup>. Furthermore, the impact of *cis* or *trans* entry, regarding the rate of detectable transit events, was studied<sup>[24]</sup> as well as the effect of the applied voltage range and temperature<sup>[23,146,147]</sup>. Despite the importance of such biological pores as an envisioned tool for ultrarapid DNA sequencing<sup>[10,15]</sup> (more information in the next section), researchers have to tackle the challenge of appropriate incorporation of these proteins in a compatible surrounding. This is necessary, because it was supposed that proteins preserve their native conformation and properties (e.g. activity) only embedded in a membrane system<sup>[148,149]</sup>. A very recent report about different strategies for the fabrication of freestanding lipid bilayers and accurate protein reconstitution into it was published by Gutsmann et al. in 2015<sup>[42]</sup>.

In Figure 2.16 A a cross-section view of an  $\alpha$ -hemolysin pore embedded into a lipid bilayer membrane is shown<sup>[150]</sup>, which nicely illustrates the accessible channel and its nanometre-scale dimensions. The constriction with a diameter of 1.4 nm only allows for the transit of single-stranded DNA or RNA molecules, and thus the bigger lumen (nanocavity with  $\varnothing$  of 4.6 nm) appears to exhibit no additional benefit, but Howorka et al. used this space for engineering<sup>[25]</sup>. They demonstrated the application of a “DNA-nanopore” that was built by covalently attaching an individual ssDNA oligomer within the lumen of an engineered version of the  $\alpha$ -hemolysin pore. Due to binding of ssDNA molecules to the tethered DNA strand, it was possible to discriminate between individual DNA strand up to 30 nucleotides in length only differing by a single base substitution<sup>[25]</sup>.

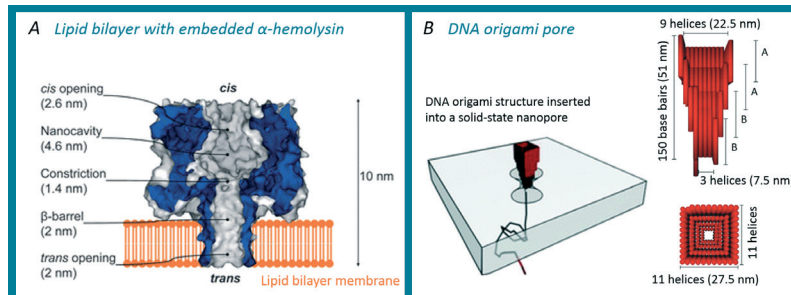


**FIGURE 2.16**

A: cross-section view of an  $\alpha$ -hemolysin pore<sup>[150]</sup>.

B: DNA origami pores inserted into a solid-state NP. The right image is taken from<sup>[151]</sup> and is rearranged.

The polynucleotides translocation studies have prompted also a large number of theoretical treatments of the associated phenomena and effects<sup>[152–154]</sup> and beside  $\alpha$ -hemolysin many other protein pores (like MspA, OmpF, OmpC, etc.) have been explored to this day<sup>[155–157]</sup>. A new and fast growing field of research in context of NPs is the development of DNA origami pores<sup>[26,27]</sup>. The combination of DNA origami and solid-state NPs (see Figure 2.16 B) was first published in 2012<sup>[151,158]</sup>. This technique is very attractive, because it enables the precise construction and design of 3D shapes with full control over geometry and surface functionality<sup>[26]</sup>. The incorporation of such artificial NPs is not restricted to solid-state NPs, but it is also feasible to directly insert them into lipid bilayers<sup>[28,159,160]</sup>. Even though a controlled translocation

(e.g. by optical tweezers) of DNA molecules was repeatedly shown for solid-state NPs<sup>[46,47,49,161]</sup>, this way of translocation at very low controlled velocities is still a missing jigsaw in context of biological pores (to the best of the authors' knowledge). Therefore, the establishment of an experimental setup accessible for both optical tweezers and biopore incorporation into lipid bilayer membranes is one focus of this thesis.

### ***Nanopores for next generation sequencing***

The *first generation sequencing* techniques were based on the Sanger method, presented in 1977<sup>[6]</sup>, followed by the *second generation sequencing* methods, which prevent the necessity of separating the DNA in a gel<sup>[162]</sup>. The actually so-called *next-generation sequencing* (NGS) technology provides short read and high-throughput, and thus has fundamentally altered our understanding of microbiology and has become an integral tool in epidemiology<sup>[8,12]</sup>. Even though the usefulness of whole genome sequencing for public health infection control is obvious, the adoption in clinical microbiology laboratories is still limited<sup>[163]</sup>. The main reason for this is, that short-read methods cannot clearly assemble repetitive elements, which are longer than the sequencing read-length into a single contig. This limits accurate assembly and causes multiple contigs, which leave gaps in the entire genome assemblies<sup>[12]</sup>. In particular, it is very challenging to correctly assemble regions, where genes have been obtained by horizontal gene transfer, like pathogenicity islands and resistance, and prophage<sup>[164]</sup>. Nevertheless, analyzing these regions is crucial for identifying key characteristics like antibiotic resistance and for determining extremely pathogenic bacterial types<sup>[165]</sup>. To close these gaps, extensive and expensive post-sequencing and laboratory-based analysis is currently required. These steps can last months, and thus the final results become irrelevant for (fast) clinical diagnostics and for guiding public health interventions<sup>[12]</sup>. Therefore, DNA sequencing using NP technology is an alternative method for producing long-read sequence data<sup>[11,12]</sup>.

The NP approach provides single-molecule sensitivity and analytical abilities that are accomplished by driving these molecules electrophoretically through a nanometre-scaled pore without prior molecular amplification and necessity for labeling<sup>[11,14,15]</sup>. In general, a NP offers a highly confined volume or channel structure, by which single nucleic acid polymers can be studied at high throughput and in addition, can be in principle detected in a way that the obtained sequence signals reflect the native order of nucleobases in a polynucleotide<sup>[11]</sup>. The prediction of long reads of (kilobase length) polymers provides a unique analytical capability that makes inexpensive, rapid DNA sequencing possible. Thus, this technique offers the prospect of a *third generation technique* that will be able sequence a diploid mammalian genome for  $\sim \$ 1\,000$  in about  $24\ h$ <sup>[11]</sup>. This technology could tap into a brand-new sector of customers (besides basic research and clinical medicine) who need genetic fingerprinting for food safety, forensic science or agricultural biotechnology<sup>[5,9]</sup>.

As one can imagine, this whole NP-based research field is rapidly growing and touches hosts of specified approaches, thus in the following only the most essential and recent contributions (with their pros and cons) are briefly presented. The interested reader is encouraged to see these recent and comprehensive reviews<sup>[5,11,14,138,166–169]</sup>.

Two groups (Cherf et al.<sup>[34]</sup> led by Akeson and Manrao et al.<sup>[35]</sup> led by Gundlach) independently presented in 2012 the first published data showing that sequence information can be truly obtained during DNA translocation through a protein NP. Until then, the most prominent drawback in NP studies was the insufficient high speed of the DNA translocation process for accurate identification of individual bases<sup>[9,11]</sup>. Both groups used a polymerase to address this issue for slowing down DNA translocation through a protein NP, to a velocity that is favorable for reading base-specific current levels. Cherf et al. bound a *phi29 DNA polymerase* to a single-stranded DNA template, which in turn was hybridized to a primer, and threaded the ssDNA end through an  $\alpha$ -hemolysin pore (at an applied voltage). By starting the primer extension via polymerase activity a double-stranded DNA is synthesized, and thus the polymerase acts like a motor pulling the DNA through the pore in single-nucleotide steps<sup>[34]</sup>. Manrao et al. followed the same strategy, however, they utilized the protein pore MspA<sup>[35]</sup>. Even though both groups accomplished the mission to perform DNA translocation at an appropriate rate and with single-nucleotide steps, the obtained current levels could not be unambiguously transferred into single base identification<sup>[9]</sup>. This issue can be (at least partly) attributed to the impact of adjacent nucleotides besides the base of interest, because a small series of nucleotides ( $\sim 10 - 15$  nucleotides) rather than a single base contributes to the current signal<sup>[29,35]</sup>.

The time of publication of these two reports overlapped with a statement of the company *Oxford Nanopore Technologies* at the *Advances in Genome Biology and Technology* conference<sup>1</sup> that set the sequencing field abuzz. They introduced two NP sequencing platforms (GridION and MinION) able to deliver high-throughput, ultra-long sequence reads at low costs<sup>[36]</sup>. In the meantime, several peer-reviewed scientific reports verify these predicted properties. However, there is still much space for further improvements. Their technological approach is in principle very similar to the one of Cherf et al. and Manrao et al. and include the utilization of a polymerase in combination with the  $\alpha$ -hemolysin pore. Ashton et al. showed in 2015 that by applying a MinION sequencer it is feasible to resolve the structure and chromosomal insertion site of a composite antibiotic resistance island in *Salmonella Typhi Haplotype 58*<sup>[12]</sup>. Haplotypes are essential for an accurate interpretation of genetic laboratory studies for medically actionable findings and can often not be resolved by short read sequencing<sup>[38]</sup>. In addition Ammar et al. reported also in 2015 the capability of very long reads to resolve both variants and haplotypes of *HLA-A*, *HLA-B* and *CYP2D6* genes, with data from a single 24-hour NP sequencing run (also with MinION) and without the necessity for statistical phasing<sup>[38]</sup>. Beside the development of this technique itself, also the software-based analysis of the very large and complex datasets make progress<sup>[170]</sup>. With these results, Oxford Nanopore Technologies competes not only with basic research, but directly with the other leading instrument providers for DNA sequencing, such as Carlsbad, Life technologies or Illumina<sup>[36]</sup>. It will be interesting to see how this competition is intensifying in order to push accurate, low-cost sequencing into the clinical space.

Finally, it should be noted that other promising approaches, using the relative new 2D materials made out of graphene, molybdenum disulfide ( $\text{MoS}_2$ ) or carbon nanomembranes (CNMs) exist<sup>[5,16]</sup>. Translocation of DNA through graphene NPs could already

---

1 See also <https://www.nanoporetech.com/news/press-releases/view/39> [30.03.2015, 13:57]

be demonstrated, however, the main disadvantage was the DNA adhering to the NP surface that resulted in high background noise<sup>[171-174]</sup>. Recent progress in this growing field can be found here<sup>[140,175-181]</sup>. Nevertheless, NPs made of graphene present an intriguing alternative to biological and “conventional solid-state” NPs, because it presents the ultimate NP membrane material given its thickness of only a single carbon atom. It also offers electrical conductivity, which opens up new approaches for measuring the traversing nucleotides (e.g. by running a tunneling current transversally through the DNA molecule)<sup>[45]</sup>. To conclude, DNA sequencing by graphene NPs is so far science fiction, however, so was sequencing via biological pores two decades ago.

## 2.6 DNA-Nanopore Force Interaction

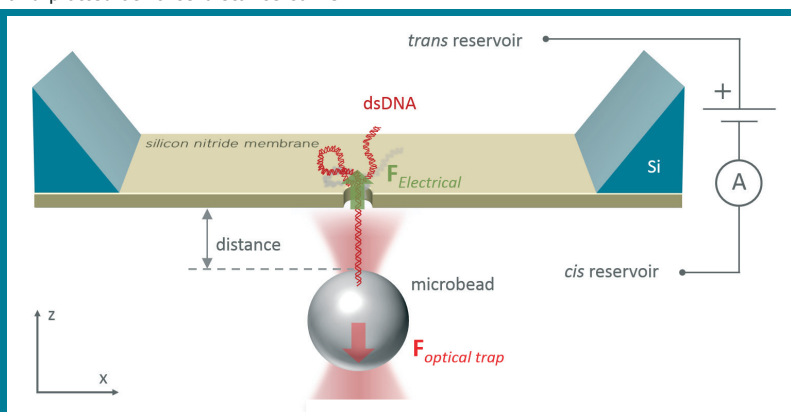
This last chapter deals with the issue of how the previous described effects affect the experimental OT force measurements of single DNA molecules, while threading through a nanopore. Additionally the theoretical dynamics of a DNA molecule within such a NP are introduced.

### 2.6.1 Experimental DNA Threading Force Measurement

The basic situation in context of OT threading force measurements on NP systems is illustrated in Figure 2.17: two compartments filled with aqueous medium are separated by a thin isolating solid-state membrane. The only connection between these two chambers is the NP, which is located in the center of this membrane. A dsDNA strand is immobilized at one end onto the surface of a microbead and according to trapping by OT, this bead is moved into the vicinity of the NP. By the application of a transmembrane voltage the free end of the immobilized dsDNA molecule is forced to thread through the pore. In this situation the dsDNA experiences an electrostatic force, which is compensated by the stiffness of the optical trap and can be measured and plotted as force-distance curve.

**FIGURE 2.17**

Schematic illustration of the basic situation, when a dsDNA molecule (immobilized on a bead) is threaded through a NP via OT, while a transmembrane voltage is applied. The membrane is isolating and separates two compartments filled with aqueous solution. The sketch is drawn inspired by<sup>[161,182]</sup>.



A typical force-distance curve is shown in Figure 2.18 with additional sketches, clarifying which spot in the diagram corresponds to which bead-DNA-NP arrangement. In this case the dsDNA molecule is thread into the NP at a bead-membrane distance

of about  $5 \mu\text{m}$ , followed by stretching the DNA up to a length of  $10.5 \mu\text{m}$  at a constant threading force of about  $5 \text{ pN}$ . Subsequently the DNA is pulled out of the pore and the force drops back to zero piconewton. The height of the measured force depends on several effects and will be discussed by introducing the theoretical electrostatic force experienced by the DNA.

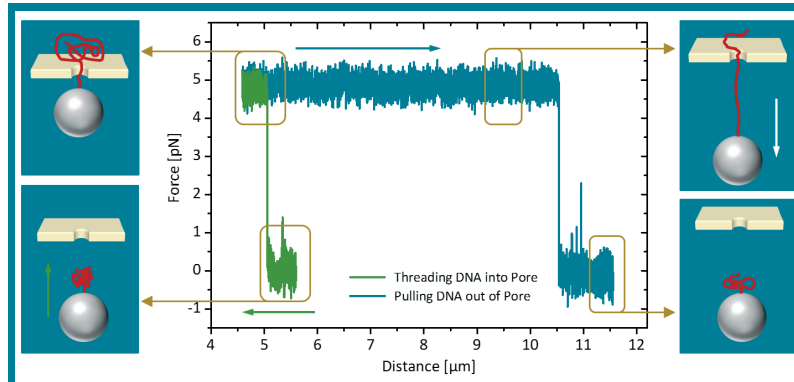


**FIGURE 2.18**

Diagram: Typical relationship between threading force and z-distance, for a whole translocation event. The sketches clarify the process of threading in the dsDNA into the NP and pulling it out again. The original diagram is taken from<sup>[131]</sup>.

The forced movement of a charged particle (such as DNA) relative to a stationary liquid by applying an electric field is in general called electrophoresis (EP)<sup>[183]</sup>. To calculate this electrostatic force  $F_{EP}^{theo}$ , which is theoretically experienced by the DNA molecule, a typical voltage of  $V = 50 \text{ mV}$  and a membrane thickness of  $d = 20 \text{ nm}$  can be considered<sup>[130]</sup>. Given these parameters the electric field is:

$$E = \frac{V}{d} = \frac{50 \text{ mV}}{20 \text{ nm}} = 2.5 \cdot 10^6 \frac{\text{V}}{\text{m}}$$

It is noteworthy, that this field is confined only to the NP, due to the isolating membrane properties. The electrostatic force  $F_{el} = Q \cdot E$  acting on the whole DNA molecule equals the force acting on the few monomers that are situated in the nanopore, and thus can be calculated by taking the charge of this few monomers (two electrons per base) and their length (basepairs distance of  $0.34 \text{ nm}$ ) into account<sup>[46]</sup>:

$$Q = \frac{2 \cdot e^-}{bp} \cdot d = \frac{2 \cdot e^-}{0.34 \text{ nm}} \cdot 20 \text{ nm} = 117,65 \cdot e^- = 1,88 \cdot 10^{-17} \text{ C}$$

With this charge the theoretical applied electrostatic force can be described as:

$$F_{EP}^{theo} = Q \cdot E = 1,88 \cdot 10^{-17} \text{ C} \cdot 2,5 \cdot 10^6 \frac{\text{V}}{\text{m}} = 47 \cdot 10^{-12} \frac{\text{V} \cdot \text{C}}{\text{m}} = 47 \text{ pN}$$

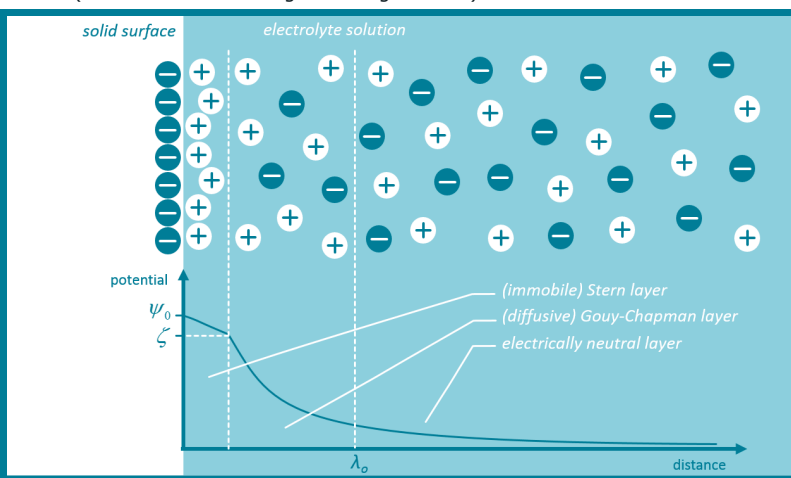
This means, that a threaded dsDNA molecule should experience an electrostatic force of  $47 \text{ pN}$  (under the prevailing conditions) and should be measurable by OT. However, in reality the effective obtainable force  $F_{eff}^{exp}$  (for the same conditions) differs drastically from this value (in general forces  $F_{eff}^{exp}$  in a range of 15–20 % of  $F_{EP}^{theo}$  are recorded)<sup>[46]</sup>. Therefore, several other phenomena affecting the measurable force have to be considered<sup>[130]</sup>.

Not only the DNA exhibits an electrical charge in an aqueous buffer environment, but also the surface of the membrane, and thus also the sidewalls of the NP. This surface charge is caused by dissociation of the silanol groups ( $-\text{Si}-\text{OH}$ ) at the membrane surface (which in turn depends on the present pH value) and can result in an either protonated or deprotonated state ( $-\text{Si}-\text{OH}_2^+$  or  $-\text{SiO}^-$ ). Moreover, the amino groups

(-Si-NH<sub>2</sub>) can also dissociate or partial charges within the material can lead to an adsorption of ions of the buffer<sup>[183]</sup>. The membrane material used in this thesis was silicon nitride (Si<sub>3</sub>N<sub>4</sub>), which is normally positively charged for at  $pH > 5$  and exhibits a negatively charge only at acidic buffer solutions ( $pH < 4$ )<sup>[184,185]</sup>. At experimental conditions ( $pH < 8$ ) the negatively charged membrane surface, causes the formation of positively charged ions of the buffer solution directly at the membrane-buffer interface, as it is depicted in Figure 2.19. This screening phenomena is commonly described as an electrical double layer (EDL) and refers to two parallel layers on top of the membrane surface<sup>[186]</sup>. The first layer directly at the interface is called *Stern layer* and describes an immobile layer of positively charged ions, which are strongly attracted via *Coulomb interaction*. In this region the electrical potential  $\psi$  decreases linearly starting at  $\psi_0$ , the surface potential, to a value  $\zeta$ , the so-called zeta-potential<sup>[187]</sup> (see the imbedded diagram in Figure 2.19).

**FIGURE 2.19**

Sketch of the ionic arrangement near a deprotonated surface, which has been brought into contact with an electrolyte at thermal equilibrium. The electric double layer consist of the immobile Stern layer and the diffusive Gouy-Chapman layer.



With larger distances from the interface, diffusion dominates the weaker Coulomb interaction. This layer is named *Gouy-Chapman layer* and in this regime the potential decreases exponentially. At the *Debye length*  $\lambda_D$  the negatively charged membrane surface is no longer "visible" for the buffer ions and it is a measure for the effectiveness of a surface charge screening<sup>[183,187]</sup>. The Debye length is defined as:

$$\lambda_D = \sqrt{\frac{k_B T \cdot \epsilon_{dp}}{2c_0 \cdot e^2 \cdot Z^2}}$$

This term consists of the thermal energy  $k_B T$ , the medium's dielectric permittivity  $\epsilon_{dp}$ , the ion concentration  $c_0$ , the elementary charge  $e$  and the valence of the ions  $Z$ . Thus, the lower the ionic strength of the solution, the larger is the second layer. Typical values for  $\lambda_D$  are about few nanometres. This double layer situation causes a transport of the loosely bound ions within the Gouy-Chapman layer, due to the electric field during application of a voltage. The remaining fluid (described by the "third" electrically neutral layer) is transported as well, due to viscous drag and inner friction with the forced ions<sup>[183]</sup>. In contrast to a hydrodynamic parabolic flow profile induced by pressure<sup>[188]</sup>, this so called electroosmotic flow (EOF) has a stamp like flow profile<sup>[183,189]</sup>.

This EOF has an opposing orientation compared to the EP, which is forcing the DNA into the NP direction. The velocity  $v_{EOF}$  can be described as<sup>[183]</sup>:

$$v_{EOF} = \frac{\epsilon_{dp} \cdot \zeta \cdot E}{\eta} = \mu_{EOF} \cdot E$$

and depends on the electrophoretic mobility  $\mu_{EOF} = \epsilon_{dp} \zeta / \eta$ . This velocity decreases either with reducing pH and temperature or increasing ionic strength of the solution, because then the surface charge, respectively the Debye-length is lowered<sup>[136]</sup>.

As already indicated the EOF causes drag force  $F_{EOF}$ , which opposes the bare electrostatic force  $F_{EP}^{theo}$ , leading to an effective measurable force  $F_{eff}^{exp} = F_{EP}^{theo} - F_{EOF}$ <sup>[47]</sup>. In case of OT measurements  $F_{eff}^{exp}$  is balanced by an opposing mechanical force  $F_{OT} = -F_{eff}^{exp}$ , which arrests the DNA in position inside the NP<sup>[47]</sup>. A typical value describing the reduction of the force is  $F_{EOF}/F_{EP}^{theo} = 0.9$ , i.e. a reduction of 90 %. Ghosal et al. presented in 2007 a theoretical simulation showing in which form such a reduction level depends on the ion concentration and varying surface charge densities<sup>[190]</sup> (see Figure 2.20 A). As expected,  $F_{EP}^{theo}$  is more reduced for larger surface charge densities  $\sigma_m$ , caused by a stronger EOF. At a high salt concentrations the force reduction is approximately constant (at given  $\sigma_m$ ), but for lower ionic strengths (<0.3 M KCL) the decrease is significantly lower, due to overlapping Debye-lengths of the NP wall and the DNA (at such a small NP of 5 nm in diameter)<sup>[190]</sup>.

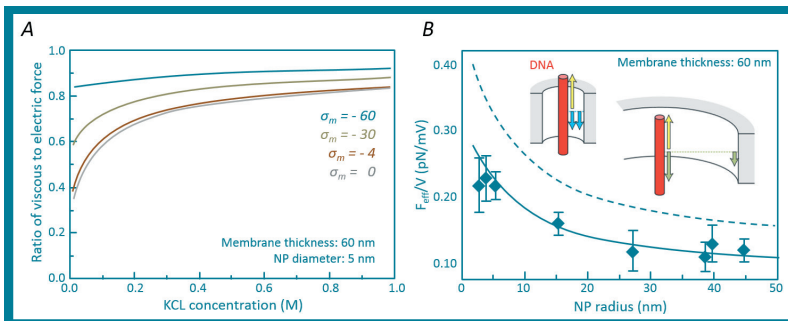


**FIGURE 2.20**

A: Dependency between  $F_{EOF}/F_{EP}^{theo}$  and ion concentration simulated for different surface charges  $\sigma_m$  (in  $mC/m^2$ )<sup>[190]</sup>. B: Effective force versus pore radius<sup>[47]</sup>. For better print quality and readability both diagrams are redrawn. The original data can be found in the referenced work of Ghosal<sup>[190]</sup> and von Dorp et al.<sup>[47]</sup>.

By transferring these theoretical findings to experimental observations, one has to take into account, that the surface charge itself depends on the ionic strength, and thus on the pH (according to the respective membrane material). Under experimental conditions and for silicon-nitride membranes  $\sigma_m$  can typically be estimated to be in the range between  $-15$  and  $-60 mC/m^2$  as described in the literature<sup>[191-195]</sup>. Another source of influence onto  $F_{eff}^{exp}$  is the geometry of the NP, which is also affected by the EOF. If the NP walls are rough, the EOF is decreasing, and thus the  $F_{eff}^{exp}$  is larger. In addition, the size of the NP is crucial, especially for small NPs (<10 nm in diameter), because of the mentioned overlap of the Debye-lengths of DNA and NP wall. This overlap causes a less pronounced EOF, and thus an increasing  $F_{eff}^{exp}$  that was presented by Van Dorp et al. in 2009. In Figure 2.20 B their finding is presented<sup>[47]</sup>, where the theoretically estimated  $F_{EP}^{theo}$  is additionally plotted (dashed line). The two insets visualize the bare electrostatic forces (arrow up) and the drag forces caused by the EOF (arrow down). Due to the fact that both, the drag force and the electrostatic force are proportional to existing electric field, the experimental observable force  $F_{eff}^{exp}$  is proportional to the applied voltage.

## 2.6.2 Theoretical Dynamics of DNA in a Solid-State Nanopore

According to the above introduced explanation attempt for qualitatively understanding the observable phenomenon, a more detailed look behind the theoretical model<sup>[182]</sup> (which is later applied for discussing experimental results in chapter 4.1.2) is given in this chapter<sup>1</sup>.

To recapitulate the key message, the dynamics of a single DNA molecule situated in a solid-state NP are governed by a complex relationship of several electrohydrodynamic effects<sup>[47,196–199]</sup>. As introduced above, the externally applied voltage induces an electrophoretic force on the charged molecule as well as an EOF of the surrounding buffer solution<sup>[191,200]</sup>. Furthermore, substantial forces are caused by counter-ion pressure<sup>[201,202]</sup>, self-energy<sup>[203,204]</sup>, concentration polarization<sup>[205]</sup>, and numerous charge-induced or non-linear electrokinetic effects<sup>[206]</sup>. These particular effects are fully contained in the following theoretical model approach.

Because of the insulating membrane property, the numerous electrohydrodynamic factors noted above are most prominent within the NP and in its immediate proximity<sup>[47,206]</sup>. Nevertheless, for distances  $d_o$  from the NP, which are significantly larger than the diameter of the NP, the electric as well as the EOF field decrease with  $1/d_o^2$ <sup>[198]</sup>. Thus, this slow algebraic decay cannot be neglected, because these fields still exhibit a distinct contribution for the net (integrated) force (acting on a charged and elongated object like DNA). As a consequence, theoretical findings for NPs with infinite length<sup>[50,191,207]</sup> exhibit a limited dependability for the quantitative analysis and interpretation of experimentally obtained forces. Moreover, a significant theoretical model (in this context) has to consider appropriate dimensioned fluid “reservoirs” above and below the desired NP region, as will be presented in the following.

The fundament of this model constitutes the well-established framework of the coupled *Nernst-Planck*, *Poisson*, and *Stokes equations*<sup>[202,208–210]</sup>, which is briefly summarized in the following (a more detailed account see e.g.<sup>[202]</sup>). Within a buffer solution, the electric potential  $\psi(\mathbf{x})$  satisfies Poisson’s equation  $\varepsilon_s \Delta \psi(\mathbf{x}) = -\rho(\mathbf{x})$ , where  $\rho(\mathbf{x}) = F_c [c_+(x) - c_-(x)]$  is the total charge density, which is based on the local ion concentrations  $c_{\pm}(x)$  of the dissolved  $K^+$  and  $Cl^-$  ions,  $\varepsilon_s = 80\varepsilon_0$  describes the buffer permittivity, and  $F_c$  is Faraday’s constant. An elongated rod-shaped particle models the DNA molecule and considers a homogeneous surface charge density  $\sigma_p$  (which is equivalent to 2 electron charges per base pair of a real dsDNA). The Poisson’s equation inside the particle can be described as  $\Delta \psi(\mathbf{x}) = 0$  and is completed by the standard boundary condition  $\mathbf{n} \cdot [\varepsilon_s \mathbf{E}_s - \varepsilon_p \mathbf{E}_p] = \sigma_p$  at the interface between particle and solution<sup>[202,211]</sup>. Here,  $\mathbf{n}$  represents the surface normal,  $\mathbf{E}_{s/p}$  the present electric field at the respective sides of the interface ( $\mathbf{E}(\mathbf{x}) = -\nabla \psi(\mathbf{x})$ ) and  $\varepsilon_p$  the permittivity of the particle, which is in the following approximated as  $\varepsilon_p = 2\varepsilon_o$ . Inside the membrane the Poisson’s equation is described analogously, with  $\Delta \psi(\mathbf{x}) = 0$  and  $\mathbf{n} \cdot [\varepsilon_s \mathbf{E}_s - \varepsilon_m \mathbf{E}_m] = \sigma_m$  at the membrane-solution interface (with the surface charge density of the membrane  $\sigma_m$  and its approximate permittivity  $\varepsilon_m = 2\varepsilon_o$ ). Additionally, the experimentally applied voltage of 50 mV is considered by introducing the boundary conditions  $\psi = 0$  V at the bottom electrode and  $\psi = 50$  mV at the top electrode (corresponding to top and bottom

1 This theoretical model was developed by Andreas J. Meyer and Peter Reimann from the *Condensed Matter Theory Group* at Bielefeld in close cooperation and was published in 2014<sup>[182]</sup>.

boundaries sketched in Figure 2.21 A). Due to their minor relevance, the specific properties of the reservoir side walls are represented by the boundary condition  $\mathbf{n} \cdot \mathbf{E}(\mathbf{x}) = 0$  [211].

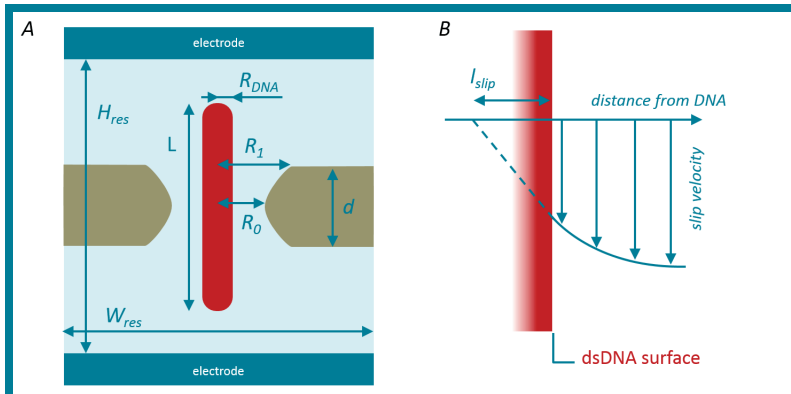


**FIGURE 2.21**

A: Schematic illustration of the main arrangement and dimensions used in the theoretical model<sup>[182]</sup>. The entire setup is rotationally symmetric about the particle axis with overall height  $H_{res}$  and diameter  $W_{res}$ .

B: Sketch visualizing the slip velocity and slip length  $l_{slip}$ , when no-slip boundary conditions are adopted to<sup>[212]</sup>.

The flux densities  $\mathbf{J}_{\pm}(\mathbf{x})$  of the two ionic species is expressed by the Nernst-Planck equation  $\mathbf{J}_{\pm}(\mathbf{x}) = c_{\pm}(\mathbf{x})\mathbf{u}(\mathbf{x}) + \mu_{\pm}c_{\pm}(\mathbf{x})\mathbf{E}(\mathbf{x}) - D_{\pm}\nabla c_{\pm}(\mathbf{x})$  in terms of their diffusion coefficients  $D_{\pm}$ , their concentrations  $c_{\pm}(\mathbf{x})$ , the fluid-velocity field  $\mathbf{u}(\mathbf{x})$  and their mobilities  $\mu_{\pm} = q_{\pm}D_{\pm}/k_B T$  [208]. Within the last term  $q_{\pm} = -q_{\pm} = e$  describe the ion charges for  $Cl^{-}$  and  $K^{+}$ ,  $k_B$  is Boltzmann's constant,  $T = 293$  K the temperature and  $e$  is the electron charge. In the stationary state ( $\nabla J_{\pm}(\mathbf{x}) = 0$ ) the boundary conditions are  $c_{\pm}(\mathbf{x}) = c_0$  at the electrodes and  $\mathbf{n} \cdot \mathbf{J}_{\pm}(\mathbf{x}) = 0$  at all remaining boundaries<sup>[202,208]</sup>. Here,  $c_0$  represents the experimentally determined bulk concentration of the ions with a large distance from the membrane.

With  $\nabla \mathbf{u}(\mathbf{x}) = 0$  (i.e., the fluid is incompressible) and  $\eta = 8 \cdot 10^{-4}$  Pa·sec (viscosity of water at room temperature), the velocity of the fluid  $\mathbf{u}(\mathbf{x})$  and the corresponding pressure  $p(\mathbf{x})$  satisfy Stokes' equation  $\eta \Delta \mathbf{u}(\mathbf{x}) = \Delta p(\mathbf{x}) - p(\mathbf{x})\mathbf{E}(\mathbf{x})$  [208]. In addition, a vanishing normal stress  $\mathbf{A} \cdot \mathbf{n} = \boldsymbol{\theta}$  is presumed at the electrode boundaries (with  $\mathbf{A}$  the hydrodynamic stress tensor and its corresponding components  $A_{ij} = \eta(\partial u_i / \partial u_j + \partial u_j / \partial u_i) - p\delta_{ij}$ ) [208]. Whereas standard no-slip boundary conditions  $\mathbf{u}(\mathbf{x}) = \boldsymbol{\theta}$  are adopted at the side walls of the reservoirs and the membrane surfaces. It is noteworthy, that this boundary condition also apply for a potentially lipid bilayer-coated NP. Though such a coating resembles a movable 'fluid wall', its low diffusion coefficient ( $D_{POPC} = 1.34$  nm<sup>2</sup>/μsec)<sup>[51]</sup> and charge neutrality induces no directed motion under experimental conditions (applied voltage of 50 mV).

Regarding the particle surface, no-slip boundary conditions are a priori not established and instead, the possibility of non-negligible hydrodynamic slip effects is enabled<sup>[182]</sup>. For this reason, the more general, so-called *Navier boundary conditions*  $\mathbf{u}_{\parallel} = l_{slip} \partial_{\perp} \mathbf{u}(\mathbf{x})$  and  $\mathbf{u}(\mathbf{x}) \cdot \mathbf{n} = 0$  are utilized, where  $\mathbf{u}_{\parallel}$  describes the slip velocity parallel to the surface,  $l_{slip}$  denotes the so-called slip length, and  $\partial_{\perp} \mathbf{u}(\mathbf{x})$  the derivative of the velocity field along the direction, which is normal to the particle surface (compare to Figure 2.21)<sup>[212]</sup>.

According to solving these coupled partial differential equations, the key observable in the experiment, namely the net electrohydrodynamic force  $F_{eff}^{exp}$  acting on the particle (dsDNA molecule), can be straightforwardly obtained as the integral  $\mathbf{F}_{eff}^{theo} = \int_S [\mathbf{A}(\mathbf{x}) + \mathbf{M}(\mathbf{x})] \mathbf{n} dS$  over the particle surface  $S$ . Here,  $\mathbf{A}$  is the hydrodynamic stress tensor (see above) and  $\mathbf{M}$  the Maxwell stress tensor with its components  $M_{\underline{uv}} = \varepsilon \left( E E - \delta |\mathbf{A}|^2 / 2 \right)$ .<sup>[211]</sup>

The above-mentioned Nernst-Planck, Poisson and Stokes equations are solved numerically, considering a rotationally symmetric geometry as sketched in Figure 2.21. The dimensions of the total system (cylindrical container) exhibit a height of  $H_{res} = 1 \mu m$  and a diameter of  $W_{res} = 2 \mu m$ . Additionally, it was verified that larger values did not have a noticeable impact on the results<sup>[182]</sup>. The given membrane thickness is  $d = 20 nm$  in case of the bare silicon nitride membrane, and  $d = 30 nm$  in case of the potentially existing lipid-coated membrane (varying  $d$  between  $10 nm$  and  $60 nm$  changed the results by not more than 3 %). The characteristic hourglass shape of the NP was approximated as hyperboloids with maximal and minimal radii  $R_1$  and  $R_0$  (see Figure 2.20 and<sup>[213]</sup>; furthermore, the intersection between hyperboloid and flat membrane was slightly "rounded"). For the minimal radius  $R_0$  in this model the experimentally estimated pore radius was adopted, whereas the maximal pore radius  $R_1$  was relative connected to  $R_0$  by  $R_1 = R_0 + d/10$  (further realistic selections of  $R_1$  varied the results by less than 5 %).

The dsDNA molecule was theoretically modeled as a rod-shaped particle of radius  $R_p = 1.1 nm$  and length  $L = 2l_{Kuhn} + d$  with a Kuhn length of  $l_{Kuhn} \approx 100 nm$  (=2 · persistence length of dsDNA), and thus approximating the respective literature values for dsDNA<sup>[199,214]</sup>. In addition, a homogeneous surface charge density of the (DNA) particle  $\sigma_p = -2e / (0.34 nm \cdot 2\pi \cdot 1.1 nm)$  was adopted (with the dsDNA circumference of  $2\pi \cdot 1.1 nm$ ). The position of the rod-shaped DNA-molecule was symmetrically along the pore axis, whereas both ends stuck out of the pore by  $l_{Kuhn}$ . Once again, it was tested by further increasing the rod length, that  $F_{eff}^{theo}$  persist nearly unchanged. Taking for granted that the dsDNA molecule can be satisfactorily approximated by such rigid rod (a detailed discussion can be found here<sup>[182]</sup>), there still exist the possibility that the rod axis may differ from the pore axis. These thinkable deviations were also verified to only have a minor effect on  $F_{eff}^{theo}$ , both for the uncoated and potentially coated NPs.

## 3 Materials and Methods

For understanding and reproducing the experiments and results, which will be presented in the fourth chapter, this section gives an overview on the technical requirements and experimental preparations executed within the scope of this thesis.

At first a list of all chemicals and materials is presented, followed by a brief introduction of the optical tweezers (OT) and fluorescence microscopy setup. At least four different methods concerning the modification of the nanopores (NPs) by means of lipid mono- or bilayers are discussed.

### 3.1 Chemicals and Materials

The following tables list all chemicals, reagents, lipids and laboratory equipment and material for the experiments in this thesis.

| Chemical / Reagents  | Manufacturer          |
|--|-----------------------|
| 1-hexanol (C <sub>6</sub> H <sub>14</sub> O)                               | Alfa Aesar, GER       |
| Acetone (p.a.)   | VWR, GER              |
| Calcium chloride (CaCl <sub>2</sub> )                                      | Sigma-Aldrich, GER    |
| Chloroform (ChCl <sub>3</sub> )  | VWR, GER              |
| Deionized water, $\chi=0.3$ mS/cm (MilliQ®)                                | Millipore, USA        |
| Ethanol (p.a.)   | VWR, GER              |
| HEPES (C <sub>8</sub> H <sub>18</sub> N <sub>2</sub> O <sub>4</sub> S)     | Sigma-Aldrich, GER    |
| Hydrogen chloride (HCL)  | Sigma-Aldrich, GER    |
| Hydrogenperoxide (H <sub>2</sub> O <sub>2</sub> ), 30%                     | VWR, GER              |
| Isopropyl alcohol (p.a.)   | VWR, GER              |
| Natriumchloride (NaCl)   | VWR, GER              |
| n-Decan (CH <sub>3</sub> (CH <sub>2</sub> ) <sub>8</sub> CH <sub>3</sub> ) | Merck Schuchardt, GER |
| Nitrogen (p.a.)  | Linde, GER            |
| Oxygen (p.a.)  | Linde, GER            |
| Pentane (CH <sub>3</sub> (CH <sub>2</sub> ) <sub>3</sub> CH <sub>3</sub> ) | Sigma-Aldrich, GER    |
| Polydimethylsiloxane Sylgard 184 (PDMS)                                    | Dow Corning, USA      |
| Potassium chloride (KCL)   | VWR, GER              |
| Potassium ferrocyanide (K <sub>4</sub> [Fe(CN) <sub>6</sub> ])             | VWR, GER              |
| Sucrose (C <sub>12</sub> H <sub>22</sub> O <sub>11</sub> )                 | Roth, GER             |
| Sulfuric acid (H <sub>2</sub> SO <sub>4</sub> ), 96%                       | VWR, GER              |
| TDTS (Tridecafluor-1,1,2,2-tetra-hydrooctyl-trichlorsilan)                 | ABCR, GER             |
| Tris(hydroxymethyl)aminomethane (TRIS)                                     | Roth, GER             |
| Zinc chloride (ZnCl <sub>2</sub> )   | Roth, GER             |
| $\alpha$ -Hemolysin from <i>Staphylococcus aureus</i>                      | Sigma-Aldrich, GER    |

| DNA / Microbeads   | Manufacturer                  |
|--|-------------------------------|
| „DNA Filter“ Ultra-0.5 50 kDa Ultracel Filter                                  | Amicon™, USA                  |
| DNA Oligomeres (5'-AGGTCGCCGCC-3', 432 ng/μl,)                                 | Metabion, GER                 |
| DNA Oligomeres (5'-GGGCGGCGACCT-3', 543 ng/μl)<br>tagged with biotin molecules | Invitrogen™, USA              |
| Streptavidine-polystyrene microbeads (3.05 μm)                                 | Kisker Biotech, GER           |
| λ-DNA (500 ng/μl)  | New England Biolabs Inc., USA |

| Lipids   | Manufacturer             |
|--|--------------------------|
| Cholesterol  | Sigma-Aldrich, GER       |
| DOPE (1,2-dioleoyl-sn-glycero-3-phosphoethanolamine)   | Avanti Polar Lipids, USA |
| DOPG (1,2-dioleoyl-sn-glycero-3-phospho-(1'-rac-glycerol))                                   | Avanti Polar Lipids, USA |
| DOPS (1,2-dioleoyl-sn-glycero-3-phospho-L-serine)  | Avanti Polar Lipids, USA |
| DPhPC (1,2-diphytanoyl-sn-glycero-3-phosphocholine)  | Avanti Polar Lipids, USA |
| DOPC (1,2-dioleoyl-sn-glycero-3-phosphocholine)  | Avanti Polar Lipids, USA |
| DPCC (1,2-dipalmitoyl-sn-glycero-3-phosphocholine)   | Sigma-Aldrich, GER       |
| POPC (1-palmitoyl-2-oleoyl-sn-glycero-3-phosphocholine)                                      | Avanti Polar Lipids, USA |
| POPG (1-palmitoyl-2-oleoyl-sn-glycero-3-phospho-(1'-rac-glycerol))                           | Avanti Polar Lipids, USA |
| Rhod-DOPE (1,2-dioleoyl-sn-glycero-3-phosphoethanolamine-N-(lissamine rhodamine B sulfonyl)) | Avanti Polar Lipids, USA |

| Laboratory Equipment                                | Manufacturer                               |
|---|--|
| Bilayer slide                                       | Inovation, GER                             |
| Bilayer slide holder & movable carriage             | Self-constructed                           |
| Centrifuge 5417 C                                   | Eppendorf, GER                             |
| Desiccator  | DURAN, Germany                             |
| HIM (Helium ion microscope ORION PLus)              | Carl Zeiss AG, Germany                     |
| Magnetic Stirring Hotplate MR 3001 K                | Heidolph, GER                              |
| Microscope slides (24 mm x 60mm x (0.13 - 0.17) mm) | Menzel-Gläser, GER                         |
| Oxygen - plasma chamber                             | Self-constructed, see <sup>[215,216]</sup> |
| Rotary evaporator RV 05                             | Janke & Kunkel, GER                        |
| Thermocycler "Uno Cycler"                           | VWR, GER                                   |
| Ultrasonic homogenizer (Sonopuls MS 72)             | Bandelin, GER                              |
| Vortex-Genie 2                                      | Scientific Industries, USA                 |

| Microchips  | Manufacturer              |
|---|---------------------------|
| Silicon microchips (5 mm x 5 mm)<br>with silicon nitride membrane (200 μm thin) | Silson, UK                |
| Silicon microchips (3 mm x 3mm)<br>with silicon nitride membrane (20 nm thin)   | Structure Probe Inc., USA |
| Silicon microchips (3 mm x 3mm)<br>with silicon nitride membrane (10 nm thin)   | Norcada Inc, CAN          |

| Laboratory Material  | Manufacturer             |
|--|--------------------------|
| Acrylic glass  | Miscellaneous            |
| Cleanroom wipers   | ITW Contamination, China |
| Conductive silver paint  | Sigma-Aldrich, Germany   |
| Disposable dental needle ( $\varnothing$ 0.5 mm x 40 mm)         | Braun, GER               |
| Glass capillaries (borosilicate $\varnothing$ 0.78 mm)           | Harward Apparatur        |
| Glass syringe (10 ml; H-C 1/4"-28UNF/6 PTFE)                     | ILS, Germany             |
| Glass vials (1 ml)   | VWR, GER                 |
| ITO (indium tin oxide) coated glass slides                       | Sigma-Aldrich, Germany   |
| Platinum wire ( $\varnothing$ = 0.4 mm)                          | VWR, GER                 |
| Reservoir puncher ( $\varnothing$ 1.5 mm and $\varnothing$ 4 mm) | Self-constructed         |
| Round-bottom flask (10 ml)                                       | VWR, GER                 |
| Single use syringes (1 ml, 5 ml and 10 ml)                       | Braun, GER               |

## 3.2 Experimental Setup

The main experimental setups are presented in the next two chapters. First, the optical tweezers microscope and its basic development are described, followed by an introduction to the utilized fluorescence microscopy setup.

### 3.2.1 Optical Tweezers

An inverted microscope and a powerful infrared laser constitute the core of the optical tweezers (OT) setup. A unique feature of OT is the contactless manipulation and force measurement of dielectric microparticles with subpiconewton force resolution<sup>[111,113]</sup>. These external forces that act on a trapped particle can be quantified by detecting the particle position with high spatial as well as temporal resolution. The lateral force (x- and y-direction) can be determined by utilizing forward or backscattered light of the trapped particle and guiding it onto a position sensitive detector. To measure the axial force (z-direction) the intensity of the forward or backscattered light has to be detected<sup>[217-219]</sup>. Collection of the forward scattered light is less advantageous than measuring the backscattered light. The forward scattered light has to be collected by means of a condenser lens and be confocally adjusted to the trapping objective, and thus the versatility of the setup is strongly limited<sup>[220]</sup>. This restriction can be surmounted by utilizing backscattered light<sup>[217,218]</sup>. However, it should be noted that disturbing force interference effects can occur when this system is operated in the vicinity of optical interfaces (like a silicon nitride membrane). Sischka et al. demonstrated that it is feasible to partially suppress these interference effects by improving the optical setup<sup>[218]</sup>. An innovative development of the OT setup, recently presented by Knust et al.<sup>[131]</sup>, deals with a video-based image analysis of the trapped particle for position detection as well as force measurement. With this technique, using standard CCD camera operated at moderate light illumination (with negligible sample heating), high force resolution in the axial direction was achieved<sup>[131]</sup>.

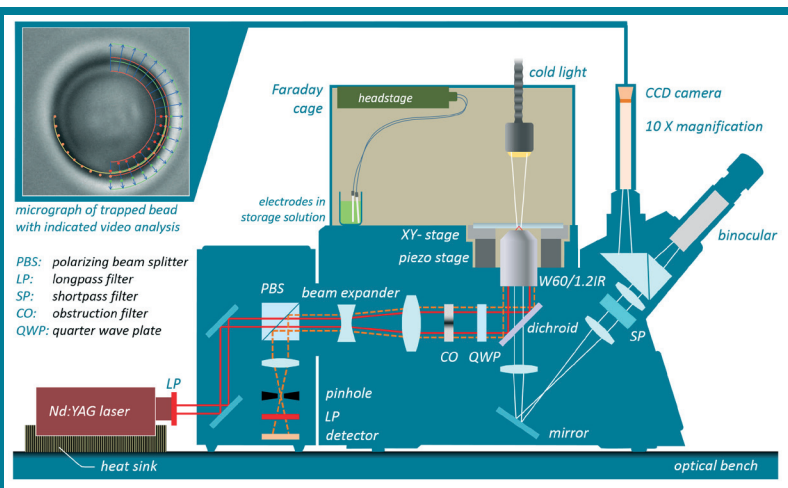
### Optical tweezers system

The OT setup shown as a schematic in Figure 3.1 includes both the backscattered light technique and the video-based image analysis. In the following text the setup and its main components are briefly introduced a more detailed description (including manufacturer information) can be looked up in these publications<sup>[128,131,218,221]</sup>. The P-polarized beam (red line) of a Nd:YAG-laser (1 W, 1064 nm) initially passes a long-pass filter (1064 nm) and a polarizing beam splitter cube before it is expanded to a diameter of 9 mm. Next, it is turned into right-circularly polarized light via a quarter wave plate, and finally focused by a water immersion objective (60x, NA 1.2) into the sample chamber, creating the OT trap. Once a particle is trapped, the backscattered light (orange dashed line) from it is collected by the objective, turned into a parallel light beam again and reflected by a dichroic mirror. The light changes into linearly S-polarized light after passing the quarter wave plate and subsequently, the polarizing beam splitter cube reflects the beam onto a photodetector (utilizing a confocal projection through a longpass filter).

**FIGURE 3.1**

Scheme of the OT setup, illustrating the main components required for OT force recording via backscattered light detection and video-based image analysis.

A detailed description of the process is given in the main text. The inset shows a micrograph of a trapped bead and is taken from<sup>[131]</sup>.



Once an external force (in the z-direction) acts on a trapped particle, it will be slightly deflected out of the beam focus. This leads to a change of the backscattered light intensity, which can be translated into force values (according to prior calibration). To reduce disturbing backscattered interference effects, a central obstruction filter is placed into the light path next to the quarter wave plate. In addition, this filter forms a doughnut-like laser beam, which also enhances the force constant in the z-direction<sup>[218]</sup>. Two short pass filters are placed in the path of the visible light (white line) to protect eyes and camera. The sample chamber is placed on a micrometer-precise manual stage (for coarse adjustment) and can be additionally position controlled by means of a piezo stage (with nanometre precision). Hence, it is feasible to move a trapped particle (or microbead) relative to the sample chamber. A metal box acts as a Faraday cage and enables undisturbed recording of very small ionic currents (see also Figure 3.2 A).

The sample chamber reservoirs are electrically contacted by "glass capillary electrodes". These electrodes are filled with agarose gel and a cyanoferrat salt bridge and

they contain a platinum wire, which is connected (via a headstage) to a patch-clamp amplifier (image B). To illuminate the sample chamber, a high power cold light source (1000 *lm*) is placed about 2 *cm* above the top of the chamber inside the Faraday cage.

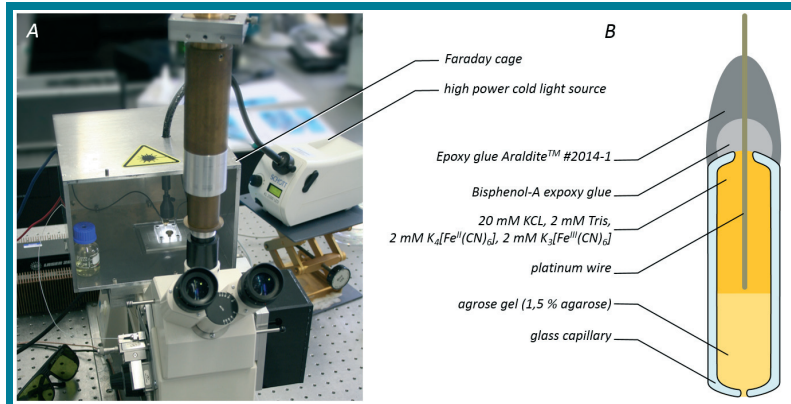


**FIGURE 3.2** Photograph of the OT setup with inverted microscope, Faraday cage and cold light illumination (A). Schematic illustration showing the structure and contents of a glass capillary electrode (B).

### Video-based force analysis

The region of interest of the sample chamber, including a trapped microbead, can be observed by the microscope binocular, while an image of the microbead is projected to the focal plane of the CCD camera by means of a custom-build post magnification (factor 10). This magnification is mandatory for a sufficient high lateral resolution of the microbead's image, which in turn is required for proper analysis of the axial force acting on the bead. Additionally, the bead's image has to be continuously monitored, which is possible with a maximum frame rate of 123 frames per second in real-time<sup>[131]</sup>. The complete image analysis is software-based using a CPU with six cores and twelve parallel threads. To precisely determine the apparent size of a trapped bead in the focal plane, specific edges in each single image are searched, as illustrated in the inset micrograph in Figure 3.1. Hence, the strongest rising (green) and falling (red) edges along 360 circular spokes (blue) are identified<sup>1</sup> and the middle position between these two edges is determined. The apparent size of the microbead is gathered by fitting a circle through these points. This apparent size decreases<sup>2</sup> when a positive external force acts on the bead and deflects it axially inside the optical trap. The force calibration of the OT is executed using the drag force via Stokes' law, while moving the piezo in z-direction with a defined velocity.

A LabVIEW software combines total control over piezo stage movement, force calibration and recording, applied voltage, measuring the ionic current and illumination intensity<sup>3</sup>.

1 These edges are identified, if both exceed a specific threshold value. Additionally they have to be in a consistent relation to each other, which means that the rising edge is further away from the bead's center than the falling edge<sup>[131]</sup>.

2 This applies for utilizing polystyrene beads. Using silica beads instead, the apparent size increases at positive applied external forces.

3 This software was primarily coded by Dr. Andy Sischa and developed further by B.Sc. Sebastian Knust.

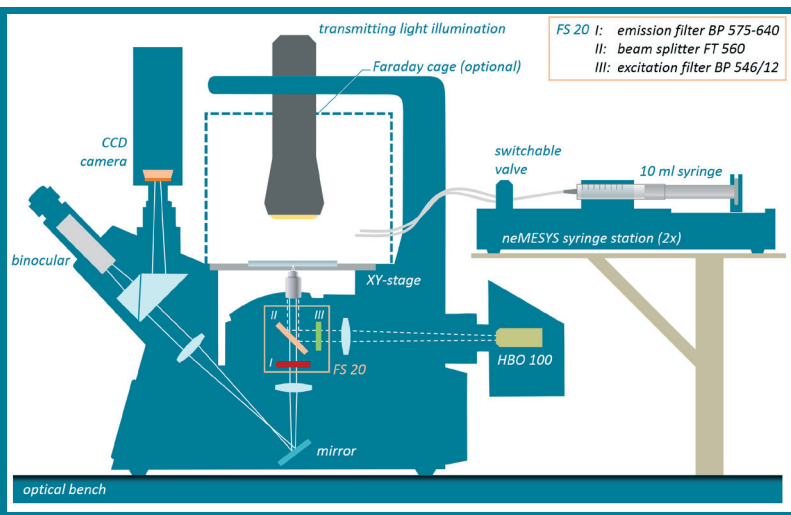
### 3.2.2 Fluorescence Microscopy

The central elements of this setup are an inverted fluorescence microscope (Axiovert 200, Zeiss, Germany) and a low-pressure syringe pump unit (neMESYS, Cetoni, Germany), which can be seen in Figure 3.3. The microscope is equipped with a 100 W mercury short arc lamp (HBO 100, Zeiss, Germany) at its backport, a 40X objective (LD Achromplan, Zeiss, Germany) and a fluorescence filter set to enable fluorescent imaging of labeled phospholipids. The filter set (FS 20, Zeiss, Germany) consists of an excitation filter (BP 546/12), a beam splitter (FT 560) and an emission filter (BP 575-640). This filter set was selected for accurate observation of lipids which are labeled with Rhodamine B (excitation wavelength 543 nm, emission wavelength 565 nm). Non-fluorescent objects are illuminated by a halogen white lamp (30 W), which is installed on top of the sample with a condenser lens in front. The sample chamber is placed onto an automatically movable stage (99S008, Ludl Electronics, USA), controllable either by software or manually by a joystick. For the same reasons as described for the OT setup, a custom built Faraday cage can be optionally placed on top of the stage (see also Figure 4.26). A CCD camera (Imager 3LS, LaVision, Germany) is installed at the microscope's primary camera port and controlled by the software Davis 6.2 for image acquisition.

For electrical connection either the glass capillary electrodes (compare Figure 3.2) for GUV bursting observation or chlorinated platinum wires for the work with the Bilayer Slide are used. For applying voltage and ionic current recording a patch-clamp amplifier (BC-525A, Warner Instrument Corp., USA) was additionally integrated in the course of this work and controlled by a LabView software.

**FIGURE 3.3**

Scheme of the fluorescence microscopy setup. The fluorescence imaging is conducted with filter set 20, to observe the fluorophore Rhodamine B. A syringe unit (controllable by software) for perfusion experiments is installed next to the microscope.



#### Syringe pump unit

For perfusion of the Bilayer Slide channels, two low-pressure syringe pumps are utilized (see Figure 3.3) in combination with the neMESYS UserInterface software. Both glass syringes (10 ml volume) are connected to two microtubes via a switchable valve, respectively, and can be controlled individually by the software. The four

microtubes end at tube connectors integrated in a mobile carriage, which fits onto the Bilayer Slide holder (for more details see chapter 3.3.4).

### 3.3 Nanopore Modification

In context of this thesis, nanopore modification represents the ability to alter a solid-state surface by using lipid bilayers in two different ways. On the one hand, lipid bilayers can act as a surface coating and therefore, change (e.g.) the surface charge properties. On the other hand, freestanding lipid bilayers could be generated to span across a pore, and thus provide a biological environment for later incorporation of biopores. In the following chapters the experimental methods are introduced that were utilized to implement these two different approaches in nanopore modification.

#### 3.3.1 Preparation of Lipid-Coated Nanopores

A custom made and well-established sample chamber design was used to investigate lipid bilayer coated NPs<sup>[161]</sup>. The principle design and structure is illustrated in Figure 3.4. The basic component consists of three layers. A 40  $\mu\text{m}$  thick PDMS sheet with a channel structure (0.5 mm wide and 26 mm long) was sandwiched between a glass coverslide and another PDMS sheet with punched access holes as a channel top cover (see photograph A and sketch C). The sides of both PDMS sheets, which face towards each other, were functionalized by oxygen plasma and thereby bond covalently prior to assembly. The silicon nitride chip was placed centrally on top of the channel above the middle access hole. To enlarge the reservoirs of the (*cis*) channel and the *trans* compartment two extensions made of PMMA were mounted on top. Part one fits to both *trans* reservoirs and part two seals the silicon nitride chip by utilizing a PDMS ring in between (see Figure 3.4 B and D). This structure features, in combination with a mounting plate (image B), a very stable and easy to handle sample chamber.

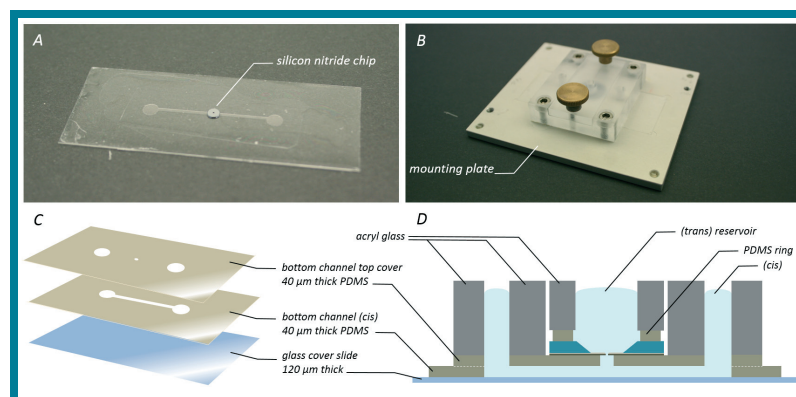


**FIGURE 3.4** Photographs showing the channel structure (A) and assembled sample chamber (B). Additionally, schemes of the structure with size and material information are presented (C and D).

#### Nanopore fabrication

A silicon chip was utilized as a carrier medium for the NPs; this approach is traditionally used in the context of electron microscopy. The chip had a diameter of about 3 mm, is 200  $\mu\text{m}$  thick and contained a square window with a typical size of

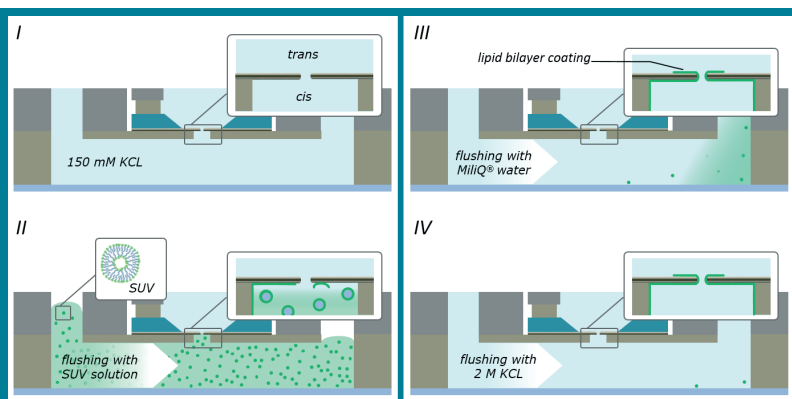
60  $\mu\text{m} \times 60 \mu\text{m}$  (compare chapter 2.5 and Figure 2.15). The lower side of the chip, and thus the window area, is covered with a 20 nm thin silicon-nitride membrane (10 nm and 50 nm thick membranes were also used in this thesis). A single NP with a typical diameter between 15 and 80 nm was milled by helium ion microscope (HIM) into the center of the silicon-nitride membrane. Before usage, each chip was cleaned for 30 min in a 80°C hot piranha solution, consisting of freshly mixed aqueous  $\text{H}_2\text{O}_2$  solution and concentrated  $\text{H}_2\text{SO}_4$  with a ratio of 1:3 (v/v). This treatment ensures a high hydrophilicity of the membrane, which is important for surface fusion of SUVs. Afterward, the chip was carefully rinsed with deionized water and mounted into the sample chamber.

### Lipid bilayer-coating

Coating of the NP walls with a lipid bilayer from the SUVs was performed similar to the work of Yusko et al.<sup>[51]</sup>. The SUVs were prepared by utilizing a rotary evaporator for formation of a lipid film in a round bottom glass flask<sup>[182]</sup>. After resuspending this film in buffer (150 mM KCl and 10 mM HEPES at pH 7.5) to a final lipid concentration of 2 mM, the SUVs were generated via tip sonication (10–20 min at 30 % power). The used lipid mixture was composed of 99.2 mol% POPC and 0.8 mol% Rhod-DOPE (DOPE labeled with Rhodamine B). The coating process of the silicon-nitride membrane and the NP walls with a lipid bilayer is illustrated in Figure 3.5. Initially, the sample chamber was rinsed with buffer (150 mM KCl and 10 mM HEPES at pH 7.5), followed by the exchange of the buffer in the *cis* channel with the SUV suspension (image I and II). The vesicle solution was left for 15 min in the channel to let the vesicles interact with the silicon-nitride membrane. Due to the hydrophilic membrane, the SUVs burst on the surface and merge to a lipid bilayer, which covers the membrane as well as the NP (image II and III). Excess SUVs were then removed by rinsing with MilliQ® water and both *cis* and *trans* reservoirs were filled with a solution of 2 M KCl and 10 mM Tris/HCl at pH 8.0.

**FIGURE 3.5**

Schematic sketch illustrating the main preparation steps for coating a NP containing silicon nitride chip via SUV fusion.



As indicated in image IV in Figure 3.5 the lipid bilayer did not only cover the lower side of the silicon-nitride membrane and the NP wall, but also the upper side of the membrane. Thus, a large patch with a typical size between 5 and 20  $\mu\text{m}$  was formed, which was clearly observable by fluorescence microscopy. To confirm if a bilayer coating attempt succeeded, *fluorescence recovery after photo bleaching* (FRAP) was

used, as well as the NP conductivity measurements. As evidence of a reduced NP diameter due to the lipid-coated pore walls, the conductivity was perceptibly reduced compared to an uncoated NP<sup>[51,182]</sup>. Once a NP was coated, the entire sample chamber was rinsed again with buffer (20 mM KCL and 2 mM Tris/HCL at pH 8). Then, a suspension of bead-dsDNA constructs was added to the *cis* compartment and dsDNA threading and force measurements were performed.

### **Preparation of bead-dsDNA constructs**

To conduct a controlled translocation via optical tweezers, the dsDNA has to be coupled to a microsphere. For this purpose, microbeads made of polystyrene and coated with streptavidin were used. The size distribution of the beads ranged from 3.05 to 3.28  $\mu\text{m}$  in diameter<sup>[130]</sup>. For accurate immobilization of the DNA molecules onto the bead surface,  $\lambda$ -DNA was tagged on one end with a biotin molecule: 20  $\mu\text{l}$   $\lambda$ -DNA (500  $\text{ng}/\mu\text{l}$ ) and 2  $\mu\text{l}$  oligos (5'-AGGTCGCCGCC-3', 432  $\text{ng}/\mu\text{l}$ ) were together heated up to 75°C to break up the circular  $\lambda$ -DNA-structure, resulting in an open double-strand with a 12 base long overhang at each side (sticky ends). The following slow cooling (from 75°C to 25°C over 80 *min*) induced a saturated attachment of oligos to the complementary base sequence at one sticky end. Then, 0.6  $\mu\text{l}$  oligos (5'-GGG-CGGCGACCT-3', 543  $\text{ng}/\mu\text{l}$ ), labeled with a biotin molecule, were hybridized to the other end of the  $\lambda$ -DNA. This occurred during slow cooling from 40°C to 25°C over 60 *min*. For purification, the complete suspension was filtered and washed with buffer solution (150 mM NaCl, 10 mM Tris/HCl, pH-Wert 8) in several centrifugation steps (5000 *g* for 7 *min*, respectively). Afterwards, the filtered DNA was diluted with 180  $\mu\text{l}$  of the same buffer solution, yielding a final DNA concentration of 50  $\text{ng}/\mu\text{l}$ . This DNA suspension was stored in small aliquots in a freezer at -20°C.

The immobilization of the DNA molecules onto the streptavidin coated microbead surface was only performed immediate prior to experimental usage. At first, 0.5  $\mu\text{l}$  of the microbead stock solution and 18  $\mu\text{l}$  buffer (20 mM KCL and 2 mM Tris/HCL at pH 8) were mixed and gently vortexed for several seconds. Then, 1  $\mu\text{l}$  of the final DNA solution was added and this suspension was also gently vortexed for several seconds. After 10 *min*, the microbead-dsDNA construct solution was amended with 20 mM KCL buffer to a final volume of about 1 *ml*.

### **3.3.2 Langmuir-Blodgett Transfer**

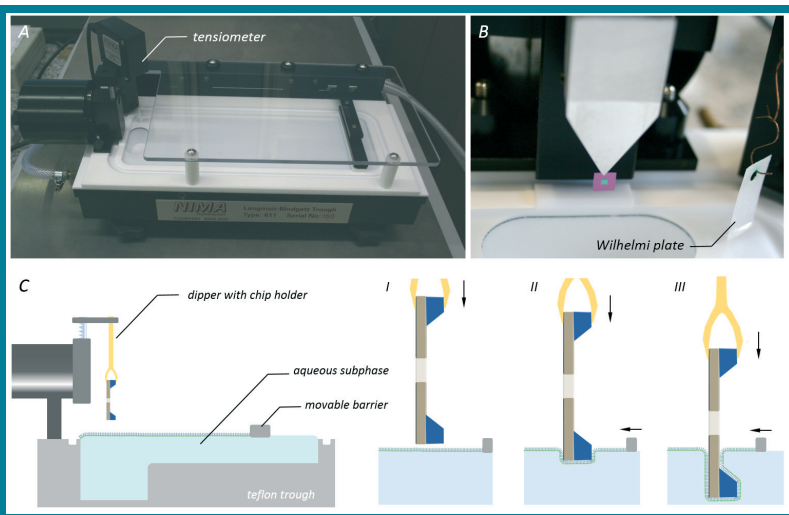
As described in chapter 2.2, the Langmuir-Blodgett (LB) transfer technique allows for generating densely packed lipid monolayers and transferring these layers onto solid substrates. A PTFE (*polytetrafluoroethylene*, teflon) trough in combination with a movable barrier (PTFE) for enclosing a distinct surface area, serves as basic platform of this technique. A photograph (A) and a schematic (C) of the setup are shown in Figure 3.6. To measure the lateral surface pressure, a tensiometer (A) in combination with a Wilhelmy-plate was used (B). A monolayer can be transferred by utilizing a dipper (with integrated chip holder), which can be precisely moved in vertical direction (Figure 3.6 D and I - III).

Prior to each experiment the trough was cleaned and the tensiometer calibrated. Once the trough was filled with the subphase (MiliQ®-water or 1 mM ZnCl<sub>2</sub>) in such a

manner that the barrier visibly touched the liquid surface, the cleanliness of the subphase was checked by closing the barrier (reducing the enclosed liquid area). Any pressure increase was due to contaminants on the subphase surface and had to be removed via a PTFE nozzle connected to a suction pump. Once the subphase was clean, a small amount of lipids (5–30  $\mu\text{l}$ , dissolved in chloroform) was spread drop wise into the active part of the trough (left side in image C).

**FIGURE 3.6**

Two photographs showing the Langmuir-Blodgett trough with installed tensiometer (A) and the holder with mounted silicon nitride chip (B). Image C illustrates the working principle of LB trough. Additionally, the lipid monolayer transfer process is pictured (I to III).



### ***Isotherm measurement***

The surface tension (inverse of the surface pressure) can be described as the work required to expand the surface isothermally by unit area<sup>[109]</sup>. The tendency of surface-active molecules, like phospholipids, to accumulate at interfaces favors expansion of the interface and hence lowers the surface tension. This behavior enables the monitoring of the surface pressure as a function of area<sup>[109]</sup>. An isotherm was recorded following lipid spreading and 10 *min* allowance for solvent evaporation. This was done by sweeping the barrier over the water surface (speed: 10–40  $\text{cm}^2/\text{min}$ ), and thus forcing the lipid molecules to come closer together and finally forming a compressed, ordered monolayer. Once the collapse pressure was reached (compare to 2.2), the film irretrievably lost its monolayer form and it was possible to determine the area occupied per single molecule. Measuring an isotherm prior to each LB transfer experiment is important to ensure that the lipid molecules are not damaged and especially to decide at which constant surface pressure the transfer should be executed. Herein, the transfer pressure was set to be a maximum of 80 % of the collapse pressure.

### ***Lipid monolayer transfer***

After determining the optimal transfer pressure, the trough was cleaned by means of the suction pump and lipid solution was spread in the subphase surface. This time the barrier was not moved at a constant velocity, but instead, was directed to move to keep a defined pressure (e.g. 37  $\text{mN/m}$ ) constant. Once a stable pressure was recorded, the dipper (with holder for the microchip) was slowly lowered, thus dipping into

the subphase-monolayer interface. At this moment the LB film started to be transferred to the microchip surface; this process is schematically illustrated in Figure 3.6 I - III. Over the course of the transfer, the number of lipids available on the subphase surface decreased. To ensure that the selected pressure was constant, the barrier closed slowly (automatically controlled by the software). The transfer ratio was determined by measuring the area of monolayer removed from the subphase surface and taking the area of the microchip (immersed in the subphase) into account. This value serves as a strong indicator as to, whether or not the microchip was completely covered with a LB film.

As described in 2.2 it is possible to coat both hydrophilic and hydrophobic surfaces. In this experiment, the chip was functionalized with silane (TDS) and thereby hydrophobic. This led to an attachment of the lipid tails to the chip surface and in the micropore, a lipid bilayer have been formed. The microchips used here consisted of silicon and a silicon nitride membrane, but differed in dimension as the chips presented 3.3.1. They had a size of  $5\text{ mm} \times 5\text{ mm}$  and a thickness of  $200\text{ }\mu\text{m}$ . The membrane window was  $2\text{ mm} \times 2\text{ mm}$  large and the membrane itself had a thickness of  $500\text{ nm}$  and contained a micropore with a diameter between  $3\text{ }\mu\text{m}$  and  $8\text{ }\mu\text{m}$ .

#### Assembly of coated microchip and sample chamber

Once the microchip was coated after dipping into the subphase, it was transferred to the sample chamber without making contact with the air. Prior to this, the sample chamber has to be prepared. The principle design and structure was the same as used for the SUV coating, but some dimensions were different. Due to the larger window area, the *cis* channel was  $2\text{ mm}$  wide and the PMMA part for sealing the *trans* compartment had a conical shape (see Figure 3.7 A - D).

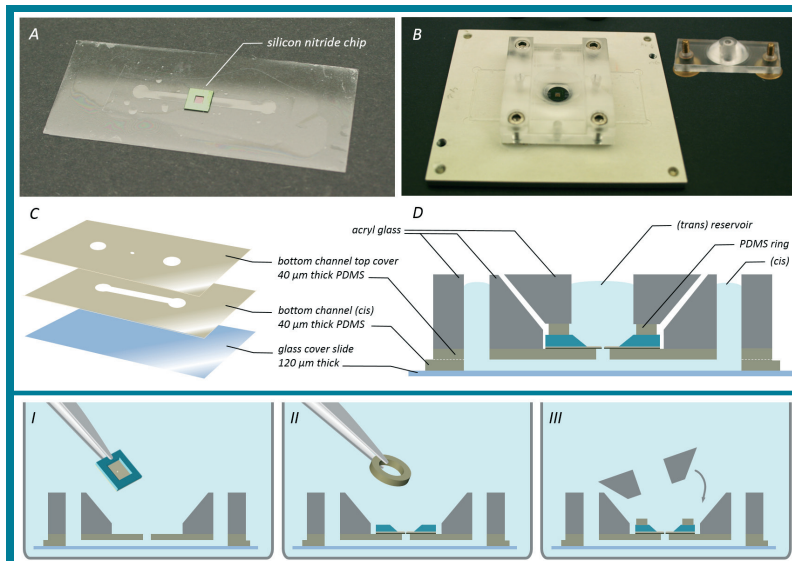


**FIGURE 3.7** Photographs presenting the channel structure (A) and partly assembled sample chamber (B). The detailed structure differs slightly from the one shown in Figure 3.4 (C and D), because of the bigger size of the silicon nitride chip. The final assembly was conducted completely underwater as pictured in images I to III.

This design enabled accurate microchip placement, because the remaining parts of the sample chamber were already assembled. Before immersion of this partly assembled sample chamber into a bigger container filled with MilliQ®-water, the *cis* channel

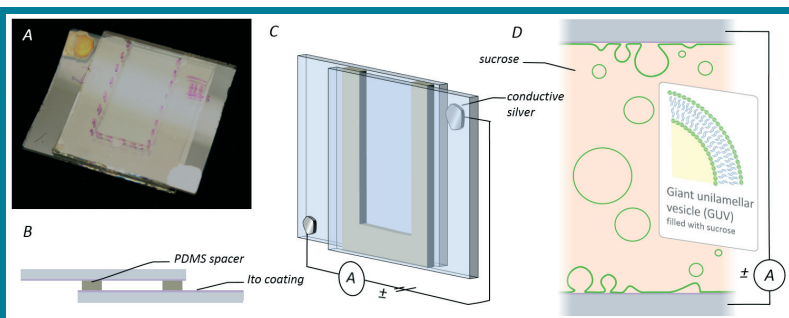
was also rinsed with water to ensure accurate filling without air bubbles. Once these initial preparations were accomplished and a LB film deposition completed, the microchip was transferred from the LB trough to the big container via a small container (see also image Figure 4.14 in chapter 4.2.1). The following underwater mounting procedure is illustrated in Figure 3.7 I – III. The microchip was placed on top of the middle access hole and sealed by the *trans* PMMA part with a PDMS ring in between. Then, the sample chamber was removed from the bigger container and gently wiped before exchanging the water with 20 mM KCL buffer in both compartments. Once the assembly was complete, the sample chamber can be investigated at the OT microscope. Additionally, the presence of an intact lipid bilayer membrane across the micropore can be checked by measuring the resistance. For biopore incorporation fresh prepared  $\alpha$ -hemolysin could be added (with different concentrations ranging from 2 ng/ml up to 16  $\mu$ l/ml). OT translocation experiments were performed by using dsDNA-microbeads constructs, prepared as described above (3.3.1).

### 3.3.3 Giant Unilamellar Vesicles

For preparing giant unilamellar vesicles (GUVs), the electroformation technique was utilized. This technique (as described in 2.1.3) uses low-voltage electric fields, which promote the formation of truly unilamellar vesicles.

In this thesis ITO (indium tin oxide) coated glass coverslides with a size of about 2 cm x 2 cm, provided the basis for proper electroformation. After cleaning of two conductive glass plates via an ultrasonic bath (with acetone, ethanol and water), a small amount of lipid solution (5  $\mu$ m to 25  $\mu$ m, solved in chloroform) was spread dropwise over an area of about 0.5 cm<sup>2</sup>. This area was marked with dashed lines in image A of Figure 3.8. After drying (in a vacuum for at least 2 h), the two lipid coated coverslides were clamped against each other with a 1 mm thick PDMS spacer in between (see image B and C). In this configuration the ITO coated sides of the glass plates were facing each other and additionally, a small droplet of silver conductive paint was placed onto it for easier connection to a signal generator (image C).

**FIGURE 3.8**  
Photograph (A) and detailed structure (B and C) of the GUV generation chamber. The scheme (D) depicts the electroformation process by swelling.



The enclosed volume between the coverslides was filled with a 300 mM sucrose solution and then the chamber was vertically clamped in a holder. In first formation experiments a function generator was used for applying alternating voltages. Later on, a LabView program was used for voltage application<sup>1</sup>.

<sup>1</sup> This LabView software was coded by Dr. Lukas Bogunovic.

The detailed voltage protocol is as follows:

- Step 1: Increasing sinusoidal voltage from 0 V to 1.6 V RMS at 12 Hz in 0.1 V RMS steps (each with 60 sec).*
- Step 2: Constant sinusoidal voltage of 1.6 V RMS (at 12 Hz) for 1 to 3 h.*
- Step 3: Square wave voltage of 1.6 V at 5 Hz for 10 min.*

The last step promoted the final separation of a swelled lipid bilayer bubble, thus forming an individual GUV. This process is illustrated in image D of Figure 3.8, which also clarifies that the GUVs are filled with 300 mM sucrose solution. Because the molarity of the sucrose solution is important for appropriate sinking properties and influences the bursting on different surfaces, varying molarities were tested. These tests are presented in 4.2.2. After accurate vesicle formation, the suspension of GUVs in sucrose was removed from the chamber and transferred to a plastic vial and stored at 4°C for up to 5 d. Before using the GUVs for bursting events, the vial was gently vortexed. With this electroformation method a polydisperse suspension of GUVs was obtained with diameters ranging from a few up to 80  $\mu\text{m}$ .

#### **GUV sinking and bursting procedure**

The sample chamber structure used for GUV sinking and fusion studies, as well as the silicon nitride chip treatment, was identical to the one described above for the SUV coating experiments (compare chapter 3.3.1). Briefly, after filling the sample chamber with buffer and electrical connection, 2–5  $\mu\text{l}$  of the GUV suspension was added to the *trans* reservoir. The sinking and bursting process was observed with fluorescence microscopy and by measuring the ionic current, while a constant voltage was applied. Once a NP was covered by a lipid bilayer membrane (recording a distinct current drop), freshly prepared  $\alpha$ -hemolysin was added (with different concentrations ranging from 2 ng/ml up to 16  $\mu\text{l}/\text{ml}$ ).

For free translocation through the  $\alpha$ -hemolysin biopore, short single-stranded DNA fragments were used. These oligos consisted of 12 bases (5'-AGGTCGCCGCC-3') and were solved in 20 mM KCL buffer.

For controlled translocation by optical tweezers,  $\lambda$ -DNA-microbead constructs (see chapter 3.3.1) were used again, but the "free" end of the double stranded  $\lambda$ -DNA had, in this case, a single stranded overhang (poly(dT)<sub>130</sub>). This ssDNA component was envisioned for controlled entrance and translocation through the biopore constriction.

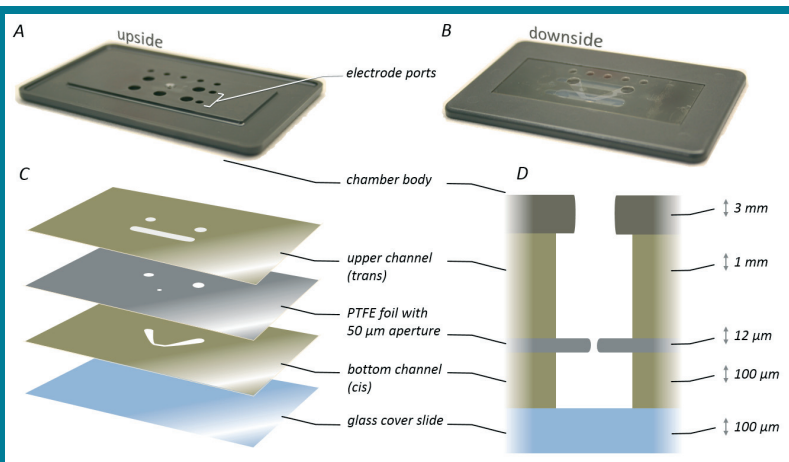
#### **3.3.4 Ionovation Bilayer Slide**

As an alternative way for lipid bilayer formation, the commercially available Bilayer Slide (Ionovation GmbH, Osnabrück, Germany) was utilized. This instrument allows to generate semi-automated horizontal bilayers<sup>[222]</sup> combining and reinterpreting the widely established painting<sup>[223]</sup> and Montal-Müller<sup>[224]</sup> technique. The main difference is that the bilayer is formed horizontally and not vertically. This modification enabled investigation of the bilayer formation process by OT microscopy. The design and structure of this Bilayer Slide is shown in Figure 3.9. The horizontal PTFE sheet was 12  $\mu\text{m}$  thick and had a 50  $\mu\text{m}$  diameter drilled hole, which exclusively connected the

*cis* and *trans* compartments. The sheet was sandwiched between a glass coverslide and a plastic body chamber using a double-sided adhesive film application. Both adhesive films contained a channel structure, which were fabricated by laser edging and with a complete volume of approximately 150  $\mu\text{l}$ .

**FIGURE 3.9**

Graphics showing the upside (A) and downside (B) of the Bilayer Slide. The subjacent sketches illustrate its structure and composition. The 12  $\mu\text{m}$  thin PTFE foil (containing the 50  $\mu\text{m}$  aperture) is sandwiched between a coverslide and the chamber body by using double-sided adhesive film. This films feature laser edged channel structures.



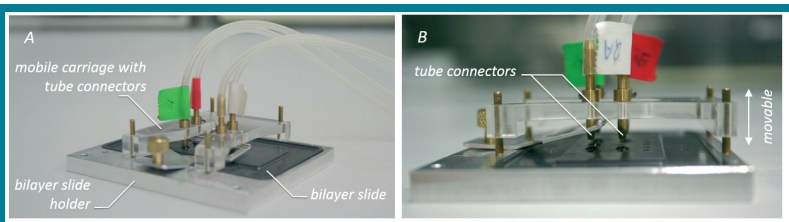
The body chamber had five main ports. Three (first row in image A) of these ports belonged to the upper channel, whereas the outer ports were for liquid perfusion and the middle port was for lipid injection. The latter also preserved the possibility to perform transmitting light microscopy. Two additional main openings were for perfusion of the bottom channel, and two minor openings on the right side were for an electrical connection (see label in image A). The glass cover slide was transparent and the distance between it and the PTFE sheet was 100  $\mu\text{m}$ , thus within the working distance of a high-numerical-aperture objective.

#### Setup integration of the Bilayer Slide

Because the Bilayer Slide is commonly utilized in combination with additional experimental setups (Ionovation Bilayer Explorer, including a detection unit and a control unit), a holder for the Bilayer Slide and a mobile carriage with tube connectors was homebuilt. The photographs in Figure 3.10 show the chip holder and the carriage, which carries four tube connectors. The microtubes lead to the syringe-pumping unit.

**FIGURE 3.10**

Photographs showing the Bilayer Slide holder (A) and the carriage with tube connectors. The carriage was adjustable in distance of the Bilayer Slide (B).



Additionally, it was feasible to vertically move the carriage manually up and down (image B). This feature was determined to be important while measuring the ionic current. The current recording possess much less noise after the tube connectors were not attached to the buffer meniscus of a main opening. For mounting the

Bilayer Slide holder onto the XY-stage of the microscope, an adapter was fabricated, which is visible in Figure 3.11 A. The electrodes (chlorinated platin wires) were connected to the patch-clamp amplifier via the headstage. In lastly executed experiments, the electrodes are also connected to a LCR-meter (HAMEG) for capacitance measurements.

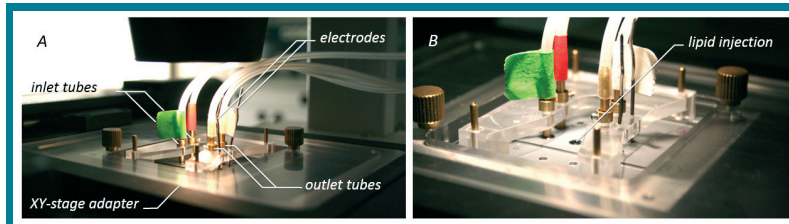


**FIGURE 3.11**

Photographs showing the completely mounted Bilayer Slide on the microscope stage with connected inlet and outlet tubes and electrodes.

Before starting an experiment, the Bilayer Slide was filled with measuring buffer and optically (or electrically) controlled for the absence of microbubbles of air. After proper mounting, both channels *cis* and *trans* were flushed via the syringe unit. The microtubes had also be free of trapped air. Next, a volume of  $0.2 \mu\text{l}$  of lipid solution was painted near the aperture (image B) and perfusion cycles for lipid bilayer generation were started. More details regarding the specific perfusion parameters are presented in chapter 4.2.3.

For biopore incorporation and microbead preparation the same procedures were utilized as described in the previous chapters.

The glass syringes, as well as the microtubes and the Bilayer Slide, were cleaned before and after each measurement session with, MiliQ®-water, isopropanol and dried under a nitrogen stream.

## 4 Results and Discussion

The scope of this work is the establishment of experimental methods for modifying solid-state nanopores (NPs) with lipid bilayer membranes. The ability to execute OT force measurements should be respected. In this context two major projects are presented; both projects are based on the utilization of lipid bilayer membranes. In chapter 4.1 lipid bilayer membranes were used to generate a stable coating covering the sidewalls of a NP and the adjacent silicon nitride membrane surface. Such surface modification offers new prospects and insights for optical tweezers controlled DNA threading experiments. In chapter 4.2 three different ways of producing freestanding lipid bilayer membranes sealing a silicon nitride nanopore are examined and demonstrated. This bilayer provides a biological environment that enables the incorporation of the pore forming toxin  $\alpha$ -hemolysin. These well-characterized biopores can be utilized for free translocation of ssDNA, as well as for OT controlled ssDNA-threading studies.

### 4.1 Lipid Bilayer-Coated Nanopores

To get a better understanding of the interaction between threading forces of single DNA strands and nanopores, which are embedded in membrane systems, it is important not just to alter the pore size (the membrane thickness or membrane material, respectively), but also to diversify the surface functionality of used membrane material. The most common membrane material is silicon nitride. When using these substrates it was frequently observed that surface charges, impurities or DNA adhesion to the substrates can negatively influence the experiments.

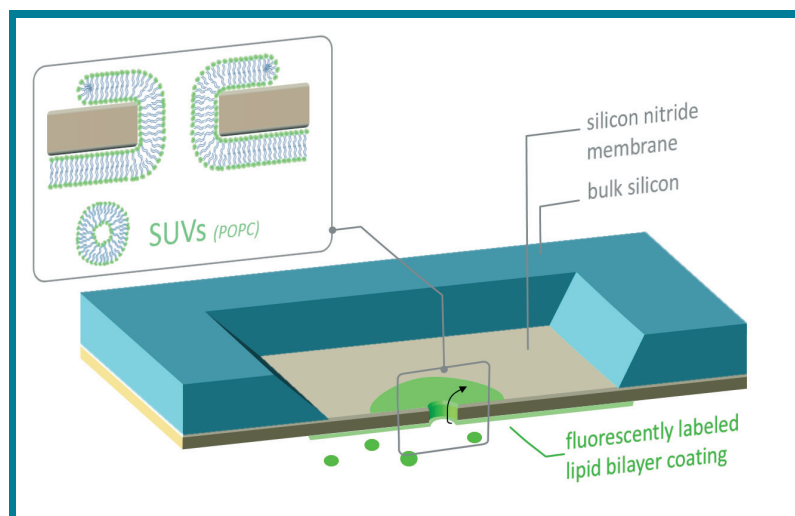


**FIGURE 4.1** Schematic sketch of a silicon nitride chip after treatment with small unilamellar vesicles. The magnification shows a vertical cross section through a NP with the lipid bilayer-coating.

The specific work on variations to functionalize the surface should provide an essential tool for the researcher to improve and to systematically control the DNA nanopore translocation process. One possible variation is demonstrated in this thesis by using

a lipid bilayer, which acted as a coating for the silicon nitride membrane (and with this also for the inner part of the NP region). This simple and elegant approach is schematically illustrated in Figure 4.1, showing a NP containing silicon nitride chip with lipid bilayer coating. The coating was conducted by utilizing small unilamellar vesicles (SUVs) and previously treating the silicon nitride chip with piranha solution, providing the necessary hydrophilicity of the membrane surface. Because of the small diameter (below 50 nm) and the resulting high surface tension, the SUVs burst on the strong hydrophilic surface of the silicon nitride membrane and merged into an intact lipid bilayer (the whole procedure is detailed described in chapter 3.3.1). The hydrophilic head groups of the phospholipids of one monolayer were oriented towards the silicon nitride surface, whereas the second monolayer was oriented in the opposite direction, and thus shielded the hydrophobic chains from the surrounding water. Of note is that a very thin water layer remained between the bilayer and the silicon nitride membrane<sup>[51]</sup>.

Another advantageous aspect of the small sized vesicles was the ability to easily become incorporated into an already existing lipid bilayer. This behavior was the reason, why the lipid bilayer could expand and slip through the nanometre sized pore (as indicated by the black arrow in Figure 4.1). The next section will address the procedure to detect and confirm the presence of a successfully completed lipid bilayer-coating.

#### 4.1.1 Characterization of Coated Nanopores

The characterization of the lipid bilayer-coated nanopores is a very crucial step, because one has to confirm that the SUVs not only burst and merge into a bilayer on the bottom side of the silicon nitride membrane, but also slip through the NP and cover the NP walls. Only the complete coating of the NP walls and the surrounding region of the membrane resulted in surface functionalization alteration, thus changing the DNA translocation properties. Due to the small size of the NP, the verification of accurate coating properties could only be executed by experimental methods in indirect manner.

For this reason, the lipid mixture was composed of POPC and Rhod-DOPE, so that the lipid bilayer could be observed by fluorescence microscopy. As described in section 3.3.1, the SUVs were added through the bottom channel of the sample chamber, and thus the vesicles could only attach (followed by bursting and merging) to the bottom side of the silicon nitride membrane. It was impossible for the SUVs to flow through the nanopore because their diameter was above the diameter of the NPs. The only way for the lipids to reach this upper region of the membrane was to move as part of an expanding lipid bilayer through the NP, followed by growing on the upper region in form of a roundly shaped patch (see Figure 4.1). This behavior was monitored by comparing fluorescence images before and after the coating process. Two examples of fluorescent microscopy images of successfully coated silicon nitride chips are shown in Figure 4.2. The bright square (area *II*) represents the "window area" of the silicon nitride membrane and the even brighter round shaped patch corresponds to the lipid bilayer that moved through the pore (area *I*). The intensity of the bilayer patch was higher because of the double amount of fluorescently labeled lipids in this

region (see schematic sketch in Figure 4.2). However, the intensity of the window area (except the patch) was brighter than the coated surrounding silicon-nitride membrane (area *III*) because of some light reflections from above the Chip, which were blocked by the bulk silicon material. The size and specific shape of the lipid bilayer patch depended on the SUV concentration, as well as the interaction time (usually 15 *min*).

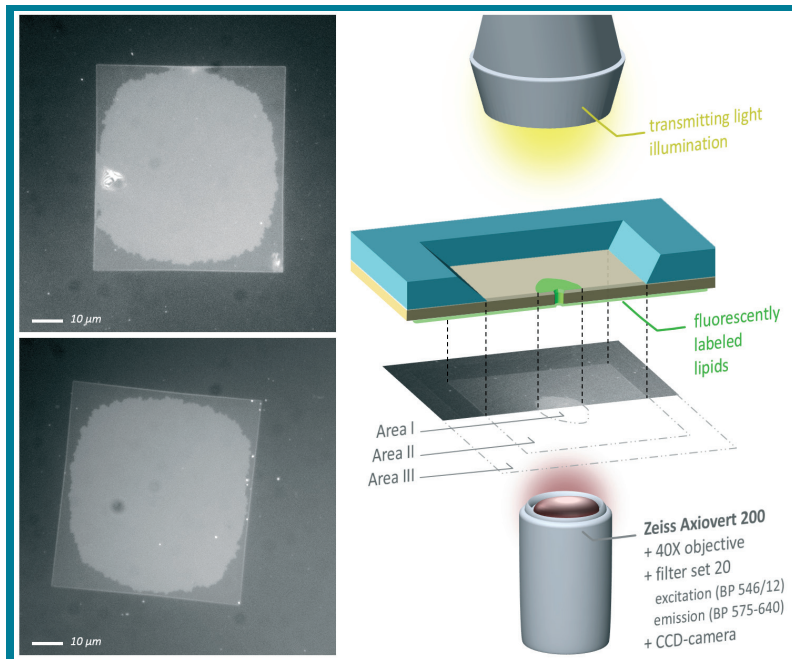


**FIGURE 4.2**

Left: Fluorescence microscopy images of two successfully coated chips. The bright square represents the “window area” of the silicon nitride membrane and the even brighter round shaped patch corresponds to the lipid bilayer, which slipped through the pore.

Right: schematic sketch of the experimental setup clarifying the observation of three areas (*I*, *II* and *III*) with different fluorescence intensities.

[Parameters: buffer: 20 mM KCL and 2 mM Tris/HCL at pH 8; exposure time: 100 msec]

The upper image in Figure 4.2 is the only one where the patch seemed to be in contact with the “window walls”. The commonly discovered patch was round shaped and had a diameter of about 15  $\mu\text{m}$  (comparable with the image marked with 180 sec in Figure 4.3). Additionally, during the coating and bilayer slipping process, a transmembrane voltage was never applied. In the event of a successful coating (i.e. a lipid bilayer patch was visible), a voltage of 100 *mV* was applied and used to determine, whether the coating was intact within the NP region (specifically, the NP walls). This procedure will be discussed later in this section.

### High voltage dependency

First, it is intended to present another visual observable phenomenon in context with applied high<sup>1</sup> voltages, which is depicted in Figure 4.3. An accurate lipid bilayer coating attempt resulted in an area of the patch either expanding or shrinking with time when a constant high (positive or negative) transmembrane voltage on the order of 2 *V* was applied.

The upper part of Figure 4.3 illustrates the expansion while applying a high positive voltage. As the red arrows in the sketch indicate, the bilayer migrated from the

<sup>1</sup> “High” voltages refer here, in the context of nanometer sized pores, to voltages of 1 – 3 Volts and have to be compared to “normal” voltages of 50 – 100 *mV* (as usual for this kind of experiments).

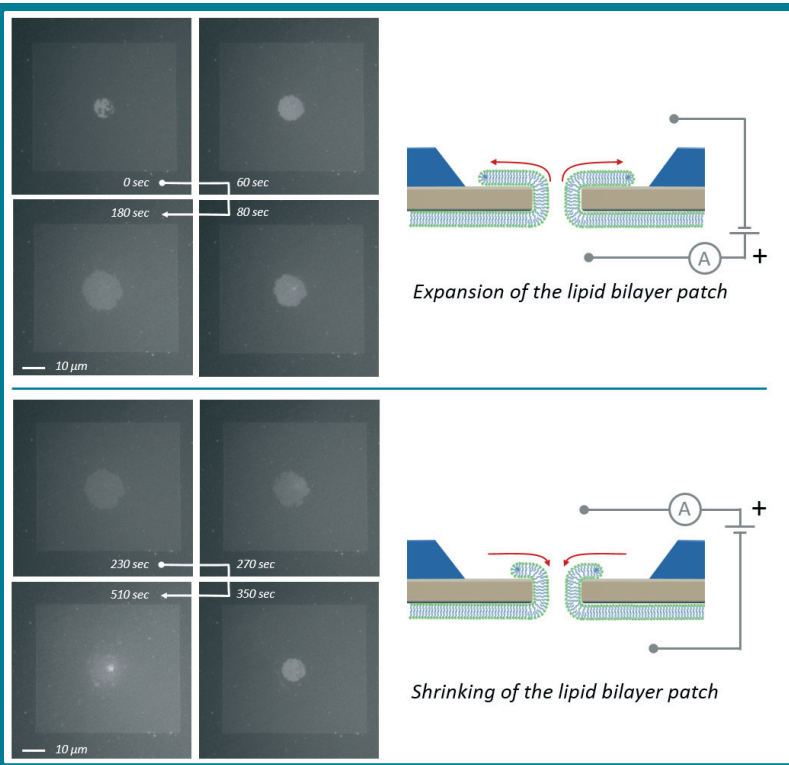
bottom side through the NP and enlarged the patch area on the upper side. Four fluorescence images at different points of time are shown. The bilayer movement also returns back in direction after inverting the voltage. This observation is important for two reasons: On the one hand, the bilayer was at high voltages fluid, and thus not immobile. This behavior suggests that the lipid bilayer had a positive charge, but due to the fact that the lipids are zwitterionic (exhibiting an overall electric neutral charge) the movement was most likely mainly caused by the electro osmotic flow. The EOF was directed to the negative electrode (see section 2.6), and thus pulled the bilayer along.

**FIGURE 4.3**

Left: Series of fluorescence microscopy images showing the expansion and shrinking of a lipid bilayer patch through the nanopore, while a high (positive or negative) voltage in the range of some *Volts* was applied. The denoted time refers to the first image.

Right: Schematic sketch of the lipid bilayer patch size variation.

[Parameters: buffer: 20 mM KCL and 2 mM Tris/HCL at pH 8; exposure time: 200 ms]



On the other hand, this effect only occurred at 2 V voltages and can be neglected for measurements applying 20–100 mV. Herein, we never observed such movements at “normal experimental conditions”, which means that the bilayer could be characterized here as immobile<sup>[182]</sup>. However, the movement of the whole bilayer and the movement of single lipids within a stated bilayer area (the position and border of the patch do not change) must be differentiated. The bilayer itself should remain fluid in context of the fluidity of single phospholipids.

#### **Fluidity and lateral diffusion of single lipids**

In order to confirm this fluidity and to determine lateral diffusion constants of the lipids, fluorescence after photobleaching (FRAP) experiments were performed on the bilayer at a region near the freestanding silicon nitride membrane. The labeled

phospholipids were selectively photobleached using an aperture (image A in Figure 4.4) for 30 *min* during constant excitation by illumination<sup>1</sup>. After this period of time, one can clearly identify the dark bleached spot in image B. After additional 15 *min*, a considerable recovery of the fluorescence in this spot was observable. To compare two FRAP experiments with different phospholipids (POPC and DPPC), the intensity of the bleached area was monitored for several time points while the bleached labeled lipids diffused out and unbleached lipids diffused in. The diagram in Figure 4.4 shows a plot of intensity versus time for each run. Even though the intensity did not completely return to the initial normalized intensity of 1 for both runs, the qualitative difference in recovery time between POPC and DPPC was visible.

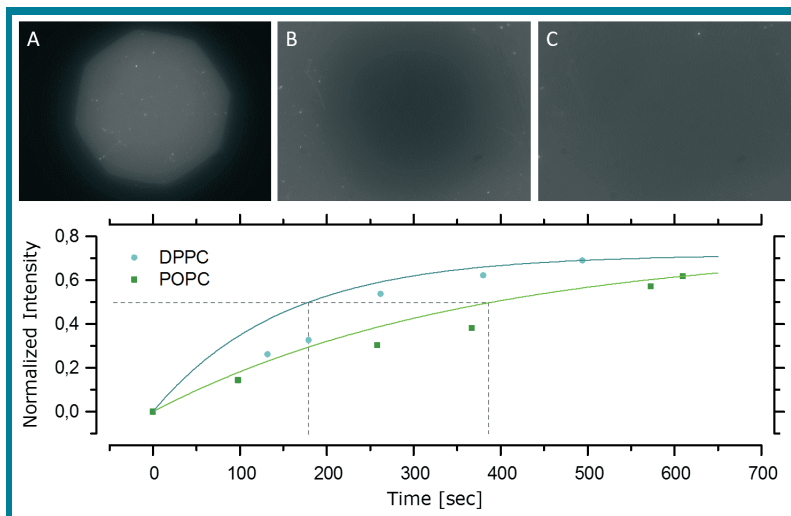


**FIGURE 4.4**

The upper series of fluorescence microscopy images (A, B and C) illustrate the executed FRAP measurement.

The bottom diagram shows a plot of intensity versus time obtained from two different FRAP experiments. The larger  $t_{1/2}$  value and slower recovery of POPC bilayers indicate the increased viscosity in comparison with DPPC bilayers.

[Parameters: radius  $r$  of the bleached spot: 20  $\mu\text{m}$ ; time distance between image B and C 630 sec; POPC  $t_{1/2} = 390$  sec; DPPC  $t_{1/2} = 180$  sec]

The equation  $D_L (nm^2/\mu\text{sec}) = 0.224 \times r^2 / t_{1/2}$  (where  $r$  ( $nm^2$ ) is the radius of the bleached spot and  $t_{1/2}$  ( $\mu\text{sec}$ ) is the half time of the fluorescence recovery), was used to determine the diffusion coefficients<sup>[225,226]</sup>. The value of  $t_{1/2}$  is obtained from an exponential fit through the data. This diffusion coefficient for the bilayer containing POPC lipids is  $D_{L(POPC)} = 1.25 nm^2/\mu\text{sec}$  and for the DPPC lipids  $D_{L(DPPC)} = 2.45 nm^2/\mu\text{sec}$ , respectively. These results are close to reported values from the literature for diffusion constants of supported lipid bilayers, ranging from 2  $nm^2/\mu\text{sec}$  to 5  $nm^2/\mu\text{sec}$  (typically obtained on  $\text{SiO}_2$  or glass surfaces)<sup>[51,227,228]</sup>. The slower recovery of POPC bilayers indicated the increased viscosity in comparison with DPPC bilayers<sup>[51]</sup> and thus POPC is the preferable phospholipid for bilayer coatings.

#### **Indirect estimation of the effective NP diameter**

To verify if the coating within the NP was still intact and to answer the question, "how big the reduction of the NP diameter after coating is" (in comparison with the NP diameter before), we used the ionic current through the NP while applying a constant voltage of 100 *mV*. This procedure is performed for every measurement before and after the coating attempt. The effective diameter of this pore should be reduced in a range of 9.6 *nm*  $\pm$  0.2 *nm* to produce an ideal lipid bilayer coating of a silicon nitride

<sup>1</sup> The FRAP experiment was performed during a visit in the Biomembrane Lab of Prof. Michael Mayer at the University of Michigan and supervised by Dr. Eric C. Yusko.

pore<sup>[51]</sup>. In this context, the effective diameter of a NP refers to a cylindrical channel, which is broad enough for the buffer ions to pass through. The effective reduction of the NP diameter was composed of the thickness of the bilayer and the thickness of the interstitial water layer between the lipid bilayer and the silicon nitride wall of the pore. Yusko et al. presented<sup>[51]</sup> a calculated value of 1.1 nm for modelling the water layer (compared with literature data of 0.5 nm to 1.7 nm)<sup>[229,230]</sup>, and thus a value of 3.7 nm for the bilayer thickness (using POPC phospholipids) can be assumed<sup>[231]</sup>.

As introduced, the effective diameter of a NP diameter depends on the electrical resistance and thus on the ionic current. This value can be calculated (all other required experimental parameters are known and reproducible). Based on the fact that a silicon nitride membrane acts as an isolator, the electric potential drops down just within the NP region with a constant voltage application. The total resistance  $R$  of the system is as followed:

$$R = R_{NP} + R_A$$

In the experiment,  $R$  can be obtained by applying a defined voltage and measuring the associated ionic current.  $R_{NP}$  represents the resistance of the cylindrical NP volume and  $R_A$  corresponds to the access resistance of the NP. The latter is due to the effect that the electrical field on both sides of the pore emerge beyond the NP volume (each in form of a hemisphere<sup>[130]</sup>). The result of this is:

$$R = \frac{\rho_{SP} l_{NP}}{\pi r_{NP}^2} + \frac{\rho_{SP}}{2r_{NP}}$$

where  $r$  represents the radius of the nanopore,  $l_{NP}$  the length of the pore (i.e. the thickness of the silicon nitride membrane) and  $\rho_{SP}$  the specific resistivity of the electrolyte. Rearranging the equation to  $r_{NP}$  yields:

$$r_{NP} = \frac{\rho_{SP}}{4U} \cdot I \sqrt{\frac{\rho_{SP}^2}{16U^2} \cdot I^2 + \frac{\rho_{SP} l_{NP}}{\pi U} \cdot I}$$

The ionic current at an applied voltage of 100 mV is recorded and conducted using a sample chamber filled with a high concentrated electrolyte solution of 2 M KCL and 2 mM Tris/HCL (at pH 8), which has a specific resistivity of  $\rho_{SP} = 0.0467 \Omega m$ . This high concentration is necessary because, at low concentrations, existing surface charges would eventually dominate the conductivity of the NP<sup>[130]</sup>. Given the knowledge about the lipid bilayer and water layer thickness and following these methods, it is feasible to calculate the effective NP diameter for both lipid bilayer coated and uncoated silicon nitride NPs. In case of the coated NPs it is important to consider not only the reduced diameter, but also the increased thickness of the membrane (silicon nitride membrane plus lipid bilayer membrane, see Figure 4.1).

In Figure 4.5 the data of 38 independent coating attempts are illustrated by comparing the NP-diameter before and after the SUV treatment. The green line represents the theoretical expected values for the NP-diameter with a successful coating and the gray dashed line shows the expected values under no variation of the NP-diameter. The proximity between a data point and the green line describes the success of the coating process, including the reduction of the diameter by the expected value of 9.6 nm. The inset in Figure 4.5 shows the distribution of the NP-diameter reduction in subdivisions of 2 nm width. For six experiments no significant reduction occurred,

whereas 13 experiments exhibited a successful reduction in the range of 7.6 nm to 11.6 nm. Interestingly, the most measured reductions were smaller than the expected value. This behavior indicates that the probability for an incompletely lipid bilayer coating is higher than for the formation of multiple lipid bilayer sheets.

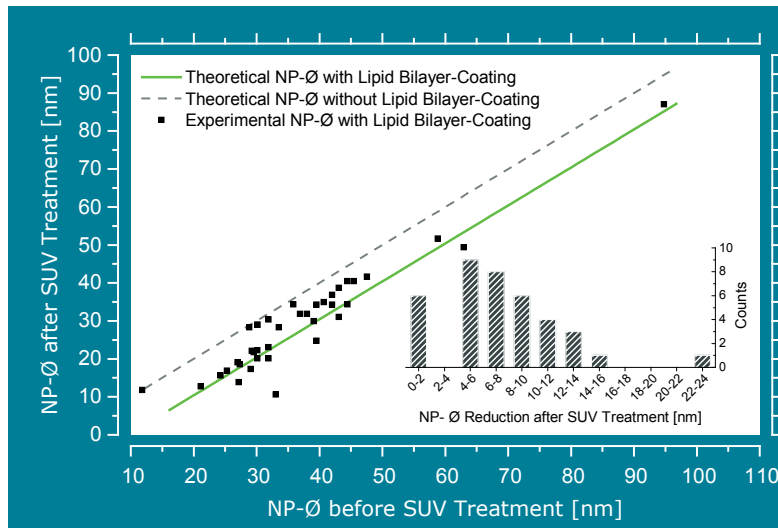


**FIGURE 4.5** Diagram which visualizes the success and failure of a lipid bilayer-coating process. The NP-diameter before coating is plotted against the diameter after coating for 38 independent experiments. The green line represents the theoretically perfect NP-diameter with a complete lipid bilayer-coating and the grey dashed line the NP-Ø without any coating. The inset histogram shows the distribution of all measurements classified by their reduction in NP-diameter.

[Parameters: NP-Ø calculations with current values obtained at 100 mV and with 2M KCL and 2 mM Tris/HCL at pH 8]

In summary, one third of all coating attempts resulted in successfully surface modified silicon nitride membranes, which are suitable to be used for OT controlled DNA threading experiments.

**Alternative size determination by imaging**

Utilization of the ionic current for monitoring and determining of the pore size – in contrast to other methods like *Atomic Force Microscopy* (AFM) or *Helium-Ion Microscopy* (HIM) – was much faster and less invasive to the silicon nitride membrane and the NP. Nevertheless, it was important to verify the apparent size based on these imaging techniques. This additional information can be used to adjust and calibrate the NP drilling process itself. In cooperation with Dr. André Spiering and Dipl.Ing. Christoph Pelargus the process of drilling the NPs into solid-state membranes was characterized and optimized.

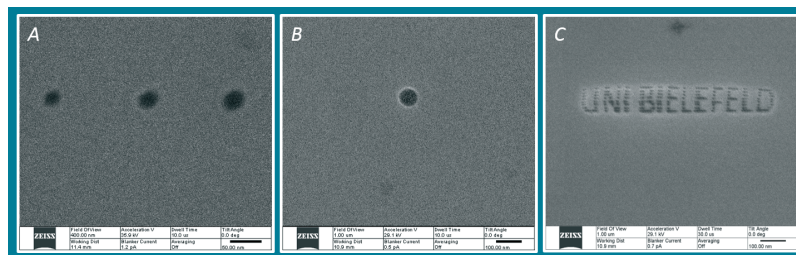


**FIGURE 4.6** Helium ion microscopy images of drilled nanopores and an exemplary lettering. The NP in the middle has an approximate diameter of 60 nm.

Figure 4.6 shows three examples of drilled NPs imaged with HIM. In image A, three drilled pores with different diameters are clearly visible, whereas the NP in image B has an approximated diameter of 60 nm. Image C illustrates a writing, demonstrating the accuracy and possibilities of the drilling process by HIM. Imaging of each drilled

pore by HIM was not advantageous and feasible, due to invasive manipulation of the silicon nitride material. The high energy required for a sufficient contrast during imaging can cause uncontrolled swelling of such thin silicon-nitride membranes or shrinking and clogging of the drilled NP. Additionally, some imaging experiments revealed trace amounts of unknown material (possibly carbons or residual of the silicon nitride membrane within the vacuum chamber) deposited in the neighboring region of the NP, by which further experiments with these NPs were no longer feasible<sup>[130]</sup>. However, it was possible to get a first approximation of the NP size, since it was directly linked to exposure time of the ion beam (maintaining other beam properties like focus or intensity constant).

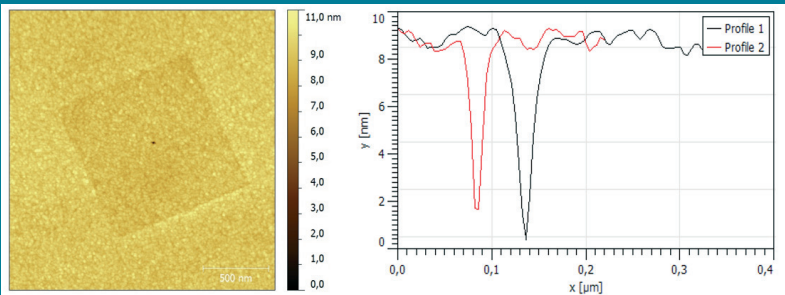
In contrast to HIM, the second characterization method using AFM was much less invasive, but very time-consuming. Hence, this technique was only used to verify the obtained NP sizes by HIM (in dependence of the exposure time) and by the ionic current calculations. In Figure 4.7 a typical AFM scan with corresponding height profile is presented.

**FIGURE 4.7**

Atomic force microscopy measurement of a NP drilled (and also imaged before) by HIM.

Left: AFM scan of the silicon nitride membrane, the dark spot corresponds to the NP.

Right: Height profile line scan. (Image shown with courtesy of Dr. André Spiering<sup>[130]</sup>).

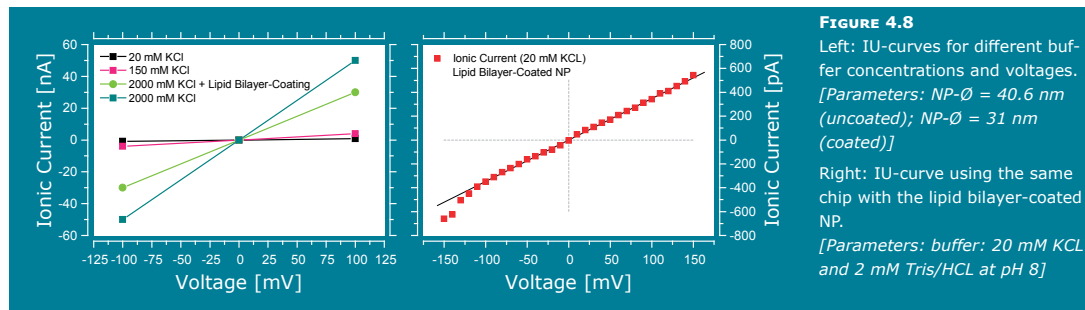


The NP can be clearly identified by the dark spot in the middle of the scan, whereas the circumjacent square clearly illustrates the HIM imaging process by leaving this area  $0.3 - 1 \text{ nm}$  thinner than before. The whole scan was performed on the freestanding silicon nitride membrane. Based on a height profile plot, this particular NP exhibits an elliptical form and a size of approximately  $20 \times 30 \text{ nm}$ .

#### **Ionic current to voltage characteristics**

In summary, the most effective and efficient way to determine the NP diameter was the indirect method via measuring the ionic current in combination with previous performed calibration experiments by AFM and HIM. Despite determining the NP size, it was also important to characterize the electric behavior of the sample chamber with integrated NP chips by using different electrolyte concentrations and applying transmembrane voltages in the range from  $-150 \text{ mV}$  to  $+150 \text{ mV}$ . Varying the electrolyte concentration was necessary due to the coating process by SUVs (as described in 3.3.1). In the left diagram in Figure 4.8, the decreasing current after the lipid bilayer coating is visible. The current was reduced from  $50 \text{ nA}$  (uncoated NP) to  $30 \text{ nA}$  (coated NP), measured under the same experimental conditions (applied voltage  $100 \text{ mV}$  and buffer concentration  $2 \text{ M KCL}$ ). After checking if the reduction in ionic current matched to the expected reduction in NP diameter, the electrolyte was exchanged with  $20 \text{ mM KCL}$  solution. The characteristic current-voltage curve at this low ionic

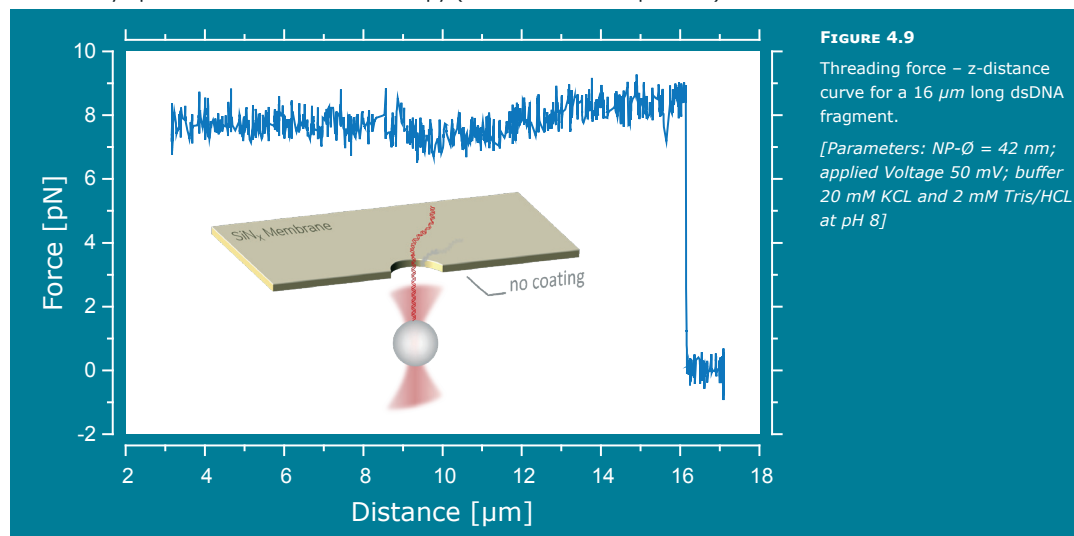
concentration is shown in Figure 4.8 on the right, exhibiting the expected linear behavior in the range from  $-100\text{ mV}$  to  $+100\text{ mV}$ . Some discrepancy can only be observed at higher negative voltages. This effect confirms the assumption that subsequent DNA-threading experiments should be conducted at lower voltages (usually  $50\text{ mV}$ ) in order to avoid variations or damage of the lipid bilayer coating.



This preliminary work (characterization of the NP-diameter and verification of the existence of a lipid bilayer coating) was the basis for performing DNA-threading experiments.

#### 4.1.2 DNA-Threading Experiments with Lipid-Coated Nanopores

For easier classification of the results gained by experiments with coated NPs, Figure 4.9 shows a typical threading force acting on a double stranded DNA, which was located within an uncoated NP with  $42\text{ nm}$  in diameter. The electrostatic force was detected by optical tweezers video microscopy (for Details see chapter 2.3).



During the increase of the vertical z-distance between microbead and nanopore at a constant applied voltage of  $50\text{ mV}$ , a constant force of  $8\text{ pN}$  was detected until the DNA strand was completely pulled out of the NP and the force dropped back to  $0\text{ pN}$ . The observable length of the DNA ( $16.1\text{ }\mu\text{m}$ ) as very close to the contour length of the

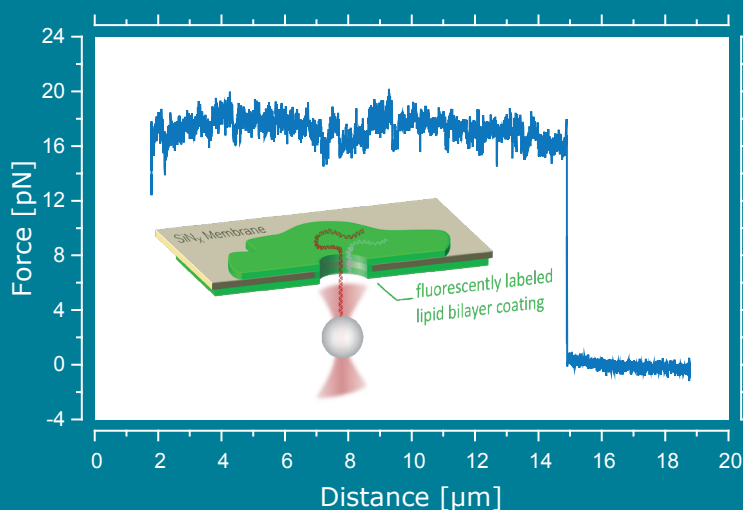
used  $\lambda$ -DNA ( $16.4 \mu\text{m}$ ). As such, it was possible to exclude varying hydrodynamic forces that acts on the microbead including the portion of dsDNA stretching between bead and nanopore. Furthermore, the DNA threading force did not fluctuate by more than 10 % while moving the microbead towards the NP up to a distance of  $2-3 \mu\text{m}$ . This indicated that the trapping laser had a negligible thermal influence on the threading force<sup>[182]</sup>. This DNA threading experiment was repeated several times for various applied voltages and different NP diameters (these results are shown at the end of this section). The voltage variations exhibited an approximately linear dependence of the measured force on the applied voltage over a range from  $20 \text{ mV}$  to  $100 \text{ mV}$ . The additional finding of considerably larger forces, observed for NPs with a diameter smaller than  $10 \text{ nm}$ , will also be discussed later.

In order to examine how an altered NP surface charge influences the threading force, a lipid bilayer coated nanopore (before coating: diameter of  $40.6 \text{ nm}$ ; after coating: diameter of  $31 \text{ nm}$ ) was used. The threading of a single dsDNA strand through this surface modified nanopore was feasible and the obtained translocation is shown in Figure 4.10. A DNA threading force of approximately  $16 \text{ pN}$  was measured and this value kept constant, on average, while pulling the complete DNA strand out again calculated contour length  $15.1 \mu\text{m}$ . This experiment was performed under the same salt and pH conditions and applied voltage as was used for the uncoated pores. The obtained force value was significantly higher than for comparable NPs without coating.

**FIGURE 4.10**

Measured dsDNA threading force induced by the electric field for a lipid bilayer-coated SiNX-membrane. Coating prepared by formation of SUVs. As the z-distance between bead and membrane was continuously increased, the force remained constant until it instantaneously dropped to zero when the DNA was completely pulled out of the pore. The Force of  $16 \text{ pN}$  is significantly higher than for an uncoated pore under equal conditions.

[Parameters: NP- $\emptyset = 40.6 \text{ nm}$  (uncoated); NP- $\emptyset = 31 \text{ nm}$  (with coating); applied Voltage:  $50 \text{ mV}$ ; buffer:  $20 \text{ mM KCL}$  and  $2 \text{ mM Tris/HCL}$  at pH 8]



The reduction of the pore diameter due to the coating ( $9.6 \text{ nm}$  for POPC bilayers) can only partially account for the strong increase in force. The diameter reduction resulted in a NP diameter of about  $31 \text{ nm}$  and such a variation in NP size would usually only account for a slight rise in measured threading force. This leads to the conclusion that this large force can primarily be attributed to a significant reduction of the electro osmotic flow (EOF, see section 2.6 for more details) through the pore. The EOF - basically caused by the negatively charged silicon nitride NP wall- seems to be suppressed by the electrical neutral lipid bilayer coating above. This smaller EOF in turn induced

an increase of the total threading force. More experiments with NPs and varying diameters were performed; two further examples are depicted in Figure 4.11. A force distance plot is presented for two different NPs with diameters of 43 nm and 37 nm (after coating). Both exhibit a significant increase in threading force of about 11 pN and 13 pN, respectively, compared to NPs with the same size, but without coating. The lipid bilayer of the 13 pN measurement was not performed by the SUV coating process, but by using giant unilamellar vesicles (GUVs). More details about this procedure and the associated experiment are presented in chapter 4.2.2.

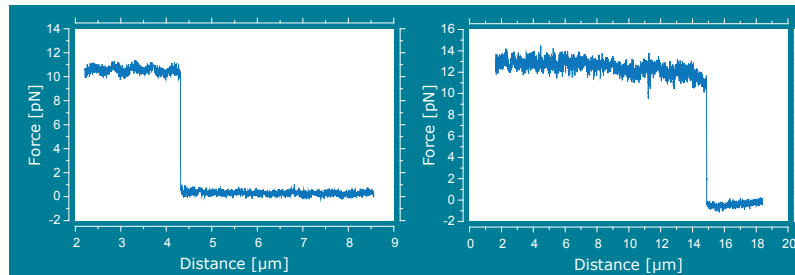


**FIGURE 4.11**  
dsDNA force - z-distance curves for lipid bilayer-coated NPs.

[Parameters Left: NP- $\varnothing$  = 52.6 nm (uncoated); NP- $\varnothing$  = 43 nm (with coating); Right: NP- $\varnothing$  = 46.6 nm (uncoated); NP- $\varnothing$  = 37 nm (with coating); applied Voltage and buffer as before]

Interestingly, the measured force magnitude is not 50 % larger as would be predicted for an uncharged NP wall<sup>[47,190]</sup>, but was instead 80 % larger (considering all 8 successful threading experiments with coated NPs). An explanation of how this result can be theoretically described will be discussed at the end of this chapter.

As noted earlier, the force exhibited an approximately linear dependence of the applied voltage, which is shown in Figure 4.12 for two coated NPs and three uncoated NPs with diameters in ranging between 50 mV and 100 mV. The measured force did not fluctuate by more than 15 % during time or when approaching or retracting the microbead from the pore<sup>[182,232]</sup>.

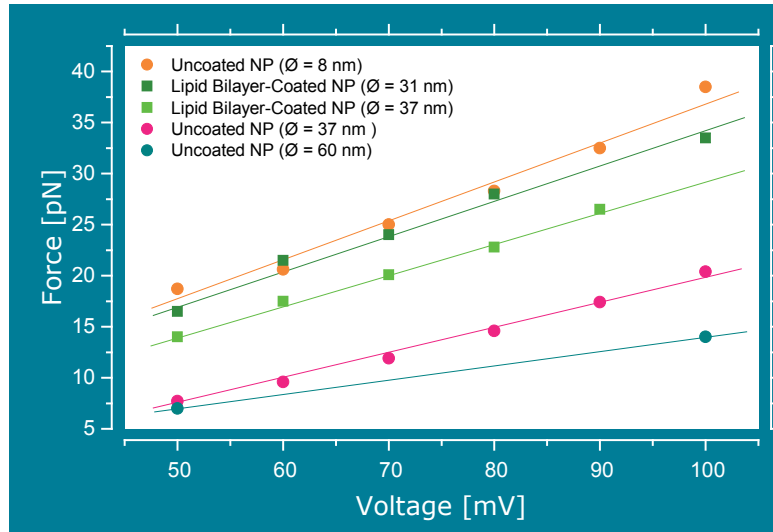


**FIGURE 4.12**

Relationship between threading force and applied voltage at constant z-distance for coated and uncoated NPs with different diameters.

[Parameters: buffer: 20 mM KCL and 2 mM Tris/HCL at pH 8]

Furthermore, this linear dependence confirms the assumption that the higher threading force for coated NPs (and thus the coating itself) is not appreciably influenced by the applied voltages up to 100 mV<sup>[182]</sup>. During all DNA-threading experiments pre-

sented herein, the ionic current signal exhibited no significant drop at the moment the DNA was completely pulled out of the NP (force drops down to zero), for both lipid coated and uncoated NPs.

As described in chapter 2.6, the total force acting on dsDNA inside a NP was significantly lowered by the hydrodynamic coupling of the EOF pointing in the opposite direction of the electrostatic force. This phenomenon lead to a strong reduction of the measured threading force<sup>[233]</sup>. Due to the fact that the EOF not only induces a drag force on the dsDNA, but also on the uncharged NP wall, the interplay between both drag forces lead to a gradually decreasing EOF (thereby increasing the total force) with decreasing NP diameter<sup>[182,233]</sup>. In addition to this general dependence of threading force and NP diameter, it was observed that for NPs with a diameter smaller than 10 nm the measured force considerably rose<sup>[182,232]</sup>.

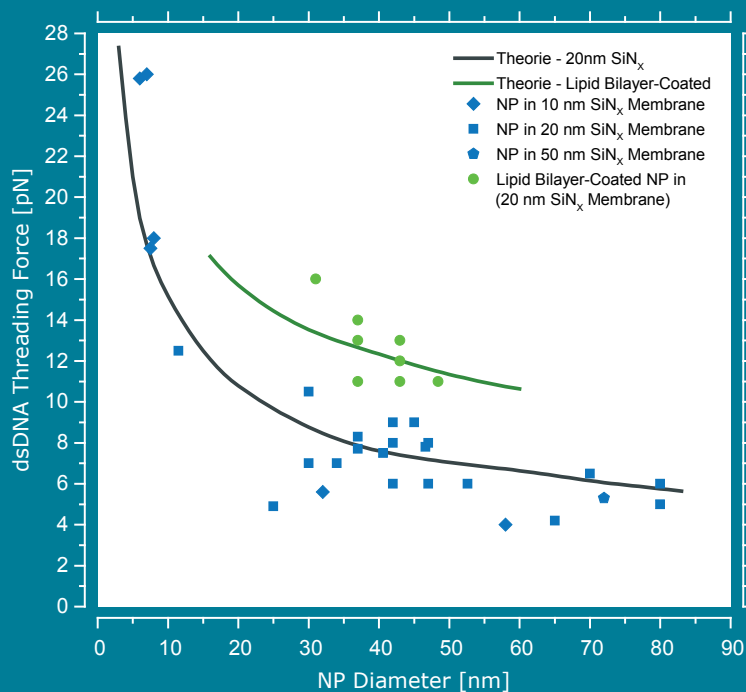
For qualitative comparison of the relationship between the measured threading force and the NP diameter, all data including results with lipid bilayer coated and uncoated NPs, are plotted in one diagram (see Figure 4.13).

**FIGURE 4.13**

Dependence of the dsDNA threading force on the NP diameters of uncoated pores (blue symbols) and lipid bilayer-coated pores (green symbols). The theoretical model for an uncoated NP (black line) fits best to the experimental data when the silicon-nitride membrane has a negative surface charge density of  $\sigma_m = -60 \text{ mC/m}^2$  and by introducing a hydrodynamic slip effect on the DNA surface with  $l_{\text{slip}} = 0.5 \text{ nm}$  (see text for more details).

The significant increase of the threading force for coated NPs can also be described by the theoretical model for coated NPs (green line) including a DNA slip length of  $0.5 \text{ nm}$  and a neutral surface charge density of  $\sigma_m = 0 \text{ mC/m}^2$  of the bilayer.

[Parameters: applied Voltage: 50 mV; buffer: 20 mM KCL and 2 mM Tris/HCL at pH 8]



According to the following description of these experimental results, a detailed discussion and theoretical interpretation of the respective findings is presented<sup>1</sup>. The blue data points, showing the results for uncoated silicon nitride membranes with varying thickness in a range between 10 nm and 50 nm, prove that the threading force is independent of the respective thickness<sup>[182,232]</sup>. Furthermore, the values for NPs with a diameter below 10 nm are considerably larger than experiments using NPs

<sup>1</sup> All theoretical descriptions, simulations und interpretations are developed by Andreas J. Meyer and Peter Reimann from the Condensed Matter Theory Group at Bielefeld University in close cooperation. In addition the simulations are supported by the Paderborn Center for Parallel Computing.

of comparable size formed either in a 20 nm thin silicon nitride membrane (that was additionally thermally oxidized before use)<sup>[48]</sup> or in a 60 nm thick SiO<sub>2</sub>/SiN<sub>x</sub>/SiO<sub>2</sub> membrane<sup>[47]</sup>. In comparison to a bare silicon nitride NP wall, the SiO<sub>2</sub> layer hypothetically leads to a stronger EOF. Moreover, the manufacturing process of the NP could play an important part in creating the surface charge of the NP wall. One could also expect that the ablation ratio between silicon and nitrogen atoms could vary, based on the use of a helium ion beam (as used in this experiments) in contrast to an electron beam, which would influence the surface charge and consequently the EOF<sup>[182]</sup>. Van Dorp et al. and Ghosal et al. already published theoretical expressions<sup>[47,190]</sup> for the total force acting on a dsDNA molecule inside a NP taking into account the dependency of the pore size. The finding that estimated experimental forces were 50 % smaller than the predicted values can be explained by the insufficient assumption of an electrically neutral surface of the NP wall. To solve this discrepancy a negative charge on the NP wall surface can be introduced<sup>[47,50,190]</sup>, providing an additional component to the EOF, and thus a reduction of the predictable threading force.

The experimental results for lipid bilayer coated nanopores (the green data points in Figure 4.13), allow the possibility to test how a modified NP surface charge affects the EOF and the measured threading force. It is clearly visible that the observed force for all eight coated NPs is significantly higher compared to NPs with the same diameter, but without coating. As described previously, this increase can only partially be attributed to the reduction of the NP diameter due to the coating. Such a variation in NP size (~10 nm smaller diameter) would only account for a small increase of the measured force. Therefore, it can be proposed that the enhanced force values are attributed to a significant reduction of the EOF through the NP. This reduction is caused by the electrically neutral lipid bilayer coating, suppressing the negative silicon nitride surface charge of the NP wall<sup>[182,232]</sup>.

For explanation of these experimental results by means of the electrohydrodynamic theory described in chapter 2.6.2, first the lipid-coated pores are examined. Between this lipid bilayer and the solid-state membrane material persists a 1–2 nm thick fluid water layer containing ions<sup>[51,230]</sup>, which lead to a strong shielding from the charge of the solid-state membrane (Debye screening). The resulting effective surface charge of the coated membrane is estimated to be insignificant, because the lipid bilayer itself does not exhibit any notable surface charge. From this assumption and setting  $\sigma_m = 0$  follows the conclusion that this model consistently undervalues the experimentally observed forces, when adopting no-slip boundary conditions for the rod-shaped particle modeling the dsDNA (i.e. for  $l_{slip} = 0$  nm)<sup>[182]</sup>. Variance of other parameters like pore shapes, membrane thicknesses as well as particle and membrane permittivity (within experimentally realistic limits) is not sufficient to explain the experimental findings. Presuming an effective reduction of the DNA charge<sup>[191,197,200,234]</sup>, this only enhances the discrepancy between theory and experiment. Another possible influence on the measured threading force may involve the axial DNA position within the NP. The simulation of force variation when the particle (a rod modelling the DNA) axis is permitted to deviate from the pore axis requires a full 3-dimensional numerical solution<sup>[182]</sup>. Much smaller reservoirs and rods have to be used in comparison with the axiallysymmetric case. The resulting force variations differ minimally by changing the

distance between particle and pore axis<sup>[182]</sup>. Stronger variations using longer rods and larger reservoirs are not expected<sup>[199]</sup>.

Another circumstance that has to be regarded is the oversimplification of the common homogeneous rod model<sup>[47,196,197,199]</sup>, which neglects some important structural properties of the experimentally used dsDNA. The phosphate groups of the DNA backbone are negatively charged and as such hydrophilic, whereas the nucleobases inside the grooves of the double helix are hydrophobic. These hydrophobic surfaces are known to give rise to significant hydrodynamic slip effects<sup>[212]</sup>, which seem to persist even in the presence of a nanoscopic substructure of alternating hydrophobic and hydrophilic domains. Therefore, a finite slip length  $l_{slip}$  that the DNA-particle surface is introduced. The green line in Figure 4.13 demonstrates that choosing a slip length of  $0.5 \text{ nm}$  leads to a good agreement of quantitatively describing the experimental findings for lipid bilayer coated NPs<sup>[182]</sup>. Moreover, the best fit  $l_{slip} = 0.5 \text{ nm}$  agrees very well with the slip length deducible e.g. from Figure 2 in the work of Kesselheim et al.<sup>[207]</sup>. Additionally, incorporating the detailed DNA structure of recent atomistic molecular dynamic simulations confirmed that non-zero fluid velocities are expected to appear along the DNA backbone<sup>[200,207]</sup>.

This successful theoretic model for lipid bilayer coated NPs can partially be adopted for uncoated NPs because the slip length ( $0.5 \text{ nm}$ ) is a property of the DNA model and as such, must remain unaffected<sup>[182]</sup>. However, a crucial difference compared to the coated membranes is the surface charge density  $\sigma_m$ , which is negative in the case of silicon nitride membrane and NP walls. Under experimental conditions  $\sigma_m$  can typically be estimated to be in the range between  $-15$  and  $-60 \text{ mC/m}^2$  as described in the literature<sup>[191-195]</sup>. Consequently, selecting  $\sigma_m$  as a fit parameter the black line in Figure 4.13 depicts our best fit to the experimental results leading to a surface charge density of  $\sigma_m = -60 \text{ mC/m}^2$ . Additionally, it could be verified that reasonable modifications of membrane thickness, pore shape, and DNA and membrane permittivities only vary this fit by a few percent<sup>[182]</sup>.

It has to be noted that in all theoretical results described here the well-established approximations  $D_{\pm} = 2 \cdot 10^{-9} \text{ m}^2/\text{sec}$  for the  $K^+$  and  $Cl^-$  diffusion coefficients  $D_{\pm}$  are utilized<sup>[235]</sup>. The variation of  $D_{\pm}$  in a range between  $1.5 - 2.5 \cdot 10^{-9} \text{ m}^2/\text{sec}$  is noteworthy and leads to resulting fit curves that still remain indistinguishable from those in Figure 4.13. The concentration of the ion bulk  $c_0$  is set to the experimental condition  $c_0 = 20 \text{ mM}$ . Possible variations in the expected threading force persist below 5 % using other  $c_0$  values between  $10 \text{ mM}$  and  $50 \text{ mM}$ . This is in good agreement with the values published by van Dorp et al.<sup>[47]</sup>.

## 4.2 Pore-Spanning Freestanding Lipid Bilayer Membranes

The NPs described so far are artificial solid-state nanopores with a thin silicon nitride membrane. These NPs – with or without a lipid bilayer coating – exhibit a certain limitation. Even though it is possible to vary the NP diameter by using lipid bilayer coatings (with different thickness<sup>[51]</sup>) this way of variation is limited by the pore manufacturing process and the type of lipids used. Furthermore, the explicit shape and surface charge of the NP and the surrounding region cannot be predicted with the highest accuracy and are difficult to reproduce. Given the lack of critical improvements in the pore manufacturing process (e.g. using HIM), an alternative type of nanopore will be investigated. A very promising approach and actually hot topic in the field of nanopore research is the study of biological pore-forming proteins. In contrast to solid-state NPs, biological pores – like  $\alpha$ -hemolysin – feature a well-known structure and thus offer a system with precise and predictable dimensions of the pore channel. Furthermore, the biological pores are promising for modification by means of genetic engineering. In general, there are two ways to incorporate such a biopore. The most common strategy is to embed the pore-forming protein in a lipid bilayer membrane<sup>[146,236-238]</sup> that mimics the natural surroundings (hydrophilic and hydrophobic regions) of the biopore (for more details see chapter 2.1.2). A different approach is the directed insertion of such a biopore into a solid-state nanopore (without any lipid bilayer) supported by a dsDNA-strand that is attached to the protein pore<sup>[239]</sup>. In this work three different methods were investigated for producing freestanding and stable lipid bilayer membranes, which are suitable for both biopore incorporation and later optical tweezers measurements. Besides these three methods, the so-called painting technique<sup>[223]</sup> was also tested for bilayer formation (also known as black lipid membranes). This method did not work as expected with the available silicon nitride chips and is not presented in this thesis. Also, the development of this method by Montal and Müller<sup>[224]</sup> cannot directly be adapted, because of limitations in the size and the geometry of the sample chamber. The limiting factor for experiments with the used OT setup, is the working distance of the objective lens, which permits a maximal distance between the bottom side of the sample chamber and the desired lipid bilayer membrane of approximately 250  $\mu\text{m}$ .

At first the results using the Langmuir-Blodgett transfer technique are presented, followed by the results of the attempt to create lipid bilayers by bursting of giant unilamellar vesicles. At last, experiments with the commercial available Ionovation Bilayer Slide with a thin teflon foil instead of a silicon nitride membrane are introduced.

### 4.2.1 Langmuir-Blodgett Monolayer Transfer

With the Langmuir-Blodgett (LB) technique it is possible to generate and characterize single-molecule thin films (monolayers) with highest control over the packing density of the used molecules, in this case phospholipids<sup>[240]</sup>. By utilizing a Langmuir Blodgett trough, it is feasible to transfer these lipid monolayers onto solid substrates<sup>[241]</sup>. This transfer of lipid monolayers was planned to generate a pore-spanning freestanding

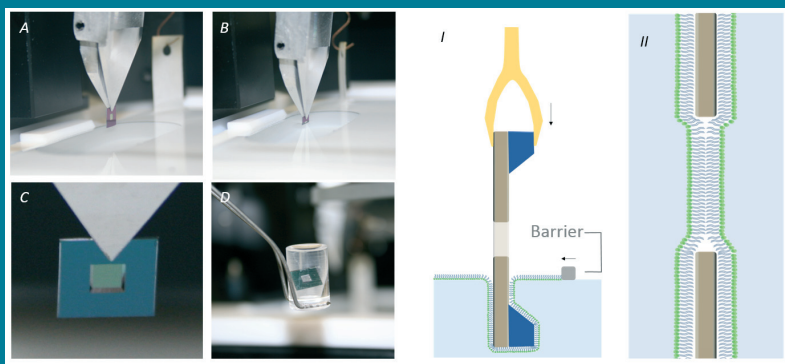
lipid bilayer. Simon et al. demonstrated in a similar attempt, that such a deposition (using a silicon membrane with micrometer pores) is possible, in principle<sup>[242]</sup>. The envisioned transfer procedure is illustrated in Figure 4.14. Image *I* schematically shows the transfer process by dipping a pore containing silicon nitride chip vertically through a lipid monolayer. The chip was clamped in a holder (image A, B and C) and slowly moved down. As a result of a hydrophobic coating with silane the hydrophobic tails of the phospholipids were oriented towards the chip surface. After complete transfer of a monolayer (on both sides of the chip), a bilayer formation inside pores with diameters of 3  $\mu\text{m}$  to 8  $\mu\text{m}$  was expected (see Figure 4.14 *II*).

Once the LB transfer was completed and the chip was fully submerged in the sub-phase solution, the setup had to be changed (for more details see chapter 3.3.2). Thus, after removing the chip out of the trough it was placed in the sample chamber.

**FIGURE 4.14**

Langmuir Blodgett transfer. Photographs of the dipping process (A and B), the silicon nitride microchip (C) and the small chip carrying container (D).

The sketches illustrate schematically the transfer process by dipping (*I*) and the desired final bilayer formation within the pore (*II*).



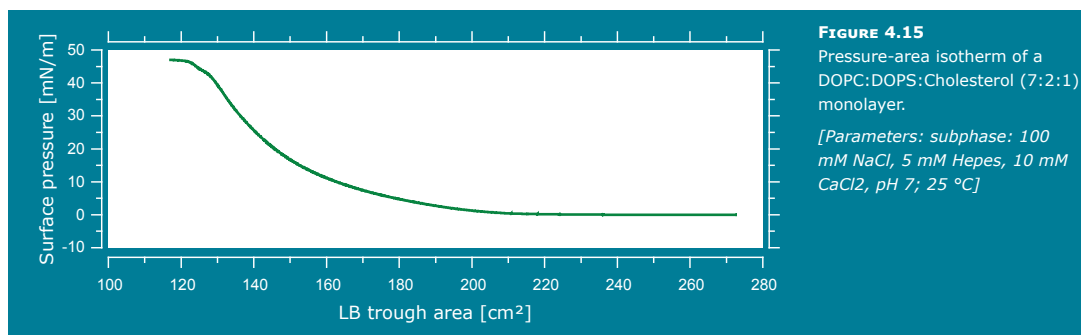
This step is crucial, because in first studies it was observed that the lipid bilayer membrane will be damaged as soon as it gets in to contact with air. As such, a small container was constructed to extract the chip out of the subphase (see Figure 4.14 D). Afterwards, the chip was transported to a bigger container filled with buffer and subsequently the sample chamber was assembled underwater. With this procedure the lipid bilayer is always surrounded by an aqueous subphase instead of air. Furthermore, the assembly the chip can be investigated by optical tweezers microscopy and the ability of  $\alpha$ -hemolysin incorporation can be proven.

#### ***Isotherm monitoring and LB monolayer transfer***

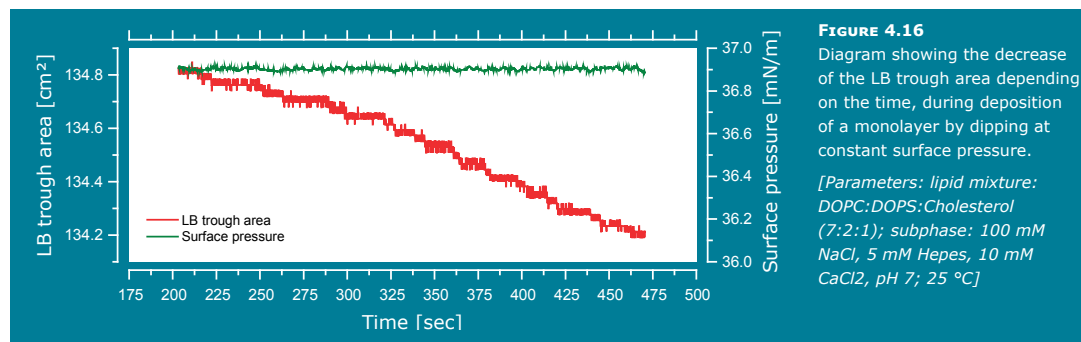
Prior to each monolayer transfer, a pressure-area isotherm was recorded to verify that the lipids were in good condition. In Figure 4.15 a representative isotherm is shown. While compressing the monolayer on the water surface, it undergoes several phase transformations (gaseous state, followed by the liquid state and condensed phase). At the end of the condensed phase, the so-called collapse occurs, here at surface pressure of  $\pi_{\text{col}} = 47 \text{ mN/m}$ . The pressure is plotted against the trough area (not against the monomolecular area) because a lipid mixture containing DOPC:DOPS:Cholesterol (7:2:1) was used<sup>1</sup>. The transfer of such an interfacial film was executed by the vertical LB film deposition procedure pictured in Figure 4.14. The monolayer was deposited at a surface pressure of  $37 \text{ mN/m}$ , after 10 *min* relaxation time via dipping (speed: 1 *mm/min*) of the chip through the air-water interface.

1 The monomolecular area can only be calculated if one lipid is utilized (or mixtures of lipids with nearly the same molecular mass and cross-sectional area)

This value of surface pressure was chosen because it refers to the condensed phase and corresponds also to the lateral pressure reported for biological bilayers<sup>[242,243]</sup> and is clearly under the collapse pressure.



The diagram in Figure 4.16 shows a typical transfer experiment. While the surface pressure was kept constant at 36.9 mN/m and the chip was dipped through the monolayer, the LB trough area linearly decreased from 134.8 cm<sup>2</sup> to 134.2 cm<sup>2</sup>. The quality of such a LB film can be estimated by controlling the transfer ratio  $T_R$ . This value describes the ratio between the removed lipid film area and the theoretical available substrate area<sup>[242]</sup>. In this experiment  $T_R$  was found to be approximately 1.1. This value is close to the ratio of 1 and indicates that the deposition of a complete monolayer onto the microchip succeeded. Additionally, it was observed that  $T_R$  and the quality of the LB film depends on the temperature, cleanliness of the subphase and of the microchip. The dipping speed (in a range between 1 – 5 mm/min) had - as reported in the literature<sup>[244]</sup> - no significant influence on  $T_R$ .



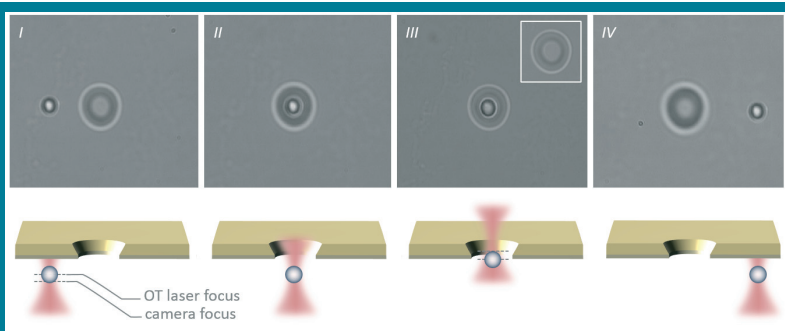
Once the monolayer deposition was finished, the excess lipids on the air-water interface were withdrawn by suction. Afterwards the microchip was extracted from the subphase by using the small container (Figure 4.14 D) without leaving the liquid surrounding.

Subsequent to the final underwater assembly of the sample chamber, it was mounted in the optical tweezers setup and electrically connected. In this experiment the resistance was approximately 500 M $\Omega$ . Taking all LB film transfers into account, the resistance for a successful attempt was about 100 – 500 M $\Omega$ . In comparison, extremely low resistances (k $\Omega$ -range) for a damaged bilayer or an unmodified microchip

were observed. Therefore, resistance in the referred experiment indicate that the LB deposition succeeded in forming a freestanding lipid bilayer in the micropore. In the next step microbeads were flushed into the bottom channel of the sample chamber to verify the stability of the lipid membrane. In Figure 4.17 four micrographs with corresponding schematics illustrate the interplay of an OT trapped microbead with the LB deposited freestanding lipid bilayer membrane. Because of a not perfect alignment of the focal plane of the trapping laser and the objective in this experiment, the trapped microbead was slightly out of focus (see gray dashed lines). The microbead was moved from the left side of the micropore to below it (see image *I* and *II*) and then pulled in a vertical direction through the pore. During this vertical movement the bead was hindered because it was not possible to pull it through the micropore. Subsequently, the bead changed its vertical position from the laser focus plane to the objective focus plane (see image *III*). Given the axial position of the bead and the feasibility to move the bead from its position to the right side beside the pore, the likelihood of the bead sticking to the pore rim can be excluded (image *IV*).

**FIGURE 4.17**

Micrographs and schematics of the micropore (diameter  $7\ \mu\text{m}$ ) after LB film deposition and its interplay with a microbead (diameter  $3\ \mu\text{m}$ ). In image *III* it is visible that the microbead is physically hindered from passing through the micropore (see “*Movie 4.1 LB-Bead above Micropore*” at the attached CD). The inset shows the annulus of the lipid bilayer membrane.



This behavior could be repeated in many experiments. Hence, the source of hindering seems to be a stable freestanding lipid bilayer membrane. It is worth noting that in experiments with silicon nitride chips without LB transfer it was possible to pull a microbead through the micropore without hindrance.

Additionally, the inset in image *III* shows the micropore with the LB film without the bead in front. The annulus of the freestanding part of the lipid bilayer membrane is also visible. These LB films were stable for hours ( $4\ \text{h}$  to  $36\ \text{h}$ ) without breaking or significant change in the resistance. The stability of the bilayer membrane during stress induced by the microbead appears to be realistic as well. The holding force in z-direction (parallel to the pore axis) applied by OT is about  $40\ \text{pN}$ . Mey et al. published in 2008 that freestanding bilayers (pore diameter  $1.2\ \mu\text{m}$ ) are stable up to rupture forces of  $25\ \text{pN}$  measured by AFM<sup>[245]</sup>.

#### **Air bubble interference**

Even though this preparatory work worked well, the envisioned  $\alpha$ -hemolysin incorporation could be never observed. In fact it was possible to observe an irregularity during the dipping process, which is schematically illustrated in Figure 4.18. Thus, the quality of the LB deposition was suspect and the transfer process was investigated again with highest attention.

Due to the small size of the silicon window ( $2 \times 2 \times 0.2\ \text{mm}$ ) and the surface tension

the monolayer did not come into contact with the inner area of the window. Therefore, no monolayer was transferred to the “*window-side*” of the silicon nitride membrane leaving an air bubble inside the window instead. This air bubble was not detected by microscopy, because its surface towards the liquid was parallel to the silicon nitride membrane, avoiding any interference effects (which are usually visible due to the curvature and varying refraction indices).

In previous studies the presence of an air bubble, located directly above a pore and thereby closing it, resulted in a very high  $G\Omega$  seal. However, in the actual experiments a resistance in the  $M\Omega$  range was always observed. The reason for this can be primarily attributed to the underwater mounting process of the sample chamber leading to a slightly leaking chamber. Based on these findings, the micrographs in Figure 4.17 have to be reinterpreted. It appears that the microbead was not pulled against a bilayer but against a monolayer at the buffer air interface. This would also explain why an incorporation of  $\alpha$ -hemolysin was never observed.

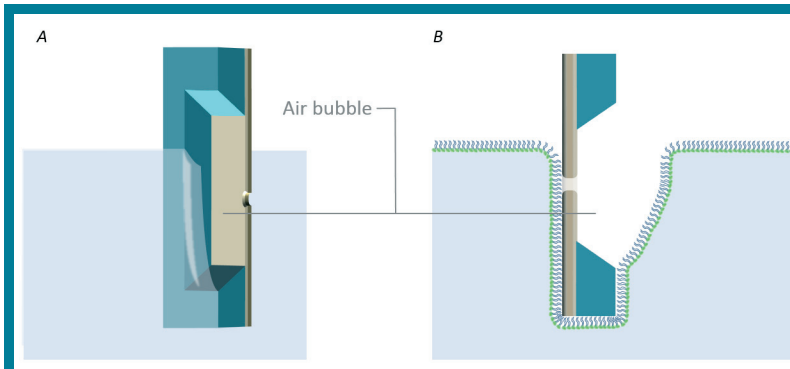


**FIGURE 4.18**

Schematic illustration of trapping an air bubble inside the window volume during the dipping process. This effect avoids the formation of a lipid bilayer within the pore region and prevents the biopore incorporation.

Further modifications of the silanization process, variations of the dipping angle and an upgraded mounting procedure did not improve the LB transfer. Overall the Langmuir Blodgett transfer is not the ideal method (at least with the parameters presented here) to generate freestanding lipid bilayers that are accessible for OT measurements. In the next chapter 4.2.2 an alternative method will be presented that utilizes giant unilamellar vesicles.

### 4.2.2 Bursting of Giant Unilamellar Vesicles

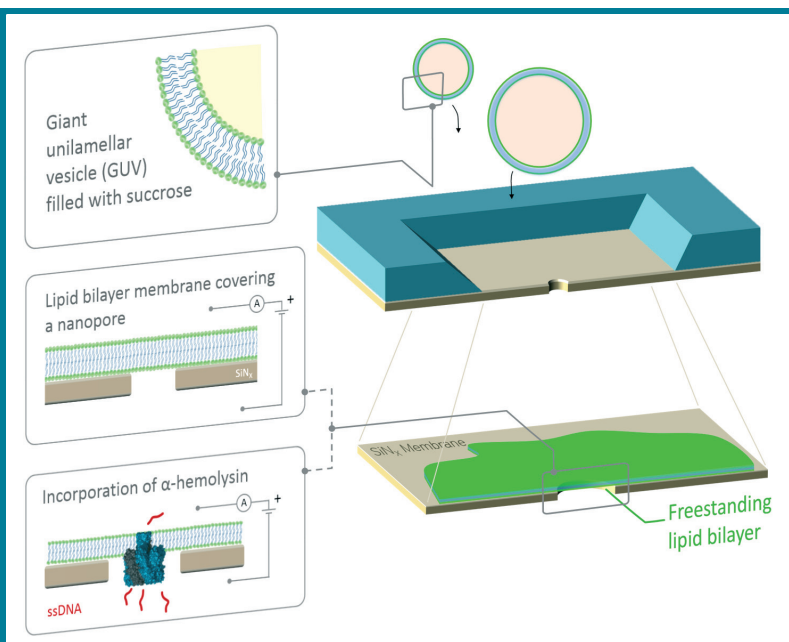
Giant unilamellar vesicles (GUVs) are prepared with a defined lipid composition and are filled with sucrose, giving them a higher density and allowing them to sink down in the used buffer solutions. In the experiment, a small amount of GUV solution was added to the buffer in the top compartment of the sample chamber. After filling, the GUVs sank down within seconds and ruptured on the silicon nitride surface as illustrated in Figure 4.19. If the vesicle fusion and rupture takes place at the middle region of the membrane, where the NP is located, it forms a freestanding lipid bilayer membrane covering the solid-state pore.

**FIGURE 4.19**

Schematic sketch of a GUV sinking and bursting process. In the upper part one can see the giant unilamellar vesicles sinking down to the silicon nitride membrane.

For better sinking properties the GUVs are filled with sucrose. The GUVs burst after coming into contact with the very hydrophilic surface resulting in a freestanding lipid bilayer membrane covering the NP.

To verify if the NP was sealed by a bilayer, the transmembrane current was monitored while a constant voltage was applied. Afterwards,  $\alpha$ -hemolysin was incorporated into the bilayer and ssDNA translocation experiments were performed.



A transmembrane voltage was applied to verify that the NP was completely covered with a lipid bilayer and not leaking. The ionic current during this process was observed and recorded simultaneously with imaging by fluorescence video microscopy. A distinct drop in the current signal close to zero  $\mu\text{A}$  in conjunction with an optical monitored bursting event, was characteristic for a successful lipid bilayer formation. If the determination of the ionic current to applied voltage characteristics yielded a  $G\Omega$  seal, one can take the existence of a freestanding lipid bilayer for granted. Once a bilayer was formed,  $\alpha$ -hemolysin could be incorporated and ssDNA translocation events could be recorded.

#### **Experimental conditions for GUV sinking and rupture**

To successfully perform the above described experiment, it was crucial to understand under which conditions the GUVs would rupture properly. For this purpose the properties of the surface and the surrounding buffer were important as well as the lipid mixture and the concentration of the sucrose inside the GUVs. Initially the size and the shape of GUVs were prepared by the established electroformation technique (see

chapter 3.3.3 for more details) and monitored via fluorescence microscopy. The GUVs shown in Figure 4.20 fabricated with common electroformation parameters as, for instance, described in the work of Heinemann et al.<sup>[246]</sup>. The first lipid mixture consists of DOPC:DOPG:Rhod-DOPE (99:0.995:0.005 mol%) filled with a 300 mM sucrose solution. In Figure 4.20 A and D, freshly generated GUVs with a size of approximately 5  $\mu\text{m}$  to 20  $\mu\text{m}$  were visible. In contrast, the vesicles noticeable in Figure 4.20 B and C were two days old and smaller than vesicles within the fresh GUV solution. Additionally, fewer vesicles were observed. Many of these small vesicles can be seen in the first three images. This appears unfavorable, because only vesicles with a size of 10  $\mu\text{m}$  are useable for bursting experiments. However, testing the sinking properties using the sample chamber with an embedded silicon nitride chip (Figure 4.20 D), showed that bigger vesicles sank down to the membrane much faster than the smaller GUVs. Hence, the presence of smaller GUVs in the vesicle solution is a negligible side effect.

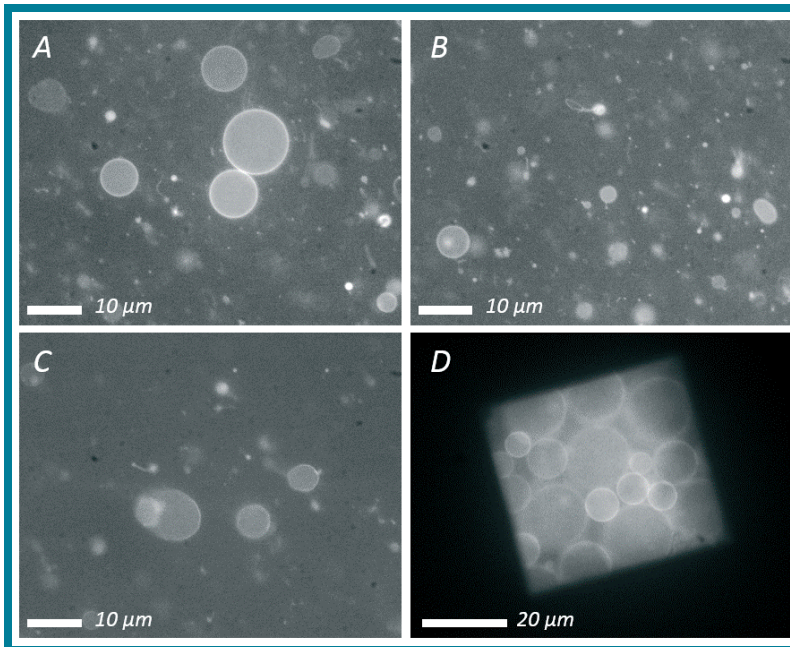


**FIGURE 4.20** Fluorescence microscopy images of GUVs for controlling size and shape of the vesicles. Images A and D show freshly produced GUVs, whereas for images B and C a two day old vesicle solution was used. In contrast to the first three images (big droplets of GUV solution on a glassslide), the fourth image was taken through a silicon nitride window.

[Parameters: Lipid mixture: DOPC:DOPG:Rhod-DOPE (99:0.995:0.005 mol%); GUV sucrose concentration: 300 mM; buffer: 20mM KCL and 2 mM Tris/HCL at pH 8]

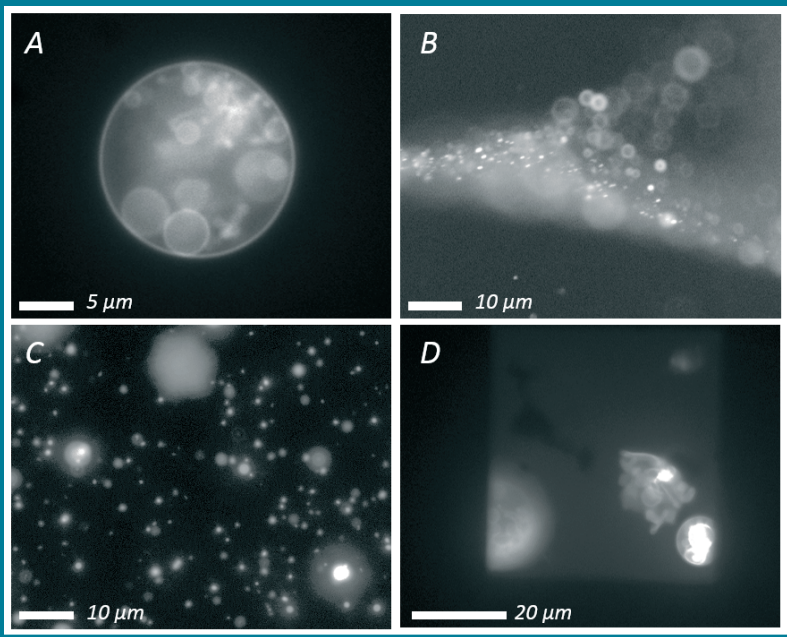
Different lipid mixtures and various concentrations of sucrose were tested in tandem to the experiments for characterizing size and shape of the GUVs. For lipid mixtures, various compositions of DOPC, DOPG and Rhod-DOPE were prepared, as well as additional mixtures that contained DPhPC, DOPS or Cholesterol. The resulting quality in size and shape did not considerably change compared to the composition used initially. Therefore, the mixture of DOPC:DOPG:Rhod-DOPE was selected to test different sucrose concentrations. Figure 4.21 shows attempts with 100, 200 and 500 mM sucrose. GUVs filled with 100 mM sucrose exhibit multiple vesicle structures (Figure 4.21 A) and bursting experiments on a silicon nitride membrane with this filling did not work (Figure 4.21 D). A high concentration of 500 mM sucrose led to some cloudlike phases with a high density of small vesicles (Figure 4.21 B). Thus, this

concentration could be set aside for the purpose of this work. The resulting GUVs prepared with 200 mM sucrose are in general comparable with those filled with 300 mM, but nevertheless, the amount of GUVs with a diameter of more than 10  $\mu\text{m}$  was much lower and the most vesicles had a size of proximately 1  $\mu\text{m}$  (Figure 4.21 C). In conclusion, the first lipid mixture (with a filling of 300 mM sucrose) led to most promising GUVs.

**FIGURE 4.21**

Fluorescence microscopy images of GUV solutions prepared with different concentrations of sucrose. Images A, B and C were selected to show the quality of the respective GUV solution. Image D pictures the failed attempt to let this multiple vesicle structures burst on a silicon nitride surface.

[Parameters: Lipid mixture: DOPC:DOPG:Rhod-DOPE (99:0.995:0.005 mol%); GUV sucrose concentration: A = 100 mM ; B = 500 mM; C = 200 mM; D = 100 mM; buffer: 20mM KCL and 2 mM Tris/HCL at pH 8]

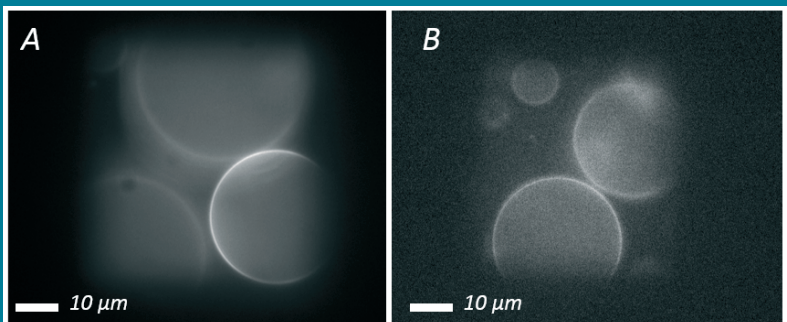


As indicated in Figure 4.20 D, the first GUV fusion and rupture experiments on silicon nitride membranes did not come to fruition, although the GUVs did sink down and come into contact with the (unmodified) membrane surface. This case is also illustrated in Figure 4.22, but here the surface was modified by a covalent functionalization with the silane TDTS, following the work of Heinemann et al.<sup>[246]</sup>.

**FIGURE 4.22**

First rupture attempts on silanized silicon-nitride chips. The fluorescence micrographs show GUVs lying on top of the membrane. Over a long time period the vesicles did not burst.

[Parameters: Lipid mixture: DOPC:DOPG:Rhod-DOPE (99:0.995:0.005 mol%); GUV sucrose concentration: 300 mM; buffer: 20mM KCL and 2 mM Tris/HCL at pH 8]



The latter authors describe that vesicle fusion and bursting on a surface depend on the interplay between the lipid headgroups and the respective surface<sup>[246,247]</sup>. A surface with high charge density is mandatory to enhance the vesicle fusion, rupture and

burst process<sup>[101,246]</sup>. The first tests with silanized silicon nitride membranes also led to no burst events, although very big and nicely shaped GUVs (approx. 25 – 35  $\mu\text{m}$  in diameter) did contact with membrane (see Figure 4.22 A and B). These experiments were repeated several times and the GUVs were also observed over a long period of time (up to 2 h). Varying the composition of the lipid mixture or applying transmembrane voltages did not lead to successful vesicle bursting events.

In order to determine ideal experimental conditions and parameters for vesicle fusion, different surface materials and buffer solutions were investigated. In Figure 4.23, six examples for successful rupture attempts are shown. The GUVs that burst on unfunctionalized mica, as well as on glass and silicon nitride surfaces, which are treated with a hot piranha solution (see section 3.3.3 for more details), were observed. In these experiments a small droplet (2 – 5  $\mu\text{l}$ ) of the GUV solution was added to a reservoir filled with different buffer solutions. It was also interesting that the GUVs ruptured in low and high salt concentrations (20 mM up to 2 M KCl). Using pure MilliQ®-water instead of a KCl buffer, the vesicles did not rupture. As it is visible in all images of Figure 4.23, the bursting of vesicle resulted in a more or less roundly shaped patch on the respective surface. In some cases small vesicles remained on top of the formed lipid bilayer. This effect depended on the former quality of the GUVs, but it should not affect the stability or sealing characteristics of the freestanding part of the lipid bilayer as long as these small vesicles are not lying directly on top of the nanopore region. Image D in Figure 4.23 also illustrates several ruptured GUVs (four in this case) fusing and forming a continuous bilayer. This could be advantageous if a first GUV burst near the NP without sealing it properly, thus preserving the possibility for another vesicle to build the freestanding part of the bilayer by fusion.

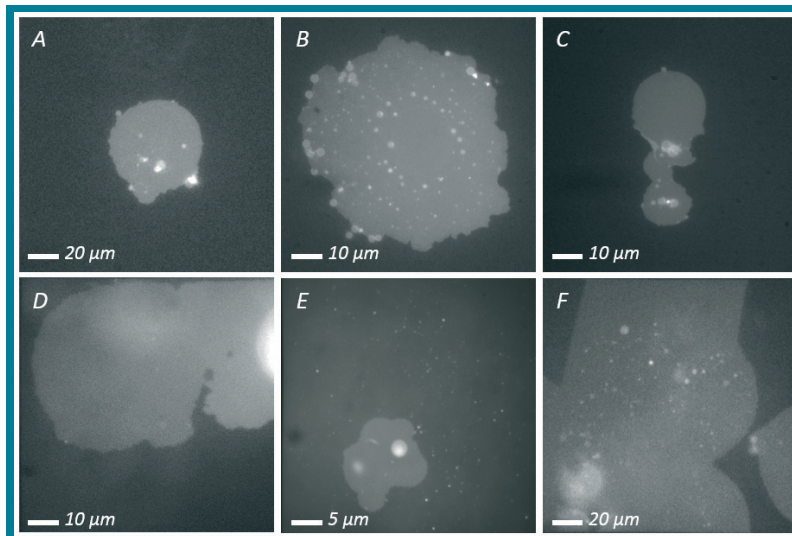


**FIGURE 4.23**

Fluorescence microscopy images of GUVs ruptured on different surface materials and with varying solutions. The mica surface was used unfunctionalized, whereas the glass or silicon nitride surface was made hydrophilic with piranha solution.

[Parameters: Lipid mixture: DOPC:DOPG:Rhod-DOPE (99:0.995:0.005 mol%); A: glass & 2 M KCl; B: glass & 20 mM KCl; C: mica & 20 mM KCl; D: silicon nitride & 20 mM KCl; E: silicon nitride & 150 mM KCl; F: silicon nitride and 2 M KCl; every KCl solution contained also 2 mM Tris/HCL and had a pH of 8]

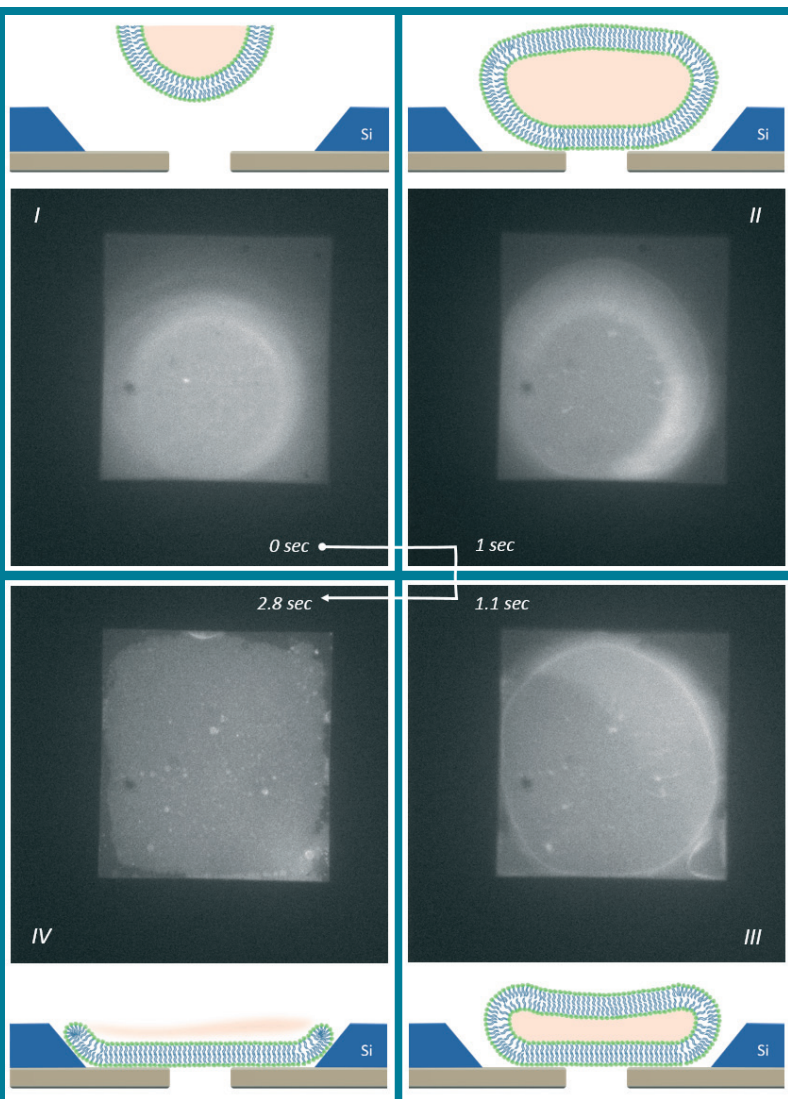
### Accurate NP sealing by GUV rupture

This experiment was successfully performed based on the preliminary characterization of the optimal lipid composition, sucrose and buffer concentration, as well as surface preparation (for establishing an effective generation of freestanding lipid bilayers by GUV rupture). The fluorescence microscopy images and corresponding schematic sketches in Figure 4.24 show an ideal sinking and bursting process.

**FIGURE 4.24**

Schematic sketch of a GUV bursting process. In the upper image one can see the giant unilamellar vesicles sinking down to the silicon nitride membrane. The GUVs were filled with sucrose for better sinking properties. The GUVs burst after lying down on the silicon nitride surface and some shape deformation (see also the "Movie 4.2 GUV sinking and NP sealing" at the attached CD).

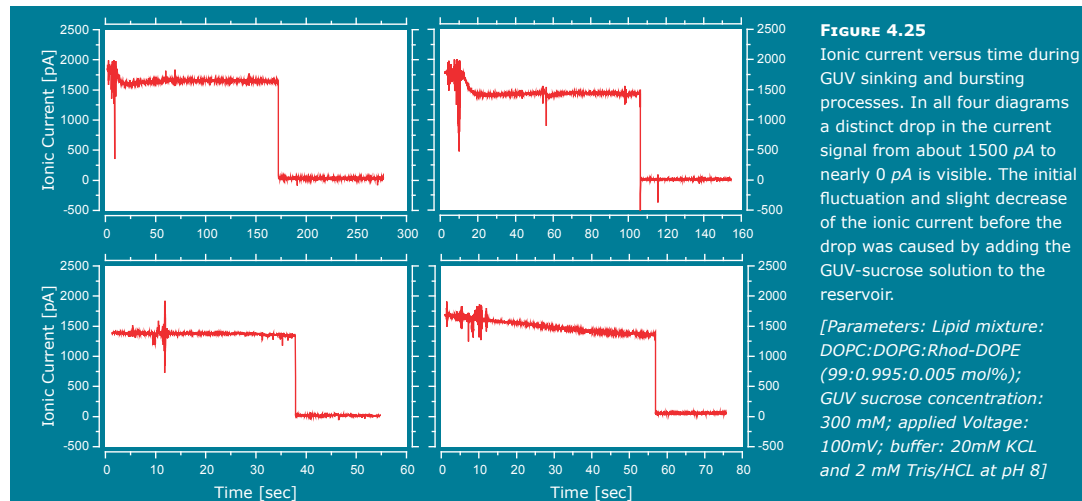
[Parameters: Lipid mixture: DOPC:DOPG:Rhod-DOPE (99:0.995:0.005 mol%); GUV sucrose concentration: 300 mM; buffer: 20mM KCL and 2 mM Tris/HCL at pH 8]



In this case a large GUV with a diameter of approximately  $45 \mu\text{m}$  required 20 sec to sink down to the membrane once the vesicle solution was added to the top of the reservoir. The rupture process took place within 3 sec, resulting in a continuous lipid bilayer covering nearly the whole surface area of the silicon nitride window. In images II and III the shape deformation (flattening) of the GUV is clearly observable,

indicating that the rupture process itself was induced by the adhesion of the GUVs to the surface. The forces acting on the suspended membrane upon bursting were also lowered by this deformation effect, due to the fact that large membrane areas (of the intact GUV) were already attached to the silicon nitride support<sup>[246]</sup>.

The sinking and bursting process was investigated by optical fluorescence microscopy, as well as by simultaneously measuring the ionic current while a constant transmembrane voltage was applied. In Figure 4.25, four examples for successful sealing events by GUV rupture are presented. The moment of closing the NP, and thus hindering the ionic transport, can be clearly identified for each experiment and agrees strongly with the optical observation (see also "Movies 4.3 – 4.5" at the attached CD).



Initial fluctuations in the ionic current signal appear to be due to small movements or jiggling of the electrodes during addition of the GUV-sucrose solution to the top reservoir of the sample chamber. The slight decrease in the current signal was caused by the added GUV solution. Due to the GUV fabrication protocol the vesicles were not only filled, but also solvated in 300 mM sucrose which is not perfectly soluble in water (without stirring), and thus replaced charge-carrying ions near the electrode. This effect could be observed repeatedly and clearly depended on the respective sucrose solution. A 10 mM sucrose solution had no significant influence on the current signal, but was not suitable for proper sinking experiments.

Additional peaks in the first third of the time scale refer to closing the faraday cage by hand. This cage, as well as the patch-clamp amplifier are newly integrated into an already existing fluorescence microscopy setup (see chapter 3.2.2 and Figure 4.26). This cage reduced the noise of the ionic current signal by more than a factor of 10. Furthermore, a new software for recording and monitoring the current and voltage signals was implemented in LabView<sup>1</sup>.

1 This LabView program was coded by Dr. Lukas Bogunovic.

After a successful sealing event the ionic current was further monitored (at least 20 sec ) to assure that the freestanding bilayer was stable (compare Figure 4.25). This is important, because the sample chamber has to be moved from the fluorescence microscopy stage to the OT setup.

**FIGURE 4.26**

Photographs of the new faraday cage and patch-clamp amplifier integrated into the existing fluorescence microscopy setup.

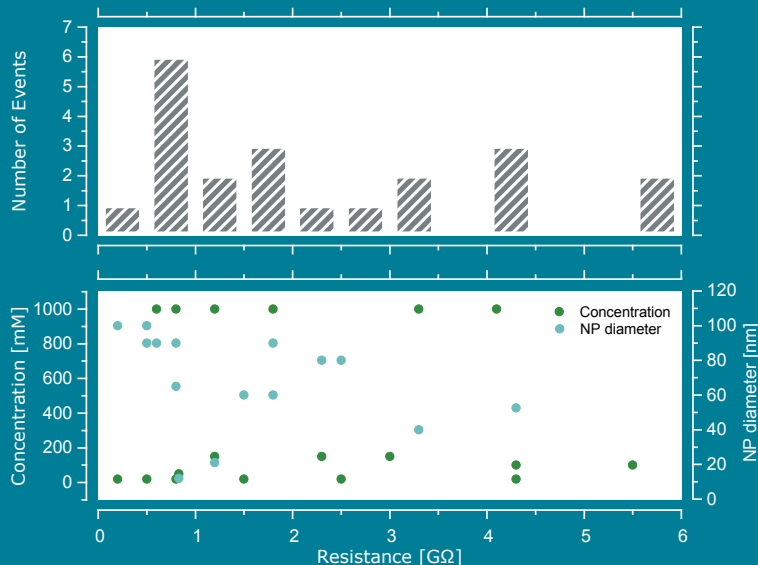


The ideal handling of the electrode connection/disconnection is also crucial for the lifetime of the freestanding lipid bilayer. First attempts revealed that the bilayer would break if the glass capillary electrodes were not pulled out of the respective reservoir, before the patch-clamp amplifier was switched off (due to possible voltage peaks). This failure also occurred, if the voltage was not applied anymore. At the OT setup, first the patch-clamp amplifier had to be switched on before placing the electrodes into the reservoirs. Then, a voltage was applied again to verify the intactness of the lipid bilayer membrane. Immediately after verification that the actual membrane was undamaged, the ionic current was characterized for different applied voltages (IU-curve) from  $-100\text{ mV}$  to  $100\text{ mV}$ , always featuring the expected linear dependence. With this data, the resistance for each bilayer was calculated. The membrane was considered suitable for further incorporation experiments with  $\alpha$ -hemolysin when the resistance was within the appropriate  $G\Omega$  range and exhibited a stable ionic current signal over a long period of time.

**FIGURE 4.27**

The top histogram illustrates the distribution of the measured resistances in the  $G\Omega$  range. The bottom diagram shows that the height of the resistance was independent of both the sealed NP diameter and the concentration of KCL buffer.

[Parameters: every KCL solution contained also  $2\text{ mM}$  Tris/HCL and had a pH of 8]



More than twenty experiments succeeded in creating a stable freestanding lipid bilayer membrane, where a stable current signal after changing the setup and observing three-digit  $k\Omega$  to  $G\Omega$  sealing was measured. The top histogram in Figure 4.27 shows the distribution of the measured resistances ranging from 0.2  $G\Omega$  to 5.5  $G\Omega$  (with a mean resistance of 2.2  $G\Omega$ ). The broad distribution was independent of both the diameter of the sealed solid-state nanopore and the used buffer concentration, which is visible in the bottom diagram of Figure 4.27.

#### **Bilayer breakage effects and indirect coating by GUVs**

In case of a damaged freestanding lipid bilayer membrane after changing the setup or after recording an IU-curve, it was occasionally observed that the region located to the NP was darker than before. This effect is visible in Figure 4.28 A. In addition to the dark spot in the middle the bilayer appeared to be "broken" in the upper left area of the former roundly shaped patch. This result could be an indication for a non-uniform hydrophilic surface. A very similar observation is presented in image B and C (Figure 4.28); in this case the darker spots in the middle of the silicon-nitride window were formed immediately after rupture of several GUVs. The reason for this effect could be found by imaging these chips with AFM. So-called "nano-volcanoes" were discovered in direct proximity to the nanopore<sup>[130]</sup> and exhibited a height of approximately 40 nm. They were caused by imaging the NP area with HIM after drilling the pore (see AFM images and more information here<sup>[130]</sup>).

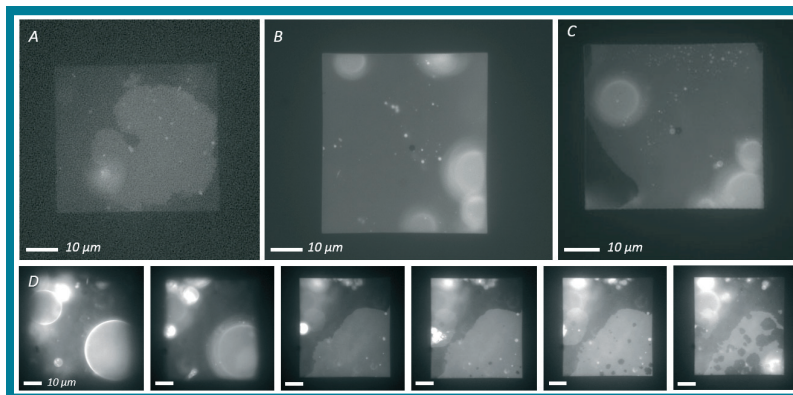


**FIGURE 4.28**

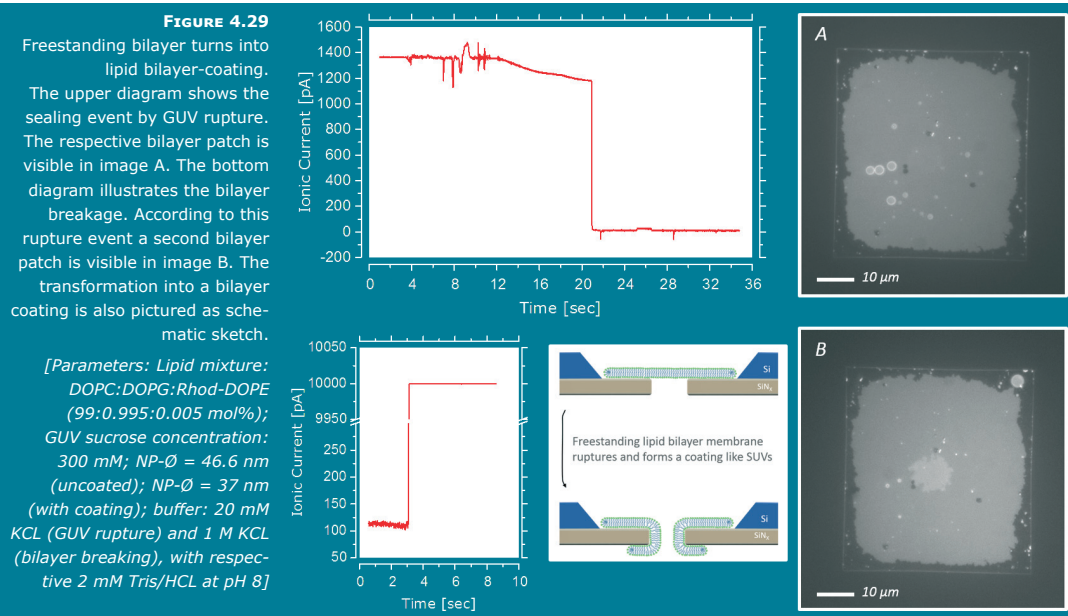
A: destroyed lipid bilayer after setup change.  
B and C: "nano-volcanoes" near the NPs disturb formation of the freestanding lipid bilayer.  
D: image sequence illustrating growing of dark spots, and thus eliminating the uniform bilayer.

[Parameters: Lipid mixture: DOPC:DOPG:Rhod-DOPE (99:0.995:0.005 mol%); GUV sucrose concentration: 300 mM; buffer: 20mM KCL and 2 mM Tris/HCL at pH 8]

Additionally intriguing results are illustrated in Figure 4.28 D. This image sequence show a GUV bursting and forming a big patch on the surface. Small dark spots emerged and grew with time shortly afterwards. After approximately 23 sec more than half of the former continuous lipid bilayer patch disappeared. The reason may be attributed to a non-uniformly modified silicon-nitride surface. Perhaps the membrane was not clean enough and some dirt particles influenced the lipid bilayer stability or this effect occurred during NP drilling process by HIM. Even though this behavior was only observed once, it underlines again the importance of the preparation and treatment of the silicon-nitride chip in order to establish a running lipid bilayer formation routine.

The destruction of a freestanding lipid bilayer membrane during voltage clamp measurements is not in any case unfavorable as described in the previous paragraph. The

two diagrams in Figure 4.29 show both the desired sealing of a NP by GUV rupture and the breaking of the freestanding lipid bilayer membrane. The latter did not lead to a dark spot, but to a second lipid bilayer patch at the bottom side of the silicon nitride membrane. This is obviously visible comparing the fluorescence microscopy images before (A) and after bilayer breaking (B) in Figure 4.29. The schematic representation in the same figure visualizes the transformation from a freestanding lipid bilayer membrane to a lipid bilayer coated NP (similar to the coating by SUVs). The height of the ionic current signal after membrane breaking was calculated by changing the buffer concentration from 20 mM KCL to 1 M KCL during the attempt to incorporate  $\alpha$ -hemolysin. The actual current signal (21 000 pA) was even higher than the 10 000 pA as shown in this figure (the recording LabView software has a cutoff limit of 10 000 pA). Nevertheless, the actual measured current was readable on the digital display of the patch clamp amplifier.



According to the discovery of this new way of lipid bilayer coating, the buffer was changed back to 20 mM KCL. This was necessary for later OT measurements, as well as for verification of complete NP wall coating. Because of a reduction of the NP diameter in the expected range, straight DNA-threading experiments were performed (see the obtained force-distance curve in Figure 4.11 on the left).

#### ***Incorporation of $\alpha$ -hemolysin and free ssDNA translocation***

In the following paragraphs the data for a successful GUVs rupture and  $\alpha$ -hemolysin incorporation experiment at low salt concentration (50 mM KCL) will be presented. The upper diagram in Figure 4.30 demonstrates the GUV rupture and NP sealing event by ionic current recording. After changing the setup a very stable ionic current signal with low noise was observed. As expected the current signal was linear dependent on the applied voltage. The NP was properly sealed and the electric resistance

was determined to be  $0.8 \text{ G}\Omega$ . First,  $5 \mu\text{l}$  fresh prepared  $\alpha$ -hemolysin ( $2.5 \text{ ng/ml}$ , solved in  $20 \text{ mM}$  KCL buffer) was added to the top reservoir, while a constant transmembrane voltage of  $200 \text{ mV}$  was applied. No distinct change in current signal was observable after  $10 \text{ min}$ . After  $5 \mu\text{l}$  of the  $\alpha$ -hemolysin solution was additionally added and  $10 \text{ min}$  elapsed, the first recorded steps in the ionic current signal were taken.

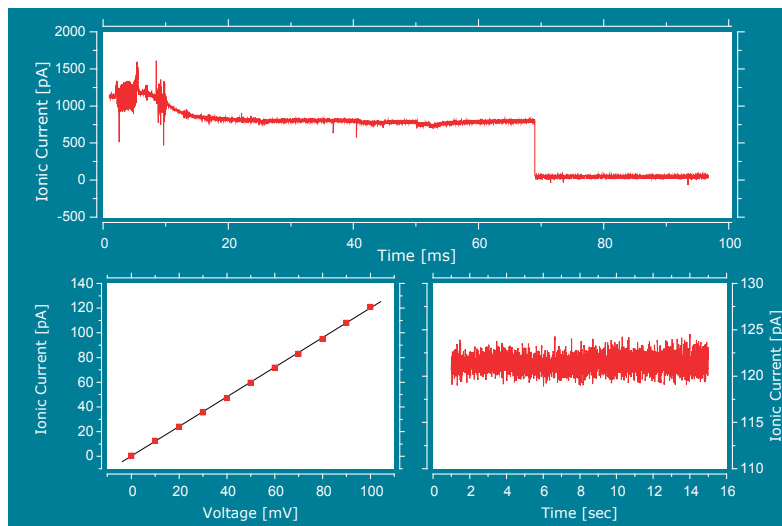


**FIGURE 4.30**

Upper diagram: Ionic current vs time during a GUV sinking and bursting process.

The IU-curve on the bottom left exhibits linear dependency. Also a stable ionic current signal with low noise was observed.

[Parameters: Lipid mixture: DOPC:DOPG:Rhod-DOPE (99:0.995:0.005 mol%); GUV sucrose concentration:  $300 \text{ mM}$ ; applied Voltage:  $100 \text{ mV}$ ; buffer:  $50 \text{ mM}$  KCL and  $2 \text{ mM}$  Tris/HCL at pH 8]

Four examples for single or multiple step events caused by incorporation of  $\alpha$ -hemolysin into the freestanding lipid bilayer membrane are shown in Figure 4.31. The measured stepwise increase of the ionic current can be just temporary (step up and step down), as well as long-lasting (images I and II). Due to the same height of each step, it can be hypothesized that each step event refers to the incorporation of a single  $\alpha$ -hemolysin pore into the lipid bilayer membrane.

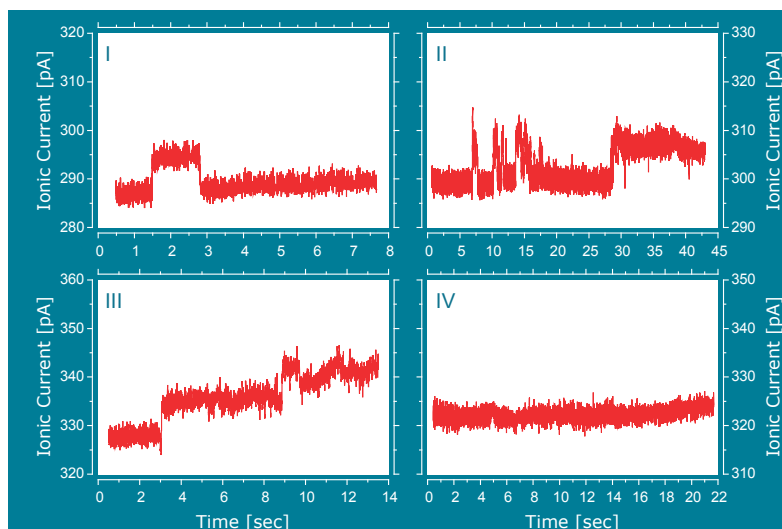


**FIGURE 4.31**

Discrete steps in the current signal during incorporation of single  $\alpha$ -hemolysin pores into the lipid bilayer (I, II and III). After integration of (probable) three biopores the ionic current was very stable and had low noise (IV).

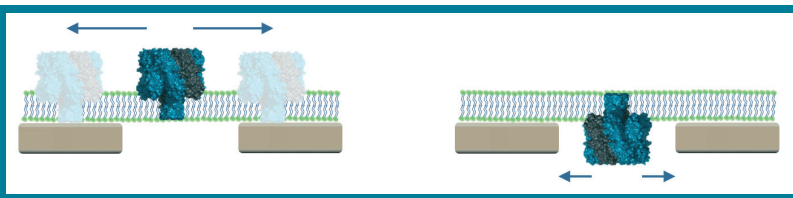
[Parameters: Lipid mixture: DOPC:DOPG:Rhod-DOPE (99:0.995:0.005 mol%); GUV sucrose concentration:  $300 \text{ mM}$ ; applied Voltage:  $200 \text{ mV}$ ; buffer:  $50 \text{ mM}$  KCL and  $2 \text{ mM}$  Tris/HCL at pH 8]

The diagram III in Figure 4.31 shows several biopores that were incorporated one by one. After approximately 5 min, three individual  $\alpha$ -hemolysin pores were steadily integrated into the bilayer and exhibited a stable current signal (diagram IV).

The observation for a current step down (Figure 4.31 I) is usually not expected in context of  $\alpha$ -hemolysin incorporation, once such a biopore is integrated into a lipid bilayer it will not be extracted anymore. Due to the fact that the  $\alpha$ -hemolysin was added to the *trans* reservoir, this finding entails that these biopores can incorporate not only into the bilayer above the NP, but also next to it (see Figure 4.32). Additionally, the biopore is not restricted to the place of incorporation and can diffuse within the lipid bilayer membrane<sup>[248]</sup>. Based on this discovery the biopore containing droplet was added to the bottom compartment of the sample chamber in subsequent experiments. This prevents the  $\alpha$ -hemolysin from diffusing outside of the NP area as it is indicated by the arrows in the sketch in Figure 4.32.

**FIGURE 4.32**

The diffusion abilities of  $\alpha$ -hemolysin pores within a bilayer depends on the orientation with regard to the solid-state NP.

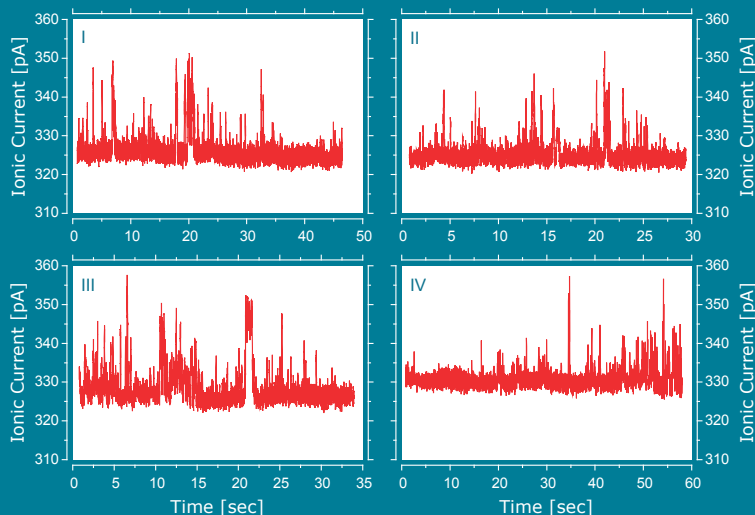


As it is visible in Figure 4.31 D, the ionic current signal was very stable and had a low noise level, which is important for accurate investigation and discrimination of later translocation events. As introduced in chapter 3.3.3, a DNA-microbead construct with a single-stranded overhang (poly(dT)<sub>130</sub>) was proposed for controlled OT force measurements. These ssDNA oligos (with poly(dT)<sub>130</sub>) were, at this time, not yet available, and thus free translocation of 12 bases short oligos was investigated instead.

**FIGURE 4.33**

Four diagrams presenting free translocation of single-stranded DNA fragments by the coulter counter method.

[Parameters: Lipid mixture: DOPC:DOPG:Rhod-DOPE (99:0.995:0.005 mol%); GUV sucrose concentration: 300 mM; applied Voltage: 200 mV; buffer: 50 mM KCL and 2 mM Tris/HCL at pH 8]



These oligos should be detected by the coulter-counter method while they are translocating through the  $\alpha$ -hemolysin pore. For this method a constant transmembrane

voltage was applied and the translocation events should appear as a significant short-time change in the ionic current signal. In Figure 4.33 four different measurements exhibiting distinct translocation events are presented. These events look similar to former applied coulter counter experiments using solid-state NPs<sup>1</sup>, but translocation times are much longer than expected for such short ssDNA fragments with a length of 12 bases.

As it is shown in the histogram<sup>2</sup> of Figure 4.34 the translocation time with the most recorded number of events was approximately 100 msec. There were also a small number of peaks with a translocation time of more than 400 msec, but the main part of events was between 50 msec and 150 msec. These translocation times were significantly higher than reported in the literature.

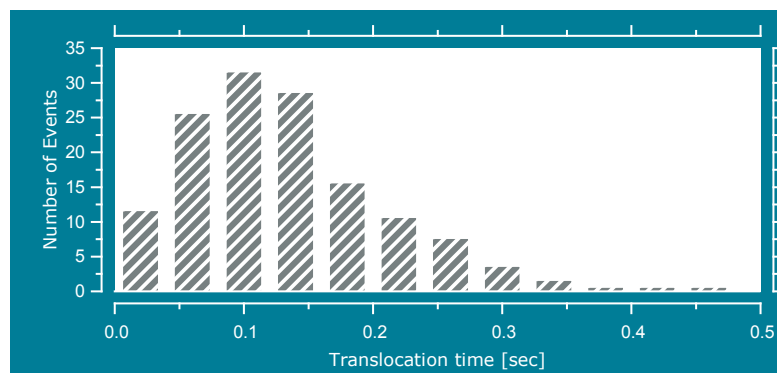


**FIGURE 4.34**

Histogram presenting the distribution of the recorded translocation time of each event.

The most probable translocation duration time lies between 50 and 150 msec at the low salt concentration of 50 mM KCL.

For instance, Meller et al. found most probable translocation times of 120 and 330  $\mu\text{sec}$  for ssDNA poly(dC)<sub>100</sub> and poly(dA)<sub>100</sub> molecules, respectively<sup>[249]</sup>. A potential reason for the extended translocation time (or better named “*translocation duration/blockade time*”) was the possibility of single-stranded DNA fragments building secondary structures, through intramolecular base pairing the ssDNA forms a hairpin loop structure. According to the insertion of a small extending single-stranded part of the folded ssDNA fragment into the  $\alpha$ -hemolysin pore, the hairpin loop structure has to unzip before sliding completely through the biopore. Due to this change in conformation apparent higher and broader distributed translocation duration times were observed. The respective spatial orientation and loop length was responsible for strongly varying translocation times. Mathé and coworkers presented data<sup>3</sup> for unzipping events of hairpins structures during translocation of ssDNA with a blockade time of  $\sim 70$  msec<sup>[250]</sup>. The unzipping kinetics of a hairpin, while it is lodged in the pore, is influenced by the rivalry between the sliding process and the rezipping. Once a nucleotide is unzipped it can either slide along the pore channel (thus blocking the rezipping) or rejoin the hairpin<sup>[250]</sup>. Vercoutere et al. also discovered that the blockade time increases with increasing length of hairpin stems<sup>[22]</sup>. Further, they demonstrated the possibility to resolve single nucleotide or single base pair differences between otherwise identical DNA molecules forming hairpins<sup>[22]</sup>.

1 Compare Figure 45 in the thesis of Dr. André Spiering<sup>[130]</sup>.

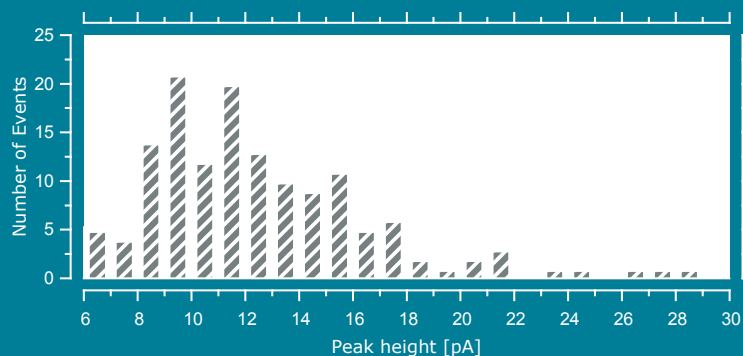
2 The peaks of this histogram (and of the following) are analyzed using a LabView program of Dr. Lukas Bogunovic based on an event-fitting algorithm.

3 The experimental parameters (e.g. applied voltage and buffer concentration) differ from the conditions of the above described experiments (for more details see the material section of the respective paper). Nevertheless, the principle impact of a hairpin structures on the translocation process should be not affected.

It is also interesting to note that the ionic current change of translocation events increased during translocation. Even though this behavior is already known for NPs with much larger diameters<sup>[130]</sup>, it was not expected to occur with  $\alpha$ -hemolysin pores. Smeets et al. published in 2006 that the reason for an increasing current signal during translocation of DNA fragments through solid-state NPs is the low salt concentration<sup>[251]</sup>. To verify if the sign of the current change using  $\alpha$ -hemolysin pores really depended on the salinity of the solution, a control experiment with a high salt concentration but otherwise same conditions was performed. A detailed description about the source of current change is given in the next section.

**FIGURE 4.35**

Histogram illustrating the distribution of recorded peak heights. The most probable peak height for this experiment lies between 9 - 11  $\mu\text{A}$  at the low salt concentration of 50  $\text{mM}$  KCL.



Due to the small number of recorded translocation events, the distribution of the peak height is not highly representative. Nevertheless, the data suggest that the most probable peak height for this experiment lies between 9 - 11  $\mu\text{A}$  (see Figure 4.35).

### Experiments at high salt concentrations

As noted above this experiment was also executed at a high salt concentration (2 M KCL). Figure 4.36 shows the GUV rupture and sealing process. Again, the ionic current signal was very stable with low noise and was linearly dependent on the applied voltage. The NP appeared to be properly sealed and exhibited an electric resistance of nearly 0.8 G $\Omega$ .

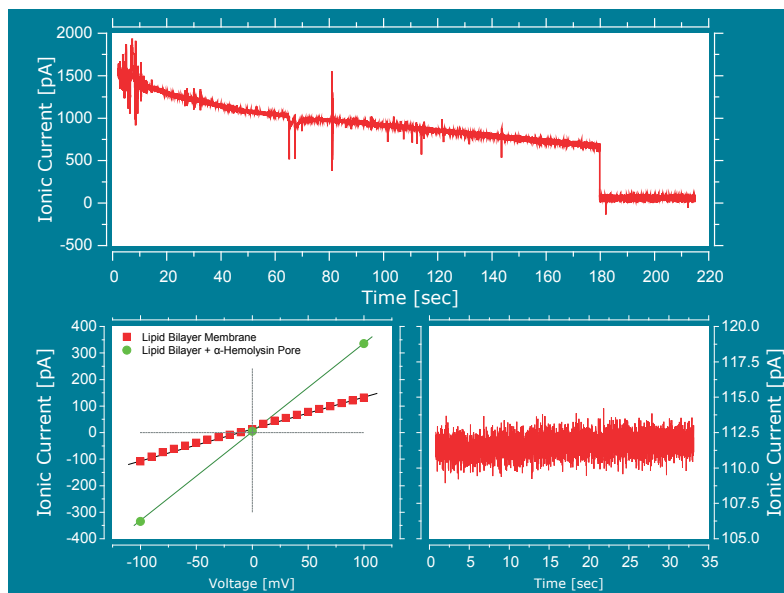


**FIGURE 4.36**

Upper diagram: Ionic current versus time while a GUV burst and sealed the NP. The IU-curve on the bottom left exhibits linear dependency. The ionic current signal was stable and with low noise.

[Parameters: Lipid mixture: DOPC:DOPG:Rhod-DOPE (99:0.995:0.005 mol%); sucrose concentration: 300 mM; applied Voltage: 100mV; buffer: 1 M KCL and 2 mM Tris/HCL at pH 8]

After the addition of freshly prepared  $\alpha$ -hemolysin (applied voltage 100 mV), several distinct steps in the ionic current signal were observed (see left diagram in Figure 4.37). The IU-curve for the lipid bilayer membrane with incorporated  $\alpha$ -hemolysin pores showed a linear dependence. The height of the ionic current compared to the previous performed experiment with low salt concentration is noteworthy.

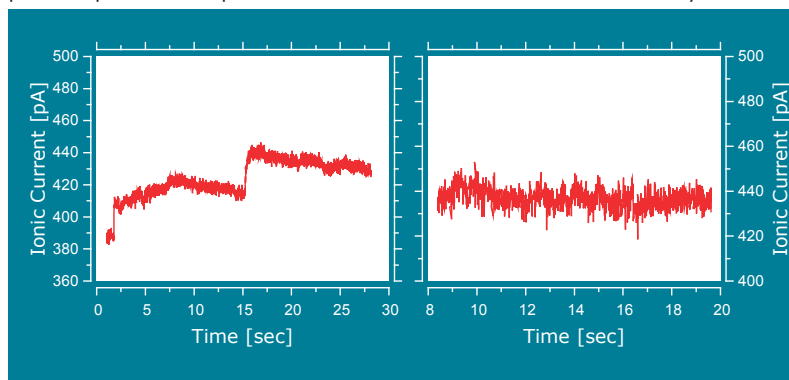


**FIGURE 4.37**

The left diagram shows discrete steps in the current signal during incorporation of single  $\alpha$ -hemolysins. After integration of (probable) four biopores the ionic current is stable (right diagram).

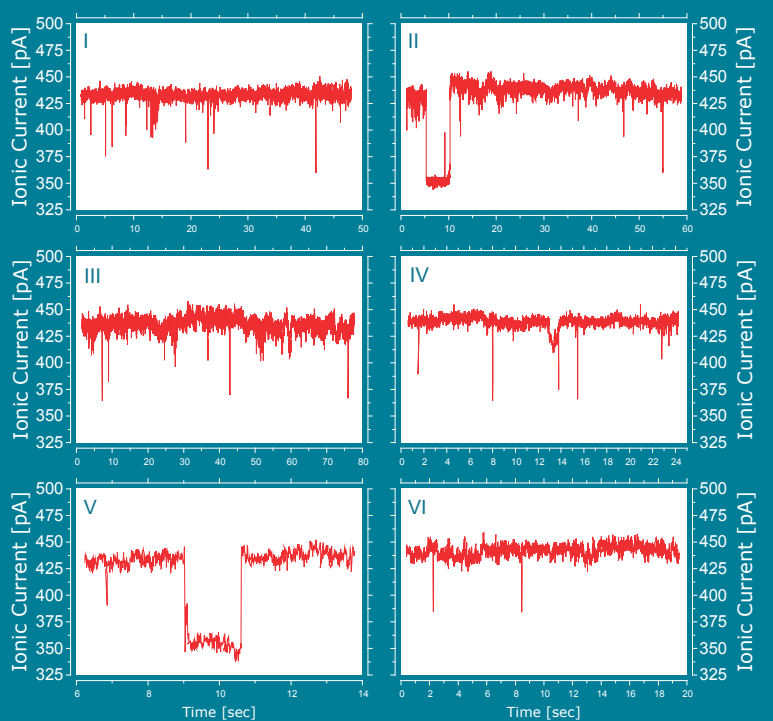
[Parameters: Lipid mixture: DOPC:DOPG:Rhod-DOPE (99:0.995:0.005 mol%); sucrose concentration: 300 mM; applied Voltage: 100 mV; buffer: 1 mM KCL and 2 mM Tris/HCL at pH 8]

Even though the currently used 1 M KCL concentration is 20 times larger (compared to 50 mM), the ionic current signal (with integrated biopores) only increased by 40% (compare Figure 4.31 IV and Figure 4.37 right). In this context, one has to act with caution given the experimental parameters that were applied. Taking into account the

differences in the applied voltage and the probable number of incorporated biopores, the variation caused only by the salinity revealed an increase by a factor of 2.5. This value is still less than expected. Other variations besides the controlled parameters might differ, such as the surface charge of the NP region.

Nevertheless, it was possible to perform free translocation experiments using the same type of ssDNA fragments as in the previous studies. In Figure 4.38 six examples are presented showing single translocation events. Few decreases in time intervals with a width of several seconds were recorded along with many short time drops (diagram II and V). These drops appear to be not caused by single ssDNA translocations. The probability that these events can be interpreted as an extraction event of  $\alpha$ -hemolysin molecules is not realistic because of the different step height. As such, these long lasting events are neglectable in the following analysis of the drop characteristics.

**FIGURE 4.38**  
Six diagrams presenting free translocation of single-stranded DNA fragments by the coulter counter method.  
[Parameters: Lipid mixture: DOPC:DOPG:Rhod-DOPE (99:0.995:0.005 mol%); GUV sucrose concentration: 300 mM; applied Voltage: 100 mV; buffer: 1 M KCL and 2 mM Tris/HCL at pH 8]



The histogram in Figure 4.39 illustrates that the translocation time with the most recorded number of events lies between 16 msec and 100 msec. There was also a small number of drops with a translocation duration time of more than 1 sec, but the events shorter than 200 msec dominated.

Altogether these translocation times were clearly shorter than the ones observed at low salinity, but higher than the reported values in the literature. This finding suggests that the previously described hairpin loop structure seem to assist the longer blockade times because of the required time for unzipping. Proving that the observed

translocation events are definitely caused by DNA molecules, we rinsed the DNA containing solution after a successful experiment twice with fresh buffer. After this washing step no further translocation events could be monitored. This procedure was also performed in subsequent experiments at low salt concentration, leading to the same result.

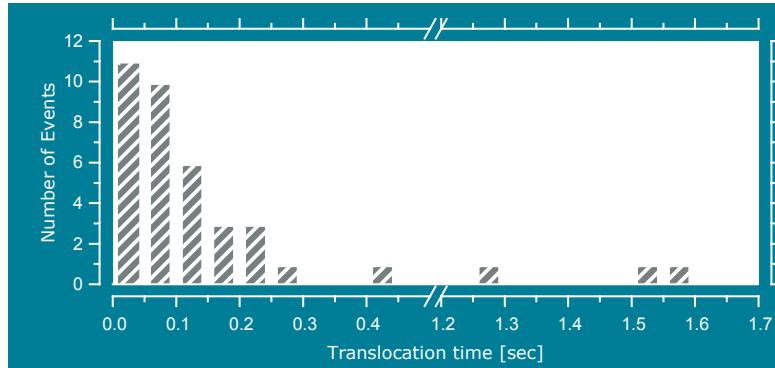


**FIGURE 4.39**

Histogram presenting the distribution of the recorded translocation time of each event (except the long lasting ones). The most probable translocation duration time lies between 50 and 150 msec at the high salt concentration of 2 mM KCL.

In contrast to the translocation time, the sign of current change occurred as expected. At this high salinity with 1 MKCL the current change appeared as a drop in the signal, as was also observed for silicon-nitride NPs at this concentration. The distribution of the recorded drop depths in Figure 4.40 is once again not highly representative and even broader than for the previous experiment. Therefore, it is not possible to point out a most probable drop depth, whilst more data is not available.

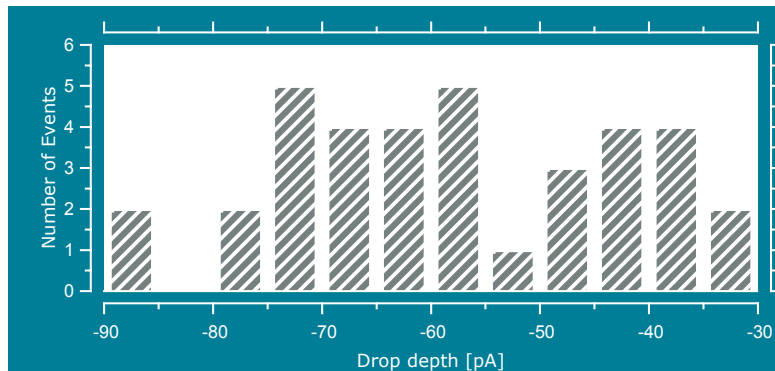


**FIGURE 4.40**

Histogram illustrating the distribution of recorded peak heights at the high salt concentration of 2 mM KCL.

Nevertheless, these results verify that the sign of current change using  $\alpha$ -hemolysin pores really depended on the salinity of the solution. Smeets et al. published in 2006 that the nanopore conductance is affected by surface charges in the pore region<sup>[251]</sup>. The charge carriers in the solution should dominate the ionic current using a buffer with high salt concentrations (e.g. 1 MKCL). Hence, the nanopore conductance scales linearly with the amount of charge carriers. Furthermore, mobile ions ( $K^+$  counterions screening the negative surface charge of the silicon nitride nanopore) contribute to the overall ionic current. The number of these counterions depends also on the strength of the salt concentration<sup>[251]</sup>. Thus, the total ionic current through a nanopore is identical to the sum of the contributions of the ion bulk concentration in solution and the counterions shielding the surface charge. Adding an ssDNA molecule

to this calculation, one has to consider two competing effects. On the one hand, the conductance is reduced due to the volume that is occupied by the DNA molecule inside the NP. This means that introducing the DNA strand into the nanopore influences the bulk conductance by reducing the number of charge carriers which are available for ionic transport<sup>[251,252]</sup>. On the other hand, the charge of the DNA backbone is shielded by a cloud of mobile counterions, which increase the number of charge carriers available for ionic transport and provide a positive contribution to the total ionic current<sup>[253]</sup>.

With these pre-considerations the influence of the salt concentration on the current change during DNA translocation can be explained. At high salinity the ion bulk concentration dominates, so that the occupied volume by the DNA has a larger (negative) impact to total ionic current than the mobile cloud of counterions leading to current drops. Whereas at a low salinity the ions of the mobile cloud shielding the DNA have an (positive) impact leading to current peaks, because both the bulk concentration and the surface screening counterions are considerably decreased.

It would be interesting to repeat this experiment with the theoretically predicted<sup>[251]</sup> crossover point at a KCL concentration of approximately 370 mM. At this concentration no change in the current signal should be noticeable during DNA translocation events. The absence of this experiment, as well as the lack of further translocation observations (at high and low salt concentrations) are a result of unsuccessful  $\alpha$ -hemolysin incorporation. Over 15 experiments were performed leading to proper NP sealing by lipid bilayer membranes with low noise that were stable for hours, but no biopore incorporation could be observed. Testing different concentrations and new ordered batches of  $\alpha$ -hemolysin also did not succeed, nor did the application of different voltage driven protocols (as demonstrated e.g. by Renner et al.<sup>[254]</sup>).

Due to this situation it was also not feasible to use the above mentioned dsDNA fragments with an ssDNA overhang for performing controlled translocation experiments by OT.

Because of the high time and effort required to execute this method of bilayer formation, a third experimental method was demonstrated for generating faster and more reproducible lipid bilayer membranes without losing the ability of operating optical tweezers experiments. This method is described in the next chapter 4.2.3.

### 4.2.3 Ionovation Bilayer Slide

As described above, the desired method for generating freestanding lipid bilayer membranes should be fast and reproducible. For this reason, the commercial available Bilayer Slide (Ionovation GmbH, Germany) was considered<sup>1</sup>. A detailed overview of the Bilayer Slide structure is given in chapter 3.3.4. The principle of this device is illustrated step-by-step in Figure 4.41.

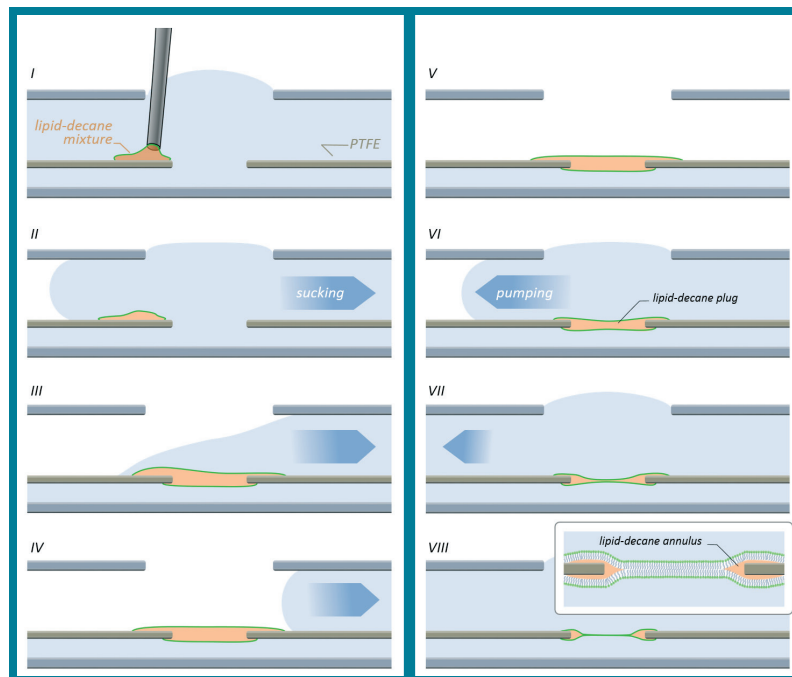


**FIGURE 4.41**  
Schematic sketch of the lipid bilayer generation procedure utilizing the “Ionovation Bilayer Slide”.

First a volume of  $0.2 \mu\text{l}$  was added next to the aperture on the PTFE foil (image I). Afterwards the buffer of the upper channel was removed and caused the formation of a lipid-decane plug within the aperture (image II to V). Back flushing of the buffer leads to initial plug thinning. Finally, a lipid bilayer membrane was formed spontaneously.

The device consists of two channels, which are separated by a  $12 \mu\text{m}$  thin PTFE (*polytetrafluoroethylene*, teflon) foil. The foil contains an oval aperture ( $50 \times 30 \mu\text{m}$ ) and is highly hydrophobic. The phospholipid (DPhPC) was solved in *n*-decane<sup>2</sup> and  $0.2 \mu\text{l}$  of this mixture was added manually near the aperture (sketch I). Prior to this procedure, both channels had to be filled with buffer solution without creating any microbubbles of air (which would hinder the free flow of the solution and ionic current measurements). Once the buffer solution was removed by sucking, the lipid-decane droplet is smeared across the PTFE foil and thus filled the aperture with a lipid-decane plug (see sketch II to V). As a result of back flushing the buffer into the upper channel, the lipid-decane plug was stabilized (sketch VI and VII) and the formation of a lipid bilayer membrane surrounded by an annulus (sketch VIII) was observed. The thinning process has been reported to occur spontaneously and within several minutes<sup>[255]</sup>. As soon as the lipid annulus was visible the lipid bilayer membrane was prepared for  $\alpha$ -hemolysin incorporation attempts.

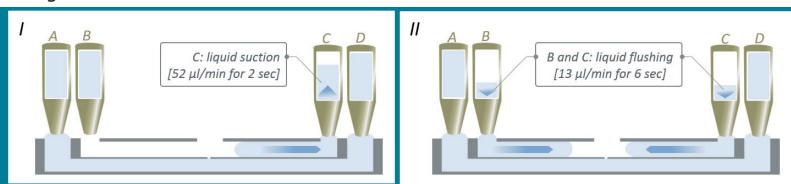
<sup>1</sup> First instructions regarding the Ionovation technology were conducted at the III. Institute of Physics (Jörg Enderlein Laboratory), Georg-August-University Göttingen (Germany), with kind support by Jan Thiert.

<sup>2</sup> In the following text *n*-decane is shortened to decane.

For better observation and for studying the formation and thinning process, the fluorescence microscopy setup was used, before changing to the OT setup. As described in chapter 3.3.4 the Bilayer Slide was connected to a syringe pump system. Both syringes were utilized for suction and flushing, independently of one another, and each syringe was connected via a switchable valve with either tube connector A and B or C and D, respectively. The sucking and flushing velocities were found to be critical for bilayer formation. The volume of sucked liquid and the volume of back flushing liquid, respectively, were only predetermined by the channel dimensions and initial level of filling. The main parameters for the most successful lipid bilayer generation cycle are presented in the following schematic. In short, after suction of the buffer ( $52\ \mu\text{l}/\text{sec}$  for 2 sec) it appeared to be advantageous to flush back the extracted volume via both inlets B and C (each with  $13\ \mu\text{l}/\text{sec}$  for 4 sec). In addition to these two steps a break of 10 sec was added to the software controlled bilayer generation sequence. This sequence was repeated until a successfully formed lipid-solvent plug was observed. The cycle was only stopped during the break to ensure a complete filling of the channel.

**FIGURE 4.42**

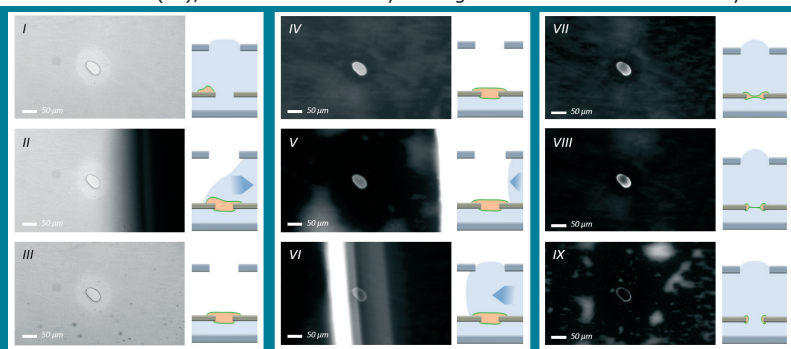
Schematic sketch visualizing the pump cycle parameters that led to the most successful lipid bilayer generation. More details are in the main text.



To get better insight in the bilayer formation process, Figure 4.43 combines micrographs and schematics of one of the earliest attempts. The first three images were obtained by transmitting light microscopy showing the suction of the buffer solution and leaving the lipid-decane plug within the aperture. The latter is only visible by fluorescence microscopy (IV). After flushing back the buffer (V - VII) thinning and bilayer formation was observed (VIII). In this experiment the bilayer broke shortly after formation (IX), which can be clearly distinguished from the thinned bilayer.

**FIGURE 4.43**

Micrographs showing the bilayer generation process, each step is visualized by a schematic. Images I to III are transmitting light micrographs and images IV to IX are fluorescent micrographs. The difference between an already thinned lipid bilayer (VIII) and a broken bilayer (IX) was clearly visible.



It was often observed that the formed plug broke before it was accurately thinned out. However, it was easy to start a new sequence, due to the connection to the syringe unit. In general three to five cycles were necessary to obtain a stable lipid bilayer membrane. Additional cycles were never successful when the lipid-decane plug formation step failed more than three times. Thus, a new lipid-decane droplet was added near the aperture after three failed attempts. This procedure could be

repeated up to five times before slide washing (with MiliQ®-water and isopropanol) was mandatory. Images *I* to *IV* in Figure 4.44 nicely demonstrate the plug forming step in more details as above. The lipid-decane droplet was forced by the solvent flow to smear over the PTFE foil and appeared as slightly shining clouds (*II* and *III*). A lipid-decane filled plug within the aperture occurred once this cloud has crossed the aperture (*IV*).

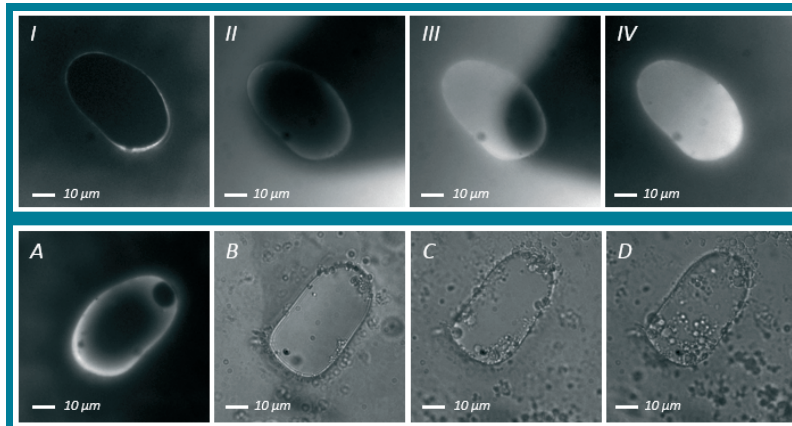


**FIGURE 4.44**

The aperture was flushed with lipid-decane mixture (*I* to *III*) resulting in a pore filled with a lipid-decane plug (*IV*). In some experiments the plug not only thinned out, but also bigger vesicles or air bubbles attached to it (*A*). It was very often observed that small vesicles were lying the plug and hindered the thinning (*B*, *C* and *D*).

[Parameters: Lipid mixture: DPhPC:Rhod-DOPE (99:1 vol%) 25 mg/ml in *n*-decane; buffer: 20 mM KCL and 2 mM Tris/HCL at pH 8]

A supplementary impression of frequently observed phenomena is given in the bottom row in Figure 4.44. Image *A* shows a thinned bilayer with a microbubble of air integrated to the annulus. Anytime this was observed the bilayer broke within the next several minutes. The small air bubble or vesicles visible in image *B*, *C* and *D* (frequently detected when more plug forming cycles were performed) had no such dramatic impact on the lipid bilayer lifetime, but appeared to hinder the thinning process.

#### **Bilayer thinning and lipid-solvent annulus appearance**

When a lipid-decane plug was successfully generated, the thinning process was observed over a long time. Figure 4.45 demonstrates a thinning that took about 45 min, resulting in a clearly visible annulus in the transmitting light micrograph (*V*).

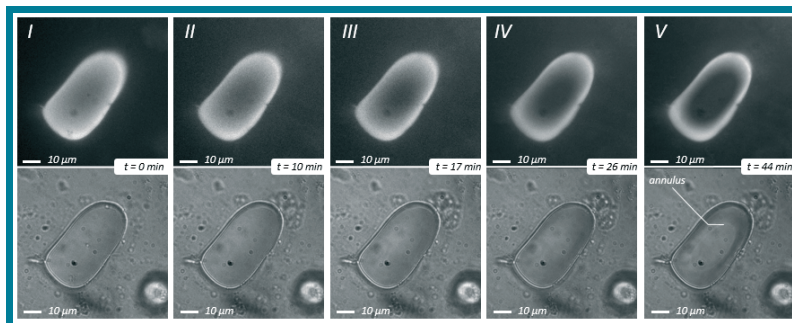


**FIGURE 4.45**

In this experiment the thinning took about 45 min until the initial lipid-decane plug (*I*) thinned out forming a stable lipid bilayer membrane (*V*). The annulus was observable by transmitting light microscopy.

[Parameters: Lipid mixture: DPhPC:Rhod-DOPE (99:1 vol%) 25 mg/ml in *n*-decane; buffer: 20 mM KCL and 2 mM Tris/HCL at pH 8]

The area of the formed lipid bilayer membrane appeared very dark in contrast to the surrounding lipid annulus when fluorescence microscopy was used. The lipid-solvent annulus features always a higher fluorescence intensity because the labeled

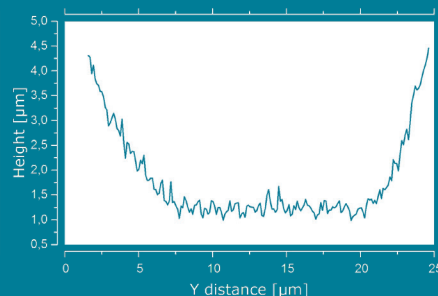
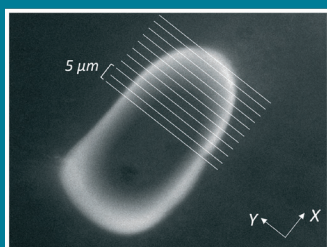
lipid molecules were not only subjected to the buffer-decane interface (as simplified pictured in the inset in image VIII of Figure 4.41), but were also distributed in the lipid-decane annulus itself. This bilayer was stable for several hours and did not break when the setup was changed. As demonstrated in Figure 4.45 the combination of fluorescence and transmitting light microscopy was important. Even though the transmitting light micrographs provided pictures with more information once the annulus was formed, the step by step thinning process was only observed using fluorescence microscopy. Thus, this combination was mandatory as long as the thinning time was not clearly reduced. A first approach to promote the thinning by creating a constant flow within the top or bottom channel or within both channels simultaneously had no significant influence. A further method to speed up this thinning process is presented later in this chapter.

To visualize the shape and curvature of the annulus the intensity gradient in image V (Figure 4.45) was analyzed. Twelve line plot profiles of the intensity are plotted indicated by the white lines in the micrograph (Figure 4.46).

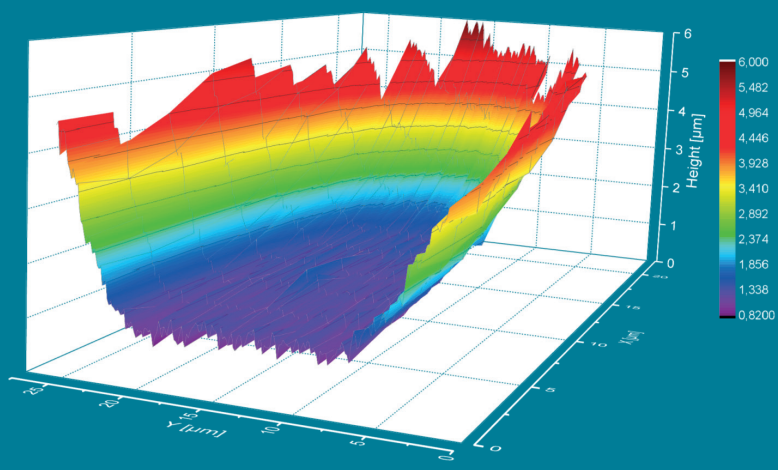
**FIGURE 4.46**

Fluorescence micrograph marked with white lines indicating the position of analyzed intensity line plot profiles.

One of these line plots is presented aside. The level of intensity (in arbitrary units) was converted into approximated height in  $\mu\text{m}$  (for more details see main text).



The 3D-plot resulted from combining 12 line plots together and it illustrates the annulus curvature and the flatness of the lipid bilayer membrane.



The obtained level of intensity in arbitrary units is then converted into approximated height in  $\mu\text{m}$ <sup>1</sup>. One exemplary single line plot is presented in Figure 4.46. The length of the bilayer area in the y-direction is estimated at approximately 12.5  $\mu\text{m}$  and in the

<sup>1</sup> The thickness of the PTFE foil was 12  $\mu\text{m}$  and the lipid bilayer membrane was supposed to be horizontally located in the middle of the PTFE sheet. It can be hypothesized that the distribution of the lipid molecules within the decane annulus was homogeneous and therefore, the intensity was directly connected to the height of the annulus. In this context the height of the dark area in the center of the aperture can be set as zero and the bright edge of the aperture as 6  $\mu\text{m}$  in height.

x-direction, ca.  $20\ \mu\text{m}$ . These measurements lead to a lipid bilayer membrane area of approximately  $196\ \mu\text{m}^2$ , which is 15 % of the total aperture area. The combination of the twelve line plots leads to an illustrating 3D-plot (bottom diagram in Figure 4.46). Even though the information about the dimensions in  $\mu\text{m}$  is an approximation, it provides a realistic impression of the annulus curvature and the flatness of the lipid bilayer membrane.

Figure 4.47 shows six more examples for successfully generated lipid bilayer membranes after long lasting thinning. The lifetime of the bilayer in image F was only about 30 sec from exhibiting the annulus to breakage. The instability was once again likely caused by the air bubbles within the annulus. However, the bilayer in image A was stable for hours, although small vesicles lay directly on top of the annulus edge. The half-moon like arrangement of the vesicles was caused by the curved shape of the annulus. The final size of the lipid bilayer (or annulus) area differed drastically from experiment to experiment (compare image C and D). Sometimes the bilayer area increased slightly with time, but usually the size remained stable compared to initial formation. Moreover, it was found that the presence or absence of a constant liquid flow in the upper or bottom channel had no varying influence on the size.

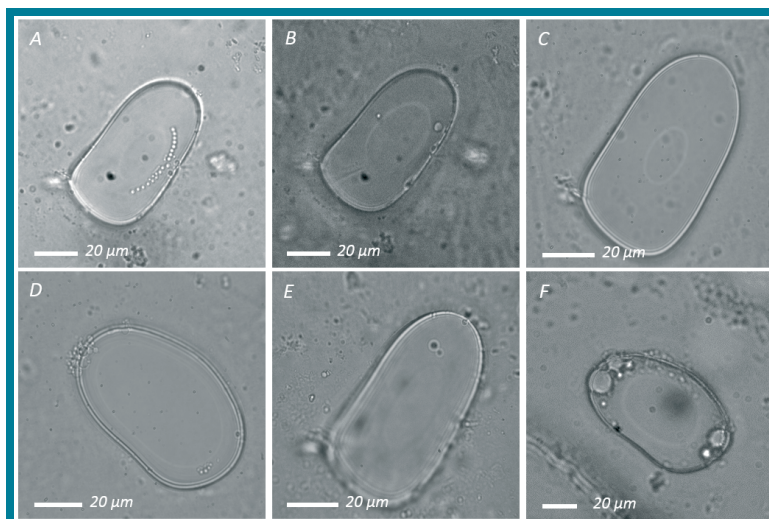


**FIGURE 4.47**

Six examples for successfully thinned lipid-decane plugs that formed a lipid bilayer membrane. In each image the annulus was visible.

[Parameters: Lipid mixture: DPhPC:Rhod-DOPE (99:1 vol%) 25 mg/ml in *n*-decane; buffer: 20 mM KCL and 2 mM Tris/HCL at pH 8]

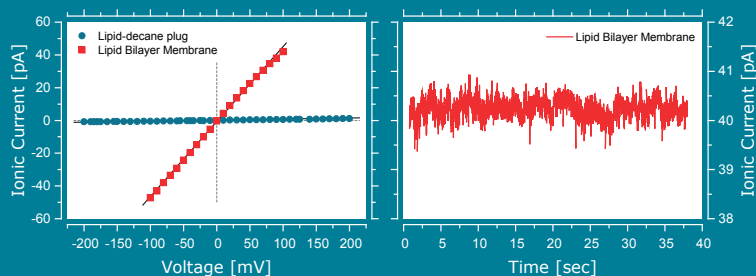
Once a stable lipid bilayer membrane was observed, an IU-curve was recorded (see left diagram in Figure 4.48). As before, the ionic current signal depended linearly on the applied voltage. The aperture was properly sealed and the electric resistance was determined to be  $2.4\ \text{G}\Omega$ . This value is comparable to obtained sealing resistances by GUV rupture experiments. Additionally, an IU-curve for a not-yet-thinned lipid-decane plug within the aperture is presented. In this example the resistance was estimated to be  $166\ \text{G}\Omega$ . The ionic current signal for a lipid bilayer membrane was also found to be stable over a long period of time and with low noise (see right diagram in Figure 4.48). As described in the methods section (3.3.4), the ionic current (as presented here) was much less noisy without allowing the tube connectors to be in contact with the Bilayer Slide reservoirs. For characterization of the lipid bilayer

membrane, the capacitance was measured additionally<sup>1</sup>. With this value the specific capacitance was calculated, which is defined as capacitance per unit area<sup>[256]</sup>. The specific capacitance indicates how much solvent is contained in a lipid bilayer membrane<sup>[256]</sup>. Due to non-ideal calibration of the LCR-meter the initial values obtained for the capacitance are unusable. Nevertheless, determining the specific capacitance will be an important tool and considerably improve the analysis of ongoing lipid bilayer studies.

**FIGURE 4.48**

The IU-curve for lipid-decane plug within the aperture and for a lipid bilayer membrane. The ionic current signal was stable and had low noise.

[Parameters: Lipid mixture: DPhPC:Rhod-DOPE (99:1 vol%) 25 mg/ml in *n*-decane; buffer: 20 mM KCL and 2 mM Tris/HCL at pH 8]



Subsequent to measuring the ionic current to applied voltage characteristics  $\alpha$ -hemolysin was added to the buffer solution. Again, no distinct steplike changes in the ionic current signal and thereby incorporation of a biopore could be observed. As for the GUv studies different buffer concentrations, new batches of  $\alpha$ -hemolysin and voltage driven protocols were unsuccessful.

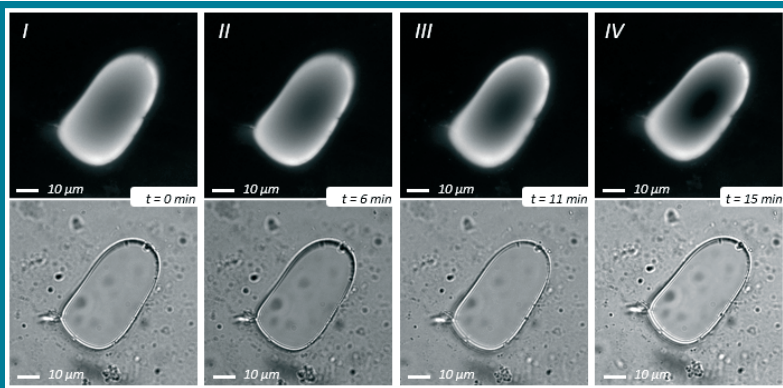
#### Enhancement of the thinning process

It was possible to enhance the thinning process by using a mixed solvent of *n*-decane and 1-hexanol. Osaki et al. demonstrated that mixing of 1-hexanol rapidly reduced the thickness of the lipid-solvent plug, and thus effectively promoted the thinning and the lipid bilayer formation process<sup>[73]</sup>. A further advantage using 1-hexanol as a solvent component was that the possibility for solvent molecules to remain within the lipid bilayer was reduced<sup>[73]</sup>. The optimal ratio of *n*-decane to 1-hexanol was found to be 3:2 (for this setup as well as for the Bilayer Slide). Figure 4.49 presents the observation that utilizes this solvent ratio.

**FIGURE 4.49**

Fluorescence and transmitting light micrographs showing the accelerated thinning process using a mixture of *n*-decane and 1-hexanol. The image E in Figure 4.47 with observable annulus was obtained 2 min after image IV in this figure.

[Parameters: Lipid mixture: DPhPC:Rhod-DOPE (99:1 vol%) 5 mg/ml in *n*-decane:1-hexanol (3:2 vol%); buffer: 20 mM KCL and 2 mM Tris/HCL at pH 8]



1 The LCR-meter was integrated in the setup within the last months of the experimental work. Thus, only a few measurements with simultaneously capacitance recordings were executed.

The thinning duration was 17 *min* until an annulus was observed (image *V* in Figure 4.47). This is more than twice as fast than without adding 1-hexanol to the solvent. Using an even higher ratio (e.g. 70 % 1-hexanol) led to an increasing probability for breakage (even before appropriate thinning). This behavior was independently discovered by Osaki et al., whereas they found the critical ratio to be 90 %, since n-decane cannot reinforce the lipid-solvent annulus<sup>[73]</sup>.

### Interesting phenomena

At the end of this chapter some interesting effects referring to the interplay between the lipid-solvent annulus and the OT laser focus are presented<sup>1</sup>. Varying the lipid composition to enhance the stability of the bilayer, a mixture with 0.5 vol% cholesterol was tested (apart from that the mixture was like the composition described in the caption to Figure 4.49). After a proper thinning and bilayer formation (see Figure 4.50 *I*), the setup was changed and some microbeads were added to the buffer solution to test the physical strength of the lipid bilayer membrane. Shortly afterwards, the membrane broke; this event is visible in image *II*. The appearance of the border between bilayer and annulus changed and it was possible to observe small vesicles or dirt particles moving through the aperture. The microbeads themselves could not be the cause of breakage, due to the fact that the beads reached the region of aperture noticeably after bilayer damage.

In all prior experiments the breakage of the bilayer was accompanied by a full disappearance of both the bilayer and the surrounding annulus, but in this case, the annulus persisted. In previous studies the OT trapping laser focus never had an observable influence on the stability and shape on the bilayer and the annulus. However, this persistent annulus could be deformed by the laser focus as it is visible in image *III* – *VI* of Figure 4.50.

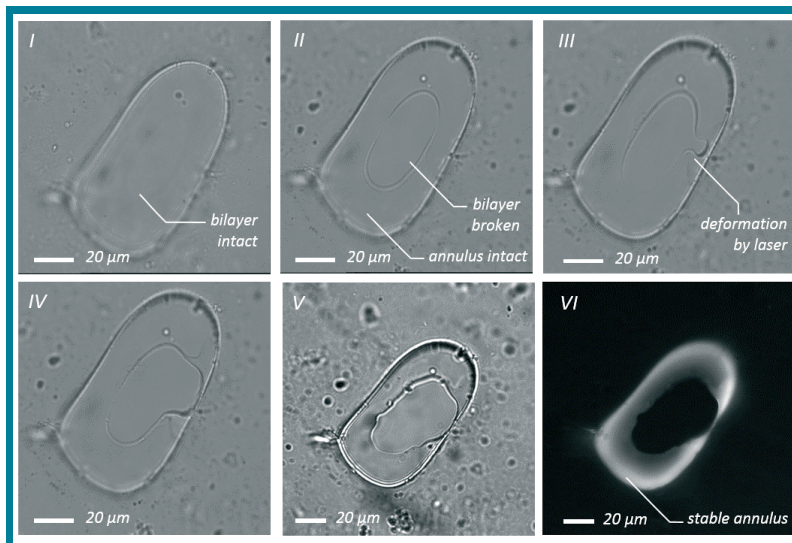


**FIGURE 4.50** Micrographs showing interesting effects after lipid bilayer breaking. According to the breaking of the bilayer (compare image *I* and *II*), a deformation of the remaining annulus induced by the laser focus was observed (image *II* to *VI*).

[Parameters: Lipid mixture: DPhPC:Rhod-DOPE:Chol (99:0.5:0.5 vol%) 5 mg/ml in n-decane:1-hexanol (3:2 vol%); buffer: 20 mM KCL and 2 mM Tris/HCL at pH 8]

<sup>1</sup> These experiments were performed under my supervision by Roland Hillmann, who will continue the ongoing experiments.

Once the laser focus lasted for some tens of seconds on the same spot of this annulus, this area seems to disappear and thereby increasing the annulus boundary. In Figure 4.50 V several disappeared areas can be identified. The fluorescence micrograph (image VI) also supports the hypothesis that the annulus still exhibited its former slightly curved shape, except for the disappeared areas, which have a distinct and sharp edge. This indicates that the annulus had no fluid character anymore, but seemed to be hardened. Whether or not this effect was caused by the additional cholesterol remains unclear because attempts with this mixture without any influence of the laser focus had been also performed.

As indicated by the last finding, there are still many compositions to be tested and perhaps this "*hardening effect*" will help to develop even more stable lipid bilayer membranes. Nevertheless, it could be demonstrated that this setup allows for swift and reproducible generation of freestanding lipid bilayer membranes. The main focus for the ongoing work will be to locate the reason why the incorporation of  $\alpha$ -hemolysin pores has, thus far, not been feasible.

## 5 Summary and Outlook

---

The study of NP-based systems covers a wide range of scientific research areas, however, the prospect of sequencing DNA by this technique is the most prominent one and the driving force for the key developments of the past few years. This has led to an intensified competition in order to push forward accurate, low-cost sequencing into clinical space. Accordingly, this NP-based technology has the capability to revolutionize basic research and clinical medicine (sequencing a diploid mammalian genome for  $\sim$  \$ 1 000 in about 24 h), as well as to enter new customer sectors, which need genetic fingerprinting for food safety, forensic science or agricultural biotechnology. The numerous experimental studies of DNA translocation events through NPs have progressively led to the question about the fundamental understanding of such a translocation process. The estimation of the involved threading force is of essential significance for the purpose of characterizing this mechanism. Integrating a NP into an optical tweezers system demonstrated the feasibility to control the position of a molecule with respect to the NP and to monitor the acting forces directly. However, an unambiguous theory of the hydrodynamic impact on the DNA translocation process remains to be achieved. This issue was addressed by the first experimental part of this thesis via investigation of NP surface modifications by means of lipid bilayer coatings and through subsequent characterization of the related effects on optical tweezers DNA threading force measurements. Besides this coating strategy, three different methods for generating freestanding NP-spanning and stable lipid bilayer membranes were examined in the second experimental part. These biological membranes should be suitable for both incorporation of biological pores like  $\alpha$ -hemolysin and subsequent optical tweezers force measurements.

In the first experimental part, optical tweezers with video-based image analysis were utilized to study and compare threading forces acting on a single dsDNA molecule situated inside a bare silicon nitride NP, as well as inside a lipid bilayer-coated solid-state NP. Inspired by the work of Yusko et al., a fabrication protocol for the coating process of the NP containing microchips (by means of small unilamellar vesicles) was developed and established, leading to a successful and reproducible modification protocol of an unmodified silicon-nitride surface. The presence of such a lipid bilayer coating has been confirmed by fluorescence microscopy and by comparing the varying ionic currents, whether the chip was coated or not. This is feasible because a lipid bilayer does not only alter e.g. the surface charge density, but it also causes a decay of the NP diameter by twice the thickness of a single bilayer. The changes in the ionic current signal were found to be very sensitive and accurate, thus allowing for the estimation of the reduced NP diameter, which is a strong indicator for the quality of the bilayer coating within the pore. Besides the coating, the general dependence of the NP diameter on the measurable value of the threading force was also studied for both coated and uncoated NPs. In general, a strong increase in the threading force upon decreasing the diameter of the bare NPs was observed, which can be attributed to a significant reduction of the EOF. Interestingly, after coating the NP walls with an electrically neutral lipid bilayer the recorded threading forces increased by 80 % (on

average). This increase could only partially be attributed to the reduction of the NP diameter due to the coating, since such a variation in NP size ( $\sim 10$  nm smaller diameter) would only account for a small increase of the measured force. Therefore, it can be proposed that the enhanced forces originate from a substantial reduction of the EOF through the NP. In order to describe these experimental results, an electrohydrodynamic theory was introduced (in close cooperation with the *Condensed Matter Theory Group* at Bielefeld University), which adopts Poisson, Nernst-Planck, and Stokes equations. In this context, the effects of reasonable modifications to the model, as well as varying surface charge and slip effects were discussed. It was discovered that the incorporation of a hydrodynamic slip length of  $l_{\text{slip}} = 0.5$  nm on the DNA surface sufficiently describes the examined threading forces for lipid bilayer coated as well as untreated NPs. This finding is a considerable indication that the surface nanostructure of the DNA (hydrophobic grooves and hydrophilic phosphate groups) has to be considered to gain a deeper understanding of the polyelectrolytes dynamics in such a highly confined environment of a NP and may be a part of the puzzle of an unambiguous electrohydrodynamic theory in the future. Beside the relevance for the theoretic model, it was found, that the use of a lipid bilayer-coating additionally prevents NPs from clogging and minimizes non-specific binding effects, which present a noticeable improvement of the experimental process.

The second project covers three different techniques, which have the common aim to generate freestanding lipid bilayer membranes. In the first instance the Langmuir-Blodgett technique was utilized to transfer a lipid monolayer simultaneously on both sides of a pore-containing solid-state membrane, forming a lipid bilayer within the pore region. Even though, the first experiments were promising, a truthful formation of such a bilayer could not be obtained. Different strategies for avoiding the disturbing air bubble within the window area of the chip by changing the dipping angle or by altering the surface modification of the membrane, led to no significant enhancements.

The second explored technique involved the production of giant unilamellar vesicles (GUVs) and their application to create a pore-spanning bilayer, by bursting the GUVs on the membrane surface. An efficient fabrication protocol was developed, leading to a reproducible (and fine-tunable) generation of GUVs, as well as repeatable observation of bursting events. Using the determined optimal lipid composition, filling properties and surface modifications, the sealing of the NP by GUV adsorption and rupture could be monitored and simultaneously verified by fluorescence video microscopy and ionic current analysis. The distribution of the measured resistances across the NP ranged from  $0.2$  G $\Omega$  to  $5.5$  G $\Omega$  (with a mean resistance of  $2.2$  G $\Omega$ ) and were shown to be independent of the diameter of the sealed solid-state NP and the used buffer concentration. Once a stable bilayer was achieved, the incorporation of the pore-forming protein  $\alpha$ -hemolysin could be demonstrated. The embedding of a single protein pore was recorded by a stepwise increase of the ionic current signal at comparatively low noise background. Starting with the translocation of single-stranded DNA oligomers at varying experimental conditions, the dependence of the buffer's salinity on the sign of the current change (either peaks or drops) was studied, confirming the results by Smeets et al. Measurements on this biopore-system with optical

tweezers could not be executed, due to later occurring problems concerning the incorporation of  $\alpha$ -hemolysin. Nevertheless, it was also demonstrated that a breakage of a freestanding bilayer (generated by GUVs) is not always unfavorable, but can lead to the formation of a lipid bilayer coating, similar to those generated by SUVs.

Finally, the commercially available *Bilayer Slide* was integrated into the existing setup, which was extended by a syringe pump system. According to the establishment of a working routine for a swift and reproducible formation of a freestanding lipid bilayer the incorporation of  $\alpha$ -hemolysin was tested. Unfortunately, this gap-filling step towards optical tweezers force measurements on a biological pore system remains open. However, this strategy as well as the GUV bursting technique still bears the potential to succeed in generating the first reported threading force measurements by OT on a biopore, once the issue of proper  $\alpha$ -hemolysin incorporation is solved sufficiently.

In conclusion, the experimental results presented in this thesis have expanded upon the force measurements in solid-state NPs to include the surface modification by a lipid bilayer coating, which results in higher recordable DNA threading forces, and thus leads to a more comprehensive theoretical description of polyelectrolyte dynamics in NPs. In addition, a fundament of preparation techniques was explored and established for future OT single-molecule threading force measurements by means of biological NPs, such as  $\alpha$ -hemolysin. Due to the lack of success within such an experiment, the involved forces for translocation through a biopore (with its highly charged interior) still remain unknown and thus, hold the key for future insights.

It will be interesting to see how this field of research progresses in the coming years, both, in fundamental science and sequencing applications, where NPs provide versatile properties as single-molecule sensors for polynucleotides, as well as for proteins.

# Bibliography

---

- [1] B. ALBERTS: *Molecular biology of the cell*, 4th ed (Garland, New York, 2002).
- [2] E. PETTERSSON, J. LUNDEBERG AND A. AHMADIAN: *Generations of sequencing technologies*, *Genomics* **93** (2): 105–111 (2009).
- [3] J. VENTER, K. REMINGTON, J. HEIDELBERG, A. HALPERN, D. RUSCH, J. EISEN, D. WU, I. PAULSEN, K. NELSON, W. NELSON, D. FOUTS, S. LEVY, A. KNAP, M. LOMAS, K. NEALSON, O. WHITE, J. PETERSON, J. HOFFMAN, R. PARSONS, H. BADEN-TILLSON, C. PFANNKOCH, Y.-H. ROGERS AND H. SMITH: *Environmental genome shotgun sequencing of the Sargasso Sea*, *Science* **304** (5667): 66–74 (2004).
- [4] S. YOUSEPH, G. SUTTON, D. RUSCH, A. HALPERN, S. WILLIAMSON, K. REMINGTON, J. EISEN, K. HEIDELBERG, G. MANNING, W. LI, L. JAROSZEWSKI, P. CIEPLAK, C. MILLER, H. LI, S. MASHIYAMA, M. JOACHIMIAK, C. VAN BELLE, J.-M. CHANDONIA, D. SOERGEL, Y. ZHAI, K. NATARAJAN, S. LEE, B. RAPHAEL, V. BAFNA, R. FRIEDMAN, S. BRENNER, A. GODZIK, D. EISENBERG, J. DIXON, S. TAYLOR, R. STRAUSBERG, M. FRAZIER AND J. VENTER: *The Sorcerer II Global Ocean Sampling expedition: expanding the universe of protein families*, *PLoS biology* **5** (3): e16 (2007).
- [5] L. STEINBOCK AND A. RADENOVIC: *The emergence of nanopores in next-generation sequencing*, *Nanotechnology* **26** (7): 74003 (2015).
- [6] F. SANGER, S. NICKLEN AND A. COULSON: *DNA sequencing with chain-terminating inhibitors*, *Proceedings of the National Academy of Sciences of the United States of America* **74** (12): 5463–5467 (1977).
- [7] P. NYRÉN: *The history of pyrosequencing*, *Methods in molecular biology* **373**: 1–14 (2007).
- [8] A. UNDERWOOD, T. DALLMAN, N. THOMSON, M. WILLIAMS, K. HARKER, N. PERRY, B. ADAK, G. WILLSHAW, T. CHEASTY, J. GREEN, G. DOUGAN, J. PARKHILL AND J. WAIN: *Public health value of next-generation DNA sequencing of enterohemorrhagic Escherichia coli isolates from an outbreak*, *Journal of clinical microbiology* **51** (1): 232–237 (2013).
- [9] G. SCHNEIDER AND C. DEKKER: *DNA sequencing with nanopores*, *Nature Biotechnology* **30** (4): 326–328 (2012).
- [10] D. DEAMER AND M. AKESON: *Nanopores and nucleic acids: prospects for ultrarapid sequencing*, *Trends in biotechnology* **18** (4): 147–151 (2000).
- [11] D. BRANTON, D. DEAMER, A. MARZIALI, H. BAYLEY, S. BENNER, T. BUTLER, M. DI VENTRA, S. GARAJ, A. HIBBS, X. HUANG, S. JOVANOVICH, P. KRSTIC, S. LINDSAY, X. LING, C. MASTRANGELO, A. MELLER, J. OLIVER, Y. PERSHIN, J. RAMSEY, R. RIEHN, G. SONI, V. TABARD-COSSA, M. WANUNU, M. WIGGIN AND J. SCHLOSS: *The potential and challenges of nanopore sequencing*, *Nature Biotechnology* **26** (10): 1146–1153 (2008).
- [12] P. ASHTON, S. NAIR, T. DALLMAN, S. RUBINO, W. RABSCH, S. MWAIGWISYA, J. WAIN AND J. O'GRADY: *MinION nanopore sequencing identifies the position and structure of a bacterial antibiotic resistance island*, *Nature Biotechnology* **33** (3): 296–300 (2015).
- [13] C. DEKKER: *Solid-state nanopores*, *Nature Nanotechnology* **2** (4): 209–215 (2007).
- [14] M. WANUNU: *Nanopores: A journey towards DNA sequencing*, *Physics of life reviews* **9** (2): 125–158 (2012).
- [15] D. ANSELMETTI: *Nanopores: Tiny holes with great promise*, *Nature Nanotechnology* **7** (2): 81–82 (2012).
- [16] D. ANSELMETTI AND A. GÖLZHÄUSER: *Converting molecular monolayers into functional membranes*, *Angewandte Chemie* **53** (46): 12300–12302 (2014).
- [17] O. BRAHA, B. WALKER, S. CHELEY, J. KASIANOWICZ, L. SONG, J. GOUAUX AND H. BAYLEY: *Designed protein pores as components for biosensors*, *Chemistry & Biology* **4** (7): 497–505 (1997).

- [18] J. KASIANOWICZ, E. BRANDIN, D. BRANTON AND D. DEAMER: *Characterization of individual polynucleotide molecules using a membrane channel*, Proceedings of the National Academy of Sciences of the United States of America **93** (24): 13770–13773 (1996).
- [19] L. MOVILEANU, S. CHELEY AND H. BAYLEY: *Partitioning of individual flexible polymers into a nanoscopic protein pore*, Biophysical Journal **85** (2): 897–910 (2003).
- [20] M. AKESON, D. BRANTON, J. KASIANOWICZ, E. BRANDIN, AND D. DEAMER: *Microsecond time-scale discrimination among polycytidylic acid, polyadenylic acid, and polyuridylic acid as homopolymers or as segments within single RNA molecules*, Biophysical Journal **77** (6): 3227–3233 (1999).
- [21] J. KASIANOWICZ, S. HENRICKSON, H. WEETALL AND B. ROBERTSON: *Simultaneous multianalyte detection with a nanometer-scale pore*, Analytical Chemistry **73** (10): 2268–2272 (2001).
- [22] W. VERCOUTERE, S. WINTERS-HILT, H. OLSEN, D. DEAMER, D. HAUSSLER AND M. AKESON: *Rapid discrimination among individual DNA hairpin molecules at single-nucleotide resolution using an ion channel*, Nature Biotechnology **19** (3): 248–252 (2001).
- [23] A. MELLER, L. NIVON AND D. BRANTON: *Voltage-Driven DNA Translocations through a Nanopore*, Physical Review Letters **86** (15): 3435–3438 (2001).
- [24] S. HENRICKSON, M. MISAKIAN, B. ROBERTSON AND J. KASIANOWICZ: *Driven DNA transport into an asymmetric nanometer-scale pore*, Physical Review Letters **85** (14): 3057–3060 (2000).
- [25] S. HOWORKA, S. CHELEY AND H. BAYLEY: *Sequence-specific detection of individual DNA strands using engineered nanopores*, Nature Biotechnology **19** (7): 636–639 (2001).
- [26] N. BELL AND U. KEYSER: *Nanopores formed by DNA origami: a review*, FEBS Letters **588** (19): 3564–3570 (2014).
- [27] S. HERNÁNDEZ-AINSA AND U. KEYSER: *DNA origami nanopores: developments, challenges and perspectives*, Nanoscale **6** (23): 14121–14132 (2014).
- [28] J. BURNS, N. AL-JUFFALI, S. JANES AND S. HOWORKA: *Membrane-spanning DNA nanopores with cytotoxic effect*, Angewandte Chemie **53** (46): 12466–12470 (2014).
- [29] A. MELLER, L. NIVON AND D. BRANTON: *Voltage-driven DNA translocations through a nanopore*, Physical Review Letters **86** (15): 3435–3438 (2001).
- [30] N. ASHKENASY, J. SÁNCHEZ-QUESADA, H. BAYLEY AND M. GHADIRI: *Recognizing a single base in an individual DNA strand: a step toward DNA sequencing in nanopores*, Angewandte Chemie **44** (9): 1401–1404 (2005).
- [31] D. STODDART, A. HERON, E. MIKHAILOVA, G. MAGLIA AND H. BAYLEY: *Single-nucleotide discrimination in immobilized DNA oligonucleotides with a biological nanopore*, Proceedings of the National Academy of Sciences of the United States of America **106** (19): 7702–7707 (2009).
- [32] Y. HE, M. TSUTSUI, R. SCHEICHER, F. BAI, M. TANIGUCHI AND T. KAWAI: *Thermophoretic manipulation of DNA translocation through nanopores*, ACS Nano **7** (1): 538–546 (2013).
- [33] K. LIEBERMAN, G. CHERF, M. DOODY, F. OLASAGASTI, Y. KOLODDI AND M. AKESON: *Processive replication of single DNA molecules in a nanopore catalyzed by phi29 DNA polymerase*, Journal of the American Chemical Society **132** (50): 17961–17972 (2010).
- [34] G. CHERF, K. LIEBERMAN, H. RASHID, C. LAM, K. KARPLUS AND M. AKESON: *Automated forward and reverse ratcheting of DNA in a nanopore at 5-Å precision*, Nature Biotechnology **30** (4): 344–348 (2012).
- [35] E. MANRAO, I. DERRINGTON, A. LASZLO, K. LANGFORD, M. HOPPER, N. GILLGREN, M. PAVLENOK, M. NIEDERWEIS AND J. GUNDLACH: *Reading DNA at single-nucleotide resolution with a mutant MspA nanopore and phi29 DNA polymerase*, Nature Biotechnology **30** (4): 349–353 (2012).
- [36] M. EISENSTEIN: *Oxford Nanopore announcement sets sequencing sector abuzz*, Nature Biotechnology **30** (4): 295–296 (2012).

- [37] L. STEINBOCK, O. OTTO, C. CHIMEREL, J. GORNALL AND U. KEYSER: *Detecting DNA Folding with Nanocapillaries*, Nano Letters **10** (7): 2493–2497 (2010).
- [38] R. AMMAR, T. PATON, D. TORTI, A. SHLIEN AND G. BADER: *Long read nanopore sequencing for detection of HLA and CYP2D6 variants and haplotypes*, F1000Research **4** (17): 1–15 (2015).
- [39] T. GILBOA AND A. MELLER: *Optical sensing and analyte manipulation in solid-state nanopores*, The Analyst (DOI: 10.1039/C4AN02388A) (2015).
- [40] L. STEINBOCK, O. OTTO, D. SKARSTAM, S. JAHN, C. CHIMEREL, J. GORNALL AND U. KEYSER: *Probing DNA with micro- and nanocapillaries and optical tweezers*, Journal of Physics. Condensed Matter **22** (45): 454113 (2010).
- [41] R. BULUSHEV, L. STEINBOCK, S. KHLYBOV, J. STEINBOCK, U. KEYSER AND A. RADENOVIC: *Measurement of the position-dependent electrophoretic force on DNA in a glass nanocapillary*, Nano Letters **14** (11): 6606–6613 (2014).
- [42] T. GUTSMANN, T. HEIMBURG, U. KEYSER, K. MAHENDRAN AND M. WINTERHALTER: *Protein reconstitution into freestanding planar lipid membranes for electrophysiological characterization*, Nature Protocols **10** (1): 188–198 (2015).
- [43] G. SCHNEIDER, V. CALADO, H. ZANDBERGEN, M. K. VANDERSYPEN AND C. DEKKER: *Wedging Transfer of Nanostructures*, Nano Letters **10** (5): 1912–1916 (2010).
- [44] S. GARAJ, W. HUBBARD, A. REINA, J. KONG, D. BRANTON AND J. A. GOLOVCHENKO: *Graphene as a sub-nanometre trans-electrode membrane*, Nature **467** (7312): 190–193 (2010).
- [45] H. W. C. POSTMA: *Rapid sequencing of individual DNA molecules in graphene nanogaps*, Nano Letters **10** (2): 420–425 (2010).
- [46] U. KEYSER, B. KOELEMAN, S. VAN DORP, D. KRAPP, SMEETS, RALPH M. M., S. LEMAY, N. DEKKER AND C. DEKKER: *Direct force measurements on DNA in a solid-state nanopore*, Nature Physics **2** (7): 473–477 (2006).
- [47] S. VAN DORP, U. KEYSER, N. DEKKER, C. DEKKER AND S. LEMAY: *Origin of the electrophoretic force on DNA in solid-state nanopores*, Nature Physics **5** (5): 347–351 (2009).
- [48] M. VAN DEN HOUT, I. VILFAN, S. HAGE AND N. DEKKER: *Direct force measurements on double-stranded RNA in solid-state nanopores*, Nano Letters **10** (2): 701–707 (2010).
- [49] A. SPIERING, S. GETFERT, A. SISCHKA, P. REIMANN AND D. ANSELMETTI: *Nanopore Translocation Dynamics of a Single DNA-Bound Protein*, Nano Letters **11** (7): 2978–2982 (2011).
- [50] B. LUAN AND A. AKSIMENTIEV: *Control and reversal of the electrophoretic force on DNA in a charged nanopore*, Journal of Physics. Condensed Matter **22** (45): 454123 (2010).
- [51] E. YUSKO, J. JOHNSON, S. MAJD, P. PRANGKIO, R. ROLLINGS, J. LI, J. YANG AND M. MAYER: *Controlling protein translocation through nanopores with bio-inspired fluid walls*, Nature Nanotechnology **6** (4): 253–260 (2011).
- [52] H. LODISH AND C. LANGE: *Molekulare Zellbiologie*, 4. Aufl (Spektrum, Akad. Verl., Heidelberg, 2001).
- [53] E. PENNISI: *Genomics. DNA study forces rethink of what it means to be a gene*, Science **316** (5831): 1556–1557 (2007).
- [54] H. PEARSON: *Genetics: what is a gene?*, Nature **441** (7092): 398–401 (2006).
- [55] F. MIESCHER: *Über die chemische Zusammensetzung der Eiterzellen*, Medizinisch-chemische Untersuchungen **4**: 441–460 (1871).
- [56] R. DAHM: *Discovering DNA: Friedrich Miescher and the early years of nucleic acid research*, Human genetics **122** (6): 565–581 (2008).
- [57] J. WATSON AND F. CRICK: *Molecular Structure of Nucleic Acids: A Structure for Deoxyribose Nucleic Acid*, Nature **171** (4356): 737–738 (1953).

- [58] A. GHOSH AND M. BANSAL: *A glossary of DNA structures from A to Z*, Acta Crystallographica Section D Biological Crystallography **59** (4): 620–626 (2003).
- [59] P. YAKOVCHUK, E. PROTOZANOVA AND M. FRANK-KAMENETSKII: *Base-stacking and base-pairing contributions into thermal stability of the DNA double helix*, Nucleic Acids Research **34** (2): 564–574 (2006).
- [60] M. MANDELKERN, J. ELIAS, D. EDEN AND D. CROTHERS: *The dimensions of DNA in solution*, Journal of Molecular Biology **152** (1): 153–161 (1981).
- [61] R. WING, H. DREW, T. TAKANO, C. BROKA, S. TANAKA, K. ITAKURA AND R. DICKERSON: *Crystal structure analysis of a complete turn of B-DNA*, Nature **287** (5784): 755–758 (1980).
- [62] F. CRICK, L. BARNETT, S. BRENNER AND R. WATTS-TOBIN: *General nature of the genetic code for proteins*, Nature **192**: 1227–1232 (1961).
- [63] C. CALLADINE AND J. WISSMANN: *DNA. Das Molekül und seine Funktionsweise*, 3. Aufl (Elsevier, Spektrum Akad. Verl., München, 2006).
- [64] B. FUTCHER, G. LATTER, P. MONARDO, C. McLAUGHLIN AND J. GARRELS: *A sampling of the yeast proteome*, Molecular and Cellular Biology **19** (11): 7357–7368 (1999).
- [65] G. MULDER: *Über die Zusammensetzung einiger thierischen Substanzen*, Journal für Praktische Chemie **16** (1): 129–152 (1839).
- [66] D. PERRETT: *From „protein“ to the beginnings of clinical proteomics*, Proteomics. Clinical Applications **1** (8): 720–738 (2007).
- [67] P. WEBER, D. OHLENDORF, J. WENDOLOSKI AND F. SALEMME: *Structural origins of high-affinity biotin binding to streptavidin*, Science **243** (4887): 85–88 (1989).
- [68] A. HOLMBERG, A. BLOMSTERGREN, O. NORD, M. LUKACS, J. LUNDEBERG AND M. UHLEN: *The biotin-streptavidin interaction can be reversibly broken using water at elevated temperatures*, Electrophoresis **26** (3): 501–510 (2005).
- [69] „*Streptavidin Biotin binding*“, <http://upload.wikimedia.org/wikipedia/commons/5/5a/Streptavidin.png>. (Updatetd: 27 March 2015).
- [70] N. GREEN: *Avidin. 3. The nature of the biotin-binding site*, Biochemical Journal **89** (3): 599–609 (1963).
- [71] J. WONG, A. CHILKOTI AND V. MOY: *Direct force measurements of the streptavidin-biotin interaction*, Biomolecular Engineering **16** (1-4): 45–55 (1999).
- [72] M. DEODROWAŻPIRAMOWICZ, P. CZUBA, M. TARGOSZ, K. BURDA AND M. SZYMOŃSKI: *Dynamic force measurements of avidin-biotin and streptavidin-biotin interactions using AFM*, Acta Biochimica Polonica **53** (1): 93–100 (2006).
- [73] T. OSAKI, H. SUZUKI, B. LEPIOUFLE AND S. TAKEUCHI: *Multichannel simultaneous measurements of single-molecule translocation in alpha-hemolysin nanopore array*, Analytical Chemistry **81** (24): 9866–9870 (2009).
- [74] S. WILSON AND D. BERGSMAN: *Orphan G-protein coupled receptors: novel drug targets for the pharmaceutical industry*, Drug Design and Discovery **17** (2): 105–114 (2000).
- [75] L. BAKÁS, A. CHANTURIYA, V. HERLAX AND J. ZIMMERBERG: *Paradoxical Lipid Dependence of Pores Formed by the Escherichia coli  $\alpha$ -Hemolysin in Planar Phospholipid Bilayer Membranes*, Biophysical Journal **91** (10): 3748–3755 (2006).
- [76] S. CAVALIERI, G. BOHACH AND I. SNYDER: *Escherichia coli alpha-hemolysin: characteristics and probable role in pathogenicity*, Microbiological Reviews **48** (4): 326–343 (1984).
- [77] R. WELCH, E. DELLINGER, B. MINSHEW AND S. FALKOW: *Haemolysin contributes to virulence of extra-intestinal E. coli infections*, Nature **294** (5842): 665–667 (1981).

- [78] A. AKSIMENTIEV AND K. SCHULTEN: *Imaging alpha-hemolysin with molecular dynamics: ionic conductance, osmotic permeability, and the electrostatic potential map*, Biophysical Journal **88** (6): 3745–3761 (2005).
- [79] S. BHAKDI AND J. TRANUM-JENSEN: *Alpha-toxin of Staphylococcus aureus*, Microbiological Reviews **55** (4): 733–751 (1991).
- [80] E. GOUAUX: *alpha-Hemolysin from Staphylococcus aureus: an archetype of beta-barrel, channel-forming toxins*, Journal of Structural Biology **121** (2): 110–122 (1998).
- [81] S. BHAKDI, M. MUHLY, U. MANNHARDT, F. HUGO, K. KLAPETTEK, C. MUELLER-ECKHARDT AND L. ROKA: *Staphylococcal alpha toxin promotes blood coagulation via attack on human platelets*, The Journal of Experimental Medicine **168** (2): 527–542 (1988).
- [82] L. SONG, M. HOBAUGH, C. SHUSTAK, S. CHELEY, H. BAYLEY AND J. GOUAUX: *Structure of Staphylococcal alpha-Hemolysin, a Heptameric Transmembrane Pore*, Science **274** (5294): 1859–1865 (1996).
- [83] H. BAYLEY: *Pore-Forming Proteins with Built-in Triggers and Switches*, Bioorganic Chemistry **23** (4): 340–354 (1995).
- [84] M. RUSSO, H. BAYLEY AND M. TONER: *Reversible permeabilization of plasma membranes with an engineered switchable pore*, Nature Biotechnology **15** (3): 278–282 (1997).
- [85] J. MCNAMARA, G. WARNICK AND G. COOPER: *A brief history of lipid and lipoprotein measurements and their contribution to clinical chemistry*, Clinica Chimica Acta **369** (2): 158–167 (2006).
- [86] M. CHEVREUL, A. DIJKSTRA, G. LIST AND J. WISNIAK: *A chemical study of oils and fats of animal origin (1823)* (Sàrl Dijkstra-Tucker, France, 2009).
- [87] A. VON HÜBL: *Hübl's Methode zur Untersuchung der Fette*, Dingler's Polytechnisches Journal **253**: 281–295 (1884).
- [88] G. KNOTHE: *Structure indices in FA chemistry. How relevant is the iodine value?*, Journal of the American Oil Chemists' Society **79** (9): 847–854 (2002).
- [89] J. BERG, J. TYMOCZKO, L. STRYER AND G. GATTO: *Biochemie*, 7. Aufl. (Springer Spektrum, Heidelberg, 2013).
- [90] W. HOPPE AND R. BAUER: *Biophysics* (Springer-Verlag, Berlin, 1983).
- [91] P. YEAGLE: *The structure of biological membranes*, 3rd ed. (CRC Press, Boca Raton, 2012).
- [92] „Avanti Polar Lipids” - website, <http://avantilipids.com>. (Updated: 27 March 2015).
- [93] J. HANCOCK: *Lipid rafts: contentious only from simplistic standpoints*, Nature Reviews Molecular Cell Biology **7** (6): 456–462 (2006).
- [94] P. ALMEIDA: *The many faces of lipid rafts*, Biophysical Journal **106** (9): 1841–1843 (2014).
- [95] E.K. PALUCH: *Biophysical methods in cell biology, First edition* (Academic Press, London, 2015).
- [96] B. CASTRO, R.F. DE ALMEIDA, A. FEDOROV AND M. PRIETO: *The photophysics of a Rhodamine head labeled phospholipid in the identification and characterization of membrane lipid phases*, Chemistry and Physics of Lipids **165** (3): 311–319 (2012).
- [97] M. ANGELOVA AND D. DIMITROV: *Liposome electroformation*, Faraday Discussions of the Chemical Society **81**: 303 (1986).
- [98] D. DIMITROV AND M. ANGELOVA: *Lipid swelling and liposome formation mediated by electric fields*, Bioelectrochemistry and Bioenergetics **19** (2): 323–336 (1988).
- [99] P. WALDE, K. COSENTINO, H. ENGEL AND P. STANO: *Giant vesicles: preparations and applications*, ChemBiochem **11** (7): 848–865 (2010).
- [100] A. SAMAD, Y. SULTANA AND M. AQIL: *Liposomal drug delivery systems: an update review*, Current Drug Delivery **4** (4): 297–305 (2007).

- [101] T. CHA, A. GUO AND X.-Y. ZHU: *Formation of supported phospholipid bilayers on molecular surfaces: role of surface charge density and electrostatic interaction*, *Biophysical Journal* **90** (4): 1270–1274 (2006).
- [102] G. ROBERTS AND C. PITT: *Langmuir-Blodgett Films. Proceedings of the First International Conference on Langmuir-Blodgett Films* (Elsevier Science, Burlington, 1983).
- [103] B. FRANKLIN: *Of the Stilling of Waves by means of Oil*, *Philosophical Transactions of the Royal Society of London* **64** (0): 445–460 (1774).
- [104] A. POCKELS: *Surface Tension*, *Nature* **43**: 437 (1891).
- [105] A. POCKELS: *Relations Between the Surface-Tension and Relative Contamination of Water Surfaces*, *Nature* **48**: 152 (1893).
- [106] I. LANGMUIR: *The Constitution and fundamental properties of solids and liquids*, *Journal of the American Chemical Society* **38** (11): 2221–2295 (1916).
- [107] I. LANGMUIR: *The Constitution and fundamental properties of solids and liquids*, *Journal of the American Chemical Society* **39** (9): 1848–1906 (1917).
- [108] K. BLODGETT: *Monomolecular films of fatty acids on glass*, *Journal of the American Chemical Society* **56** (2): 495 (1934).
- [109] P. MARTIN, M. SZABLEWSKI AND F. GRUNFELD: *Tensionmeters and Langmuir-Blodgett Troughs*. NIMA Technology - Operating Manual 5th Edition (England, 1999).
- [110] G. ROBERTS: *Langmuir-Blodgett films* (Plenum Press, New York, 1990).
- [111] A. ASHKIN, J. DZIEDZIC, J. BJORKHOLM AND S. CHU: *Observation of a single-beam gradient force optical trap for dielectric particles*, *Optics Letters* **11** (5): 288 (1986).
- [112] D. GRIER: *A revolution in optical manipulation*, *Nature* **424** (6950): 810–816 (2003).
- [113] J. MOFFITT, Y. CHEMLA, S. SMITH AND C. BUSTAMANTE: *Recent advances in optical tweezers*, *Annual Review of Biochemistry* **77**: 205–228 (2008).
- [114] A. ASHKIN: *Acceleration and Trapping of Particles by Radiation Pressure*, *Physical Review Letters* **24** (4): 156–159 (1970).
- [115] A. ASHKIN: *Optical Levitation by Radiation Pressure*, *Applied Physics Letters* **19** (8): 283 (1971).
- [116] A. ASHKIN AND J. DZIEDZIC: *Optical trapping and manipulation of viruses and bacteria*, *Science* **235** (4795): 1517–1520 (1987).
- [117] A. ASHKIN, J. DZIEDZIC AND T. YAMANE: *Optical trapping and manipulation of single cells using infrared laser beams*, *Nature* **330** (6150): 769–771 (1987).
- [118] C. BUSTAMANTE, S. SMITH, J. LIPHARDT AND D. SMITH: *Single-molecule studies of DNA mechanics*, *Current Opinion in Structural Biology* **10** (3): 279–285 (2000).
- [119] C. KLEIMANN, A. SISCHKA, A. SPIERING, K. TÖNSING, N. SEWALD, U. DIEDERICHSEN AND D. ANSELMETTI: *Binding kinetics of bisintercalator Triostin a with optical tweezers force mechanics*, *Biophysical Journal* **97** (10): 2780–2784 (2009).
- [120] J. SLEEP, D. WILSON, R. SIMMONS AND W. GRATZER: *Elasticity of the Red Cell Membrane and Its Relation to Hemolytic Disorders: An Optical Tweezers Study*, *Biophysical Journal* **77** (6): 3085–3095 (1999).
- [121] Y. ARAI, R. YASUDA, K. AKASHI, Y. HARADA, H. MIYATA, K. KINOSITA AND H. ITOH: *Tying a molecular knot with optical tweezers*, *Nature* **399** (6735): 446–448 (1999).
- [122] D. RAUCHER, T. STAUFFER, W. CHEN, K. SHEN, S. GUO, J. YORK, M. SHEETZ AND T. MEYER: *Phosphatidylinositol 4,5-Bisphosphate Functions as a Second Messenger that Regulates Cytoskeleton-Plasma Membrane Adhesion*, *Cell* **100** (2): 221–228 (2000).

- [123] H. LIANG, W. WRIGHT, C. RIEDER, E. SALMON, G. PROFETA, J. ANDREWS, Y. LIU, G. SONEK AND M. BERNS: *Directed movement of chromosome arms and fragments in mitotic newt lung cells using optical scissors and optical tweezers*, *Experimental Cell Research* **213** (1): 308–312 (1994).
- [124] C. VEIGEL, L. COLUCCIO, J. JONTES, J. SPARROW, R. MILLIGAN AND J. MOLLOY: *The motor protein myosin-I produces its working stroke in two steps*, *Nature* **398** (6727): 530–533 (1999).
- [125] K. SVOBODA, P. MITRA AND S. BLOCK: *Fluctuation analysis of motor protein movement and single enzyme kinetics*, *Proceedings of the National Academy of Sciences of the United States of America* **91** (25): 11782–11786 (1994).
- [126] P. KORDA, M. TAYLOR AND D. GRIER: *Kinetically Locked-In Colloidal Transport in an Array of Optical Tweezers*, *Physical Review Letters* **89** (12) (2002).
- [127] Y. HARADA AND T. ASAKURA: *Radiation forces on a dielectric sphere in the Rayleigh scattering regime*, *Optics Communications* **124** (5-6): 529–541 (1996).
- [128] A. SISCHKA: *Kraftspektroskopie und Einzelmoleküldetektion mit der Optischen Pinzette*, Dissertation (2005).
- [129] K. SVOBODA AND S. BLOCK: *Biological Applications of Optical Forces*, *Annual Review of Biophysics and Biomolecular Structure* **23** (1): 247–285 (1994).
- [130] A. SPIERING: *Einzelmolekül-Experimente an Nanoporen mit der Optischen Pinzette*, Dissertation (2014).
- [131] S. KNUST, A. SPIERING, H. VIEKER, A. BEYER, A. GÖLZHÄUSER, K. TÖNSING, A. SISCHKA AND D. ANSEMETTI: *Video-based and interference-free axial force detection and analysis for optical tweezers*, *Review of Scientific Instruments* **83** (10): 103704 (2012).
- [132] A. RICHARDSON, S. REIHANI AND L. ODDERSHEDE: *Non-harmonic potential of a single beam optical trap*, *Optics Express* **16** (20): 15709–15717 (2008).
- [133] J. LAKOWICZ: *Principles of Fluorescence Spectroscopy*, Third Edition (Springer Science, Boston, 2006).
- [134] D. JAMESON: *Introduction to fluorescence* (CRC Press, Boca Raton, 2014).
- [135] B. VALEUR AND M. BERBERAN-SANTOS: *Molecular Fluorescence. Principles and applications*, 2nd ed. (Wiley-VCH, Weinheim, 2013).
- [136] F. LOTTSPEICH AND H. ZORBAS: *Bioanalytik* (Spektrum Akademischer Verlag, Heidelberg, 1998).
- [137] G. CHURCH, D. DEAMER, D. BRANTON, R. BALDARELLI AND J. KASIANOWICZ: *Characterization of individual polymer molecules based on monomer-interface interactions* (US Patent Nr: 5,795,782, 1998).
- [138] B. VENKATESAN AND R. BASHIR: *Nanopore sensors for nucleic acid analysis*, *Nature Nanotechnology* **6** (10): 615–624 (2011).
- [139] J. LI, D. STEIN, C. McMULLAN, D. BRANTON, M. AZIZ AND J. A. GOLOVCHENKO: *Ion-beam sculpting at nanometre length scales*, *Nature* **412** (6843): 166–169 (2001).
- [140] B. MILES, A. IVANOV, K. WILSON, F. DOČAN, D. JAPRUNG AND J. EDEL: *Single molecule sensing with solid-state nanopores: novel materials, methods, and applications*, *Chemical Society Reviews* **42** (1): 15 (2012).
- [141] S. LIU, T. YUZVINSKY AND H. SCHMIDT: *Effect of Fabrication-Dependent Shape and Composition of Solid-State Nanopores on Single Nanoparticle Detection*, *ACS Nano* **7** (6): 5621–5627 (2013).
- [142] N. PATTERSON, D. ADAMS, V. HODGES, M. VASILE, J. MICHAEL AND P. KOTULA: *Controlled fabrication of nanopores using a direct focused ion beam approach with back face particle detection*, *Nanotechnology* **19** (23): 235304 (2008).

- [143] J. YANG, D. FERRANTI, L. STERN, C. SANFORD, J. HUANG, Z. REN, L.-C. QIN AND A. HALL: *Rapid and precise scanning helium ion microscope milling of solid-state nanopores for biomolecule detection*, *Nanotechnology* **22** (28): 285310 (2011).
- [144] W. LI, N. BELL, S. HERNÁNDEZ-AINSA, V. THACKER, A. THACKRAY, R. BUJIDOSO AND U. KEYSER: *Single Protein Molecule Detection by Glass Nanopores*, *ACS Nano* **7** (5): 4129–4134 (2013).
- [145] S. WINTERS-HILT, W. VERCOUTERE, V.S. DEGUZMAN, D. DEAMER, M. AKESON AND D. HAUSSLER: *Highly Accurate Classification of Watson-Crick Basepairs on Termini of Single 5DNA6 Molecules*, *Biophysical Journal* **84** (2): 967–976 (2003).
- [146] G. MENESTRINA, N. MACKMAN, I. HOLLAND AND S. BHAKDI: *Escherichia coli haemolysin forms voltage-dependent ion channels in lipid membranes*, *Biochimica et Biophysica Acta* **905** (1): 109–117 (1987).
- [147] D. FOLOGEA, J. UPLINGER, B. THOMAS, D. McNABB AND J. LI: *Slowing DNA translocation in a solid-state nanopore*, *Nano Letters* **5** (9): 1734–1737 (2005).
- [148] F. DUMAS, M. LEBRUN AND J. TOCANNE: *Is the protein/lipid hydrophobic matching principle relevant to membrane organization and functions?*, *FEBS Letters* **458** (3): 271–277 (1999).
- [149] P. ESCRIBÁ, P. WEDEGAERTNER, F. GOÑI AND O. VÖGLER: *Lipid-protein interactions in GPCR-associated signaling*, *Biochimica et Biophysica Acta* **1768** (4): 836–852 (2007).
- [150] L.-Q. GU AND J. SHIM: *Single molecule sensing by nanopores and nanopore devices*, *The Analyst* **135** (3): 441–451 (2010).
- [151] N. BELL, C. ENGST, M. ABLAY, G. DIVITINI, C. DUCATI, T. LIEDLAND U. KEYSER: *DNA Origami Nanopores*, *Nano Letters* **12** (1): 512–517 (2012).
- [152] D. LUBENSKY AND D. NELSON: *Driven polymer translocation through a narrow pore*, *Biophysical Journal* **77** (4): 1824–1838 (1999).
- [153] G. SLATER, S. GUILLOUZIC, M. GAUTHIER, J.-F. MERCIER, M. KENWARD, L. McCORMICK AND F. TESSIER: *Theory of DNA electrophoresis (approximately 1999-2002(1/2))*, *Electrophoresis* **23** (22-23): 3791–3816 (2002).
- [154] P. REIMANN, A. MEYER AND S. GETFERT: *On the Lubensky-Nelson model of polymer translocation through nanopores*, *Biophysical Journal* **103** (5): 889–897 (2012).
- [155] T. BUTLER, M. PAVLENOK, I. DERRINGTON, M. NIEDERWEIS AND J. GUNDLACH: *Single-molecule DNA detection with an engineered MspA protein nanopore*, *Proceedings of the National Academy of Sciences of the United States of America* **105** (52): 20647–20652 (2008).
- [156] S. HADI ALIJANVAND AND H. MOBASHERI: *Biophysics of Polynucleotide Interactions with OmpF Nanopore Forming Protein, Possible Tool for DNA Sequencing*, *Biophysical Journal* **102** (3): 335a (2012).
- [157] M. PAVLENOK, I. DERRINGTON, J. GUNDLACH, M. NIEDERWEIS AND J. MATHE: *MspA Nanopores from Subunit Dimers*, *PLoS ONE* **7** (6): e38726 (2012).
- [158] R. WEI, T. MARTIN, U. RANT AND H. DIETZ: *DNA origami gatekeepers for solid-state nanopores*, *Angewandte Chemie* **51** (20): 4864–4867 (2012).
- [159] J. BURNS, E. STULZ AND S. HOWORKA: *Self-assembled DNA nanopores that span lipid bilayers*, *Nano Letters* **13** (6): 2351–2356 (2013).
- [160] M. LANGECKER, V. ARNAUT, T. MARTIN, J. LIST, S. RENNER, M. MAYER, H. DIETZ AND F. SIMMEL: *Synthetic lipid membrane channels formed by designed DNA nanostructures*, *Science* **338** (6109): 932–936 (2012).
- [161] A. SISCHKA, A. SPIERING, M. KHAKSAR, M. LAXA, J. KÖNIG, K.-J. DIETZ AND D. ANSELMETTI: *Dynamic translocation of ligand-complexed DNA through solid-state nanopores with optical tweezers*, *Journal of Physics: Condensed Matter* **22** (45): 454121 (2010).
- [162] W. ANSORGE: *Next-generation DNA sequencing techniques*, *New Biotechnology* **25** (4): 195–203 (2009).

- [163] J. WAIN AND E. MAVROGIORGOU: *Next-generation sequencing in clinical microbiology*, Expert Review of Molecular Diagnostics **13** (3): 225–227 (2013).
- [164] N. THOMSON, S. BAKER, D. PICKARD, M. FOKES, M. ANJUM, N. HAMLIN, J. WAIN, D. HOUSE, Z. BHUTTA, K. CHAN, S. FALKOW, J. PARKHILL, M. WOODWARD, A. IVENS AND G. DOUGAN: *The role of prophage-like elements in the diversity of Salmonella enterica serovars*, Journal of Molecular Biology **339** (2): 279–300 (2004).
- [165] D. LIVERMORE AND J. WAIN: *Revolutionising bacteriology to improve treatment outcomes and antibiotic stewardship*, Infection & Chemotherapy **45** (1): 1–10 (2013).
- [166] H. BAYLEY: *Nanopore sequencing: from imagination to reality*, Clinical Chemistry **61** (1): 25–31 (2015).
- [167] Y. YANG, R. LIU, H. XIE, Y. HUI, R. JIAO, Y. GONG AND Y. ZHANG: *Advances in nanopore sequencing technology*, Journal of Nanoscience and Nanotechnology **13** (7): 4521–4538 (2013).
- [168] Y. FENG, Y. ZHANG, C. YING, D. WANG AND C. DU: *Nanopore-based Fourth-generation DNA Sequencing Technology*, Genomics, Proteomics & Bioinformatics (DOI: 10.1016/j.gpb.2015.01.009) (2015).
- [169] Y. WANG, Q. YANG AND Z. WANG: *The evolution of nanopore sequencing*, Frontiers in Genetics **5**: 449 (2014).
- [170] N. LOMAN AND A. QUINLAN: *Poretools: a toolkit for analyzing nanopore sequence data*, Bioinformatics **30** (23): 3399–3401 (2014).
- [171] J. EDEL AND T. ALBRECHT: *Nanopores for bioanalytical applications. Proceedings of the international conference* (Royal Society of Chemistry, Cambridge, 2012).
- [172] G. SCHNEIDER, S. KOWALCZYK, V. CALADO, G. PANDRAUD, H. ZANDBERGEN, L. VANDERSYPEN AND C. DEKKER: *DNA translocation through graphene nanopores*, Nano Letters **10** (8): 3163–3167 (2010).
- [173] S. GARAJ, W. HUBBARD, A. REINA, J. KONG, D. BRANTON, AND J. A. GOLOVCHENKO: *Graphene as a subnanometre trans-electrode membrane*, Nature **467** (7312): 190–193 (2010).
- [174] C. MERCHANT, K. HEALY, M. WANUNU, V. RAY, N. PETERMAN, J. BARTEL, M. FISCHBEIN, K. VENTA, Z. LUO, JOHNSON, A. T. CHARLIE AND M. DRNDIĆ: *DNA translocation through graphene nanopores*, Nano Letters **10** (8): 2915–2921 (2010).
- [175] P. WADUGE, J. LARKIN, M. UPMANYU, S. KARAND M. WANUNU: *Programmed synthesis of freestanding graphene nanomembrane arrays*, Small **11** (5): 597–603 (2015).
- [176] S. HEEREMA, G. SCHNEIDER, M. ROZEMULLER, L. VICARELLI, H. ZANDBERGEN AND C. DEKKER: *1/f noise in graphene nanopores*, Nanotechnology **26** (7): 74001 (2015).
- [177] A. GIRDHAR, C. SATHE, K. SCHULTEN AND J.-P. LEBURTON: *Tunable graphene quantum point contact transistor for DNA detection and characterization*, Nanotechnology **26** (13): 134005 (2015).
- [178] S. NAM, I. CHOI, C.-C. FU, K. KIM, S. HONG, Y. CHOI, A. ZETTL AND L. LEE: *Graphene nanopore with a self-integrated optical antenna*, Nano Letters **14** (10): 5584–5589 (2014).
- [179] M. SUK AND N. ALURU: *Ion transport in sub-5-nm graphene nanopores*, The Journal of Chemical Physics **140** (8): 84707 (2014).
- [180] K. LIU, J. FENG, A. KIS AND A. RADENOVIC: *Atomically thin molybdenum disulfide nanopores with high sensitivity for DNA translocation*, ACS Nano **8** (3): 2504–2511 (2014).
- [181] W. LV, S. LIU, X. LI AND R. WU: *Spatial blockage of ionic current for electrophoretic translocation of DNA through a graphene nanopore*, Electrophoresis **35** (8): 1144–1151 (2014).
- [182] L. GALLA, A. MEYER, A. SPIERING, A. SISCHKA, M. MAYER, A. HALL, P. REIMANN AND D. ANSELMETTI: *Hydrodynamic Slip on DNA Observed by Optical Tweezers-Controlled Translocation Experiments with Solid-State and Lipid-Coated Nanopores*, Nano Letters **14** (7): 4176–4182 (2014).

- [183] R. PROBSTEIN: *Physicochemical Hydrodynamics: An Introduction*, Second Edition (John Wiley & Sons, New Jersey, 2003).
- [184] M. FIRNKES, D. PEDONE, J. KNEZEVIC, M. DÖBLINGER AND U. RANT: *Electrically Facilitated Translocations of Proteins through Silicon Nitride Nanopores*, *Nano Letters* **10** (6): 2162–2167 (2010).
- [185] K. BREUER: *Micro- and nanoscale diagnostic techniques* (Springer, New York, 2003).
- [186] H. VON HELMHOLTZ: *Studien über elektrische Grenzschichten*, *Annalen der Physik und Chemie* **7**: 338–382 (1879).
- [187] M. KOHONEN, M. KARAMAN AND R. PASHLEY: *Debye Length in Multivalent Electrolyte Solutions*, *Langmuir* **16** (13): 5749–5753 (2000).
- [188] C. GERTHSEN AND D. MESCHEDER: *Gerthsen Physik*. 22. Auflage (Springer, Berlin, 2004).
- [189] J. BERTHIER AND P. SILBERZAN: *Microfluidics for biotechnology* (Artech House, Boston, 2006).
- [190] S. GHOSAL: *Electrokinetic-flow-induced viscous drag on a tethered DNA inside a nanopore*, *Physical Review E* **76** (6): 61916 (2007).
- [191] Y. HE, M. TSUTSUI, C. FAN, M. TANIGUCHI AND T. KAWAI: *Controlling DNA translocation through gate modulation of nanopore wall surface charges*, *ACS Nano* **5** (7): 5509–5518 (2011).
- [192] S. BEHRENS AND D. GRIER: *The charge of glass and silica surfaces*, *The Journal of Chemical Physics* **115** (14): 6716 (2001).
- [193] D. STEIN, M. KRUTHOF AND C. DEKKER: *Surface-Charge-Governed Ion Transport in Nanofluidic Channels*, *Physical Review Letters* **93** (3) (2004).
- [194] B. KIRBY AND E. HASSELBRINK: *Zeta potential of microfluidic substrates: 1. Theory, experimental techniques, and effects on separations*, *Electrophoresis* **25** (2): 187–202 (2004).
- [195] D. HOOGERHEIDE, S. GARAJ AND J. GOLOVCHENKO: *Probing Surface Charge Fluctuations with Solid-State Nanopores*, *Physical Review Letters* **102** (25) (2009).
- [196] S. GHOSAL: *Electrophoresis of a polyelectrolyte through a nanopore*, *Physical Review E* **74** (4) (2006).
- [197] S. GHOSAL: *Effect of Salt Concentration on the Electrophoretic Speed of a Polyelectrolyte through a Nanopore*, *Physical Review Letters* **98** (23): 238104 (2007).
- [198] M. WANUNU, W. MORRISON, Y. RABIN, A. GROSBERG AND A. MELLER: *Electrostatic focusing of unlabelled DNA into nanoscale pores using a salt gradient*, *Nature Nanotechnology* **5** (2): 160–165 (2010).
- [199] B. LU, D. HOOGERHEIDE, Q. ZHAO AND D. YU: *Effective driving force applied on DNA inside a solid-state nanopore*, *Physical Review E* **86** (1) (2012).
- [200] B. LUAN AND A. AKSIMENTIEV: *Electro-osmotic screening of the DNA charge in a nanopore*, *Physical Review E* **78** (2): 21912 (2008).
- [201] J. SADER AND D. CHAN: *Long-Range Electrostatic Attractions between Identically Charged Particles in Confined Geometries and the Poisson–Boltzmann Theory*, *Langmuir* **16** (2): 324–331 (2000).
- [202] S. GETFERT, T. TÖWS AND P. REIMANN: *Reluctance of a neutral nanoparticle to enter a charged pore*, *Physical Review E* **88** (5) (2013).
- [203] V. A. PARSEGIAN: *Long-range physical forces in the biological milieu*, *Annual Review of Biophysics and Bioengineering* **2**: 221 (1973).
- [204] D. J. BONTHUIS, J. ZHANG, B. HORNBLOWER, J. MATHE, B. I. SHKLOVSKII AND A. MELLER: *Self-energy-limited ion transport in subnanometer channels*, *Physical Review Letters* **97**: 128104 (2006).

- [205] P. DAS: *DNA Methylation and Cancer*, Journal of Clinical Oncology **22** (22): 4632–4642 (2004).
- [206] M. BAZANT AND T. SQUIRES: *Induced-charge electrokinetic phenomena*, Current Opinion in Colloid & Interface Science **15** (3): 203–213 (2010).
- [207] S. KESSELHEIM, W. MÜLLER AND C. HOLM: *Origin of Current Blockades in Nanopore Translocation Experiments*, Physical Review Letters **112** (1): (2014).
- [208] J. H. MASLIYAH AND S. BHATTACHARJEE: *Electrokinetic and Colloid Transport Phenomena* (John Wiley & Sons, New York, 2006).
- [209] R.S. EISENBERG: *Computing the field in proteins and channels*, The Journal of Membrane Biology **150** (1): 1–25 (1996).
- [210] B. CORRY, S. KUYUCAK AND S.-H. CHUNG: *Tests of Continuum Theories as Models of Ion Channels. II. Poisson–Nernst–Planck Theory versus Brownian Dynamics*, Biophysical Journal **78** (5): 2364–2381 (2000).
- [211] J. D. JACKSON: *Classical Electrodynamics* (John Wiley & Sons, New York, 1998).
- [212] L. BOCQUET AND J.-L. BARRAT: *Flow boundary conditions from nano- to micro-scales*, Soft Matter **3** (6): 685 (2007).
- [213] S. KOWALCZYK, L. KAPINOS, T. BLOSSER, T. MAGALHÃES, P. VAN NIES, R. LIM AND C. DEKKER: *Single-molecule transport across an individual biomimetic nuclear pore complex*, Nature Nanotechnology **6** (7): 433–438 (2011).
- [214] P. J. HAGERMAN: *Flexibility of DNA*, Annual review of Biophysics and Biophysical Chemistry **17**: 265–286 (1988).
- [215] U. AEBI AND T. POLLARD: *A glow discharge unit to render electron microscope grids and other surfaces hydrophilic*, Journal of Electron Microscopy Technique **7** (1): 29–33 (1987).
- [216] W. HELLMICH: *Einzelzellanalytik in Mikrofluidik - Systemen*, Dissertation (2006).
- [217] U. KEYSER, J. VAN DER DOES, C. DEKKER AND N. DEKKER: *Optical tweezers for force measurements on DNA in nanopores*, Review of Scientific Instruments **77** (10): 105105 (2006).
- [218] A. SISCHKA, C. KLEIMANN, W. HACHMANN, M. SCHÄFER, I. SEUFFERT, K. TÖNSING, AND D. ANSELMETTI: *Single beam optical tweezers setup with backscattered light detection for three-dimensional measurements on DNA and nanopores*, Review of Scientific Instruments **79** (6): 63702 (2008).
- [219] C. DEUFEL AND M. WANG: *Detection of forces and displacements along the axial direction in an optical trap*, Biophysical Journal **90** (2): 657–667 (2006).
- [220] M. LANG, C. ASBURY, J. SHAEVITZ AND S. BLOCK: *An Automated Two-Dimensional Optical Force Clamp for Single Molecule Studies*, Biophysical Journal **83** (1): 491–501 (2002).
- [221] S. KNUST: *Video-based and interference-free axial force detection and analysis for optical tweezers*, Bachelor-Thesis (2012).
- [222] A. HONIGMANN, C. WALTER, F. ERDMANN, C. EGGELING AND R. WAGNER: *Characterization of horizontal lipid bilayers as a model system to study lipid phase separation*, Biophysical Journal **98** (12): 2886–2894 (2010).
- [223] H. SUZUKI, K. TABATA, Y. KATO-YAMADA, H. NOJI AND S. TAKEUCHI: *Planar lipid bilayer reconstitution with a micro-fluidic system*, Lab on a Chip **4** (5): 502–505 (2004).
- [224] M. MONTAL AND P. MUELLER: *Formation of Bimolecular Membranes from Lipid Monolayers and a Study of Their Electrical Properties*, Proceedings of the National Academy of Sciences of the United States of America **69** (12): 3561–3566 (1972).
- [225] D. AXELROD, D. KOPPEL, J. SCHLESSINGER, E. ELSON AND W. WEBB: *Mobility measurement by analysis of fluorescence photobleaching recovery kinetics*, Biophysical Journal **16** (9): 1055–1069 (1976).

- [226] D. SOUMPASIS: THEORETICAL ANALYSIS OF FLUORESCENCE PHOTOBLEACHING RECOVERY EXPERIMENTS, *Biophysical Journal* **41** (1): 95–97 (1983).
- [227] E. KALB, S. FREY AND L. TAMM: *Formation of supported planar bilayers by fusion of vesicles to supported phospholipid monolayers*, *Biochimica et Biophysica Acta* **1103** (2): 307–316 (1992).
- [228] T. STARR AND N. THOMPSON: *Formation and Characterization of Planar Phospholipid Bilayers Supported on TiO<sub>2</sub> and SrTiO<sub>3</sub> Single Crystals*, *Langmuir* **16** (26): 10301–10308 (2000).
- [229] T. M. BAYERLAND M. BLOOM: *Physical properties of single phospholipid bilayers adsorbed to micro glass beads. A new vesicular model system studied by <sup>2</sup>H-nuclear magnetic resonance*, *Biophysical Journal* **58** (2): 357–362 (1990).
- [230] C. MILLER, J. MAJEWSKI, T. GOG AND T. KUHL: *Characterization of Biological Thin Films at the Solid-Liquid Interface by X-Ray Reflectivity*, *Physical Review Letters* **94** (23): 238104 (2005).
- [231] B. LEWIS AND D. ENGELMAN: *Lipid bilayer thickness varies linearly with acyl chain length in fluid phosphatidylcholine vesicles*, *Journal of Molecular Biology* **166** (2): 211–217 (1983).
- [232] A. SISCHKA, L. GALLA, A. MEYER, A. SPIERING, S. KNUST, M. MAYER, A. HALL, A. BEYER, P. REIMANN, A. GOELZHAUSER AND D. ANSELMETTI: *Controlled Translocation of DNA Through Nanopores in Carbon Nano-, Silicon-Nitride- and Lipid-Coated Membranes*, *The Analyst* (DOI:10.1039/C4AN02319F) (2015).
- [233] U. KEYSER, S. VAN DORP AND S. LEMAY: *Tether forces in DNA electrophoresis*, *Chemical Society Reviews* **39** (3): 939–947 (2010).
- [234] S. KOWALCZYK, D. WELLS, A. AKSIMENTIEV AND C. DEKKER: *Slowing down DNA translocation through a nanopore in lithium chloride*, *Nano Letters* **12** (2): 1038–1044 (2012).
- [235] H. BRUUS: *THEORETICAL MICROFLUIDICS* (Oxford University Press, Oxford, 2008).
- [236] M. MISAKIAN AND J. KASIANOWICZ: *Electrostatic influence on ion transport through the alphaHL channel*, *The Journal of Membrane Biology* **195** (3): 137–146 (2003).
- [237] L. MOVILEANU, S. CHELEY AND H. BAYLEY: *Partitioning of Individual Flexible Polymers into a Nanoscopic Protein Pore*, *Biophysical Journal* **85** (2): 897–910 (2003).
- [238] B. SCHUSTER AND U. SLEYTR: *Single channel recordings of  $\alpha$ -hemolysin reconstituted in S-layer-supported lipid bilayers*, *Bioelectrochemistry* **55** (1-2): 5–7 (2002).
- [239] A. HALL, A. SCOTT, D. ROTEM, K. MEHTA, H. BAYLEY AND C. DEKKER: *Hybrid pore formation by directed insertion of  $\alpha$ -haemolysin into solid-state nanopores*, *Nature Nanotechnology* **5** (12): 874–877 (2010).
- [240] M. PETTY: *Langmuir-Blodgett films. An introduction* (Cambridge University Press, Cambridge, New York, 1996).
- [241] G. ROBERTS: *An applied science perspective of Langmuir-Blodgett films*, *Advances in Physics* **34** (4): 475–512 (2006).
- [242] A. SIMON, A. GIRARD-EGROT, F. SAUTER, C. PUDDA, N. PICCOLLET D'HAHAN, L. BLUM, F. CHATELAIN AND A. FUCHS: *Formation and stability of a suspended biomimetic lipid bilayer on silicon submicrometer-sized pores*, *Journal of Colloid and Interface Science* **308** (2): 337–343 (2007).
- [243] D. MARSH: *Lateral pressure in membranes*, *Biochimica et Biophysica Acta* **1286** (3): 183–223 (1996).
- [244] J. SPINK: *The transfer ratio of Langmuir-Blodgett monolayers for various solids*, *Journal of Colloid and Interface Science* **23** (1): 9–26 (1967).
- [245] I. MEY, M. STEPHAN, E. SCHMITT, M. MÜLLER, M. BEN AMAR, C. STEINEMAN AND A. JANSHOFF: *Local membrane mechanics of pore-spanning bilayers*, *Journal of the American Chemical Society* **131** (20): 7031–7039 (2009).

- [246] F. HEINEMANN AND P. SCHWILLE: *Preparation of micrometer-sized free-standing membranes*, *Chemphyschem* **12** (14): 2568–2571 (2011).
- [247] E. SACKMANN: *Supported Membranes: Scientific and Practical Applications*, *Science* **271** (5245): 43–48 (1996).
- [248] F. HARB, J. SARKIS, N. FERTE AND B. TINLAND: *Beyond Saffman-Delbruck approximation: a new regime for 2D diffusion of  $\alpha$ -hemolysin complexes in supported lipid bilayer*, *The European Physical Journal* **35** (11): 118 (2012).
- [249] A. MELLER AND D. BRANTON: *Single molecule measurements of DNA transport through a nanopore*, *Electrophoresis* **23** (16): 2583–2591 (2002).
- [250] J. MATHÉ, H. VISRAM, V. VIASNOFF, Y. RABIN, AND A. MELLER: *Nanopore unzipping of individual DNA hairpin molecules*, *Biophysical Journal* **87** (5): 3205–3212 (2004).
- [251] R. SMEETS, U. KEYSER, D. KRAPP, M.-Y. WU, N. DEKKER AND C. DEKKER: *Salt dependence of ion transport and DNA translocation through solid-state nanopores*, *Nano Letters* **6** (1): 89–95 (2006).
- [252] Y. RABIN AND M. TANAKA: *DNA in Nanopores: Counterion Condensation and Coion Depletion*, *Physical Review Letters* **94** (14): (2005).
- [253] H. CHANG, F. KOSARI, G. ANDREADAKIS, M. ALAM, G. VASMATZIS AND R. BASHIR: *DNA-Mediated Fluctuations in Ionic Current through Silicon Oxide Nanopore Channels*, *Nano Letters* **4** (8): 1551–1556 (2004).
- [254] S. RENNER, A. BESSONOV AND F. SIMMEL: *Voltage-controlled insertion of single  $\alpha$ -hemolysin and Mycobacterium smegmatis nanopores into lipid bilayer membranes*, *Applied Physics Letters* **98** (8): 83701 (2011).
- [255] B. LE PLOUFLE, H. SUZUKI, K. TABATA, H. NOJI, AND S. TAKEUCHI: *Lipid Bilayer Microarray for Parallel Recording of Transmembrane Ion Currents*, *Analytical Chemistry* **80** (1): 328–332 (2007).
- [256] V. STIMBERG, J. BOMER, I. VAN UITERT, VANDENBERG, ALBERT AND S. LE GAC: *High Yield, Reproducible and Quasi-Automated Bilayer Formation in a Microfluidic Format*, *Small* **9** (7): 1076–1085 (2013).

## Acknowledgments

---

An dieser Stelle möchte ich mich bei all den Personen bedanken, die mich während der Durchführung dieser Arbeit unterstützt und somit wesentlich zum Gelingen beigetragen haben.

Als erstes bedanke ich mich bei Herrn Prof. Dr. Dario Anselmetti für die freundliche Aufnahme in seine Arbeitsgruppe *Experimentelle Biophysik und Angewandte Nanowissenschaften* im Jahre 2008 und das entgegengebrachte Vertrauen nach meiner Bachelor- und Master-Arbeit auch hier promovieren zu dürfen. Ich erinnere mich gerne an viele konstruktive und anregende Gespräche und die aufgebrachte Geduld in Momenten, in denen die Experimente nicht so verliefen, wie wir uns das vorgestellt haben.

Herrn Prof. Dr. Andreas Hütten danke ich dafür, dass er bereits seit meiner Zeit als Bachelorstudent immer ein offenes Ohr für mich hatte und die Zweitkorrektur dieser Arbeit übernahm.

Ich bedanke mich des Weiteren bei Herrn Prof. Dr. Michael Meyer dafür, dass ich mir bei einem zweiwöchigen Aufenthalt in seiner Arbeitsgruppe an der University of Michigan unter Anleitung von Dr. Eric Yusko den Prozess des Beschichtens mittels einer Lipid-Doppelschicht aneignen durfte.

Auch bedanke ich mich bei Herrn Prof. Dr. Peter Reimann und Andreas J. Meyer von der Arbeitsgruppe Condensed Matter Theory an der Universität Bielefeld für die außerordentlich fruchtbare Kooperation und die vielen wertvollen Diskussionen, die dazu geführt haben, die experimentellen Ergebnisse mit dem theoretischen Modell in Einklang zu bringen.

Ganz besonders möchte ich mich bei den Herren Dr. Andy Sischka, Dr. André Spiering und Dr. Dominik Greif bedanken. Die beiden erstgenannten haben mich in die Welt der optischen Pinzette eingeführt und mir bei vielen Experimenten zur Seite gestanden. Besonders mit Dr. André Spiering hat die enge Zusammenarbeit nicht nur viel Freude bereitet, sondern auch zu tollen Resultaten geführt. Dr. Dominik Greif hat mich bereits in meiner Bachelor- und Masterzeit betreut und mir in vielen fachlichen Diskussionen immer weitergeholfen. Unter seiner Führung habe ich das grundlegende technische Handwerk für ein erfolgreiches Experimentieren mit Mikrofluidik-Strukturen und den Umgang mit biologischen Proben erlernt. Auch nach seiner Zeit als Doktorand in der Arbeitsgruppe blieb er stets für mich ansprechbar und ich hoffe, dass wir weiterhin so freundschaftlich verbunden bleiben.

Christoph Pelargus danke ich für das unermüdliche Bohren und Abbilden immer neuer Poren mit dem HIM und die Unterstützung bei technischen Fragen und Problemen jeglicher Art. Dr. Lukas Bogunovic danke ich für die große und oft spontane Unterstützung, wenn es um das Programmieren neuer LabView-Software ging, welche in vielen Experimenten erfolgreich zum Einsatz kam.

Bezüglich der Fortführung meiner Arbeiten danke ich Roland Hillmann für die gute Zusammenarbeit in meiner experimentellen Endphase und die spannenden Experimente, die wir zusammen mit der Bilayer Slide gemacht haben. Ich wünsche ihm weiterhin viel Erfolg und Geschick bei dem Umgang mit (bzw. "Zähmung von") den

Lipiden, die sich häufig nicht so verhielten, wie es gewünscht oder erwartet wurde. Auch unsere fröhliche Bürogemeinschaft in D1-250 wird mir in bester Erinnerung bleiben. Über die vielen Jahre durfte ich viel lernen, arbeiten, lachen, Pläne schmieden und Quatsch machen mit Dominik Greif, Lukas Bogunovic, Sven Proppert, Carina Vosskötter, Sonja Wegener, Niklas Biere, Benjamin Pape, Sükrü Akbaba und Sabrina Kißmer. Es war eine tolle Zeit mit euch!

Außerdem möchte ich mich bei allen anderen Mitgliedern dieser Arbeitsgruppe für die angenehme Arbeitsatmosphäre bedanken, da man bei Problemen stets ein offenes Ohr gefunden hat. Frau Dr. Katja Tönsing hat mir bei Fragen zu Lipiden und organisatorischen Dingen weitergeholfen, Frau Gabi Krome und später Frau Karin Lacey konnten mir in bürokratischen Angelegenheiten immer erklärend zur Seite stehen. Des Weiteren danke ich Mareike Dieding, Roland Hillmann und Alexander Harder dafür, dass sie fachlich sowie freundschaftlich immer für mich ansprechbar waren.

Es hat mir Spaß und Freude bereitet, mit den aufgeführten und allen anderen Kollegen zusammengearbeitet zu haben.

Für das Korrekturlesen dieser Arbeit und die vielen wertvollen Hinweise bedanke ich mich an dieser Stelle noch einmal bei Dr. Andreas Krupke, Dr. Sara Bender, Dr. Dominik Greif, Dr. Andy Sischka, Dr. Frank Wittbracht, Dr. Volker Walhorn und meiner Frau Daniela.

Bezüglich meiner grundlegenden Ausbildung danke ich recht herzlich meinem ehemaligen Physiklehrer Herrn Rainer Menze. Er hat mein großes Interesse an Themen der Physik und dem damit verbundenen Physik-Studium „verschuldet“.

Natürlich möchte ich mich ganz besonders bei meinen Eltern Renate und Uwe und meinen beiden älteren Brüdern Felix und Volker bedanken. Sie haben mich jederzeit auf meinem Weg unterstützt, mir den Rücken freigehalten und mir viele wertvolle Ratschläge geben können. Durch sie war es mir möglich, meinem Physik-Studium so zielstrebig nachzugehen, ohne den Spaß und die Freude am Leben zu vernachlässigen. Abschließend danke ich meiner Frau Daniela, dass sie immer hinter mir stand und mich vor allem nach kleineren Rückschlägen immer wieder aufgebaut hat. Außerdem bin ich ihr für ihr Verständnis hinsichtlich der unzähligen Überstunden dankbar, die sich vor allem im letzten halben Jahr des Zusammenschreibens angehäuft haben.

# Appendix

---

## I. List of Publications

- 2015 A. SISCHKA, **L. GALLA**, A.J. MEYER, A. SPIERING, S. KNUST, M. MAYER, A.R. HALL, A. BEYER, P. REIMANN, A. GÖLZHÄUSER AND D. ANSELMETTI: *Controlled translocation of DNA through nanopores in carbon nano-, silicon-nitride- and lipid-coated membranes*, *Analyst* (in press DOI:10.1039/C4AN02319F), (2015).
- 2014 **L. GALLA**, A.J. MEYER, A. SPIERING, A. SISCHKA, M. MAYER, A.R. HALL, P. REIMANN AND D. ANSELMETTI: *Hydrodynamic slip on DNA observed by optical tweezers-controlled translocation experiments with solid-state and lipid-coated nanopores*, *Nano Letters* **14** (7), 4176–4182, (2014).
- 2012 **L. GALLA**, D. GREIF, J. REGTMEIER AND D. ANSELMETTI: *Microfluidic carbon-blackened PDMS device with reduced UV background fluorescence for simultaneous two-color UV/VIS detection in single cell analysis*, *Biomicrofluidics* **6**, 014104, (2012).
- 2008 D. GREIF, **L. GALLA**, A. ROS AND D. ANSELMETTI: *Single cell analysis in full body quartz glass chips with native UV laser-induced fluorescence detection*, *Journal of Chromatography A* **1206** (1), 83-88, (2008).

## II. Contributions to Conferences

- 2014 **L. GALLA**, A.J. MEYER, A. SPIERING, S. KNUST, R. HILLMANN, A. SISCHKA, P. REIMANN AND D. ANSELMETTI: *Optical Tweezers: Single Molecule Translocation through Nanopores* (poster), International Workshop - Bilayer electrophysiology, München, (2014).
- 2014 **L. GALLA**, A.J. MEYER, A. SPIERING, S. KNUST, R. HILLMANN, A. SISCHKA, P. REIMANN AND D. ANSELMETTI: *Single Molecule Translocation through Nanopores Investigated with Optical Tweezers* (talk), NanoBioEurope, Münster, (2014).
- 2013 **L. GALLA**, A. SPIERING, L. BOGUNOVIC, M. MAYER, A. SISCHKA AND D. ANSELMETTI: *Nanopore modification with phospholipid bilayers for single molecule investigations* (poster), NanoBioTech, Montreux, (2013).
- 2013 A. SPIERING, **L. GALLA**, K. TÖSNING, A. BEYER, A. SISCHKA, A. GÖLZHÄUSER, M. MAYER AND D. ANSELMETTI: *Single Molecule Translocation through Surface-Modified Nanopores* (poster), Nanolayer Workshop, Bielefeld, (2013).
- 2011 **L. GALLA**, D. GREIF, J. REGTMEIER AND D. ANSELMETTI: *Carbon-blackened PDMS microfluidic chip for UV/VIS-LIF detection in single cell analysis with reduced UV background fluorescence* (poster), NanoBioTech, Montreux, (2011).
- 2011 **L. GALLA**, D. GREIF, J. REGTMEIER AND D. ANSELMETTI: *Single cell protein analysis via two-color UV/VIS laser induced fluorescence detection in microfluidic devices* (poster), DPG Spring Meeting, Dresden, (2011).
- 2011 **L. GALLA**, D. GREIF, D. ANSELMETTI AND J. REGTMEIER: *Microfluidic PDMS device with strong reduction of the UV background fluorescence for label-free protein separation and detection* (poster), MSB, San Diego, (2011).
- 2010 **L. GALLA**, D. GREIF, D. ANSELMETTI AND J. REGTMEIER: *Parallel UV/VIS laser induced fluorescence detection for cell protein fingerprinting in microfluidic devices* (poster), DGfB-Meeting, Bochum, (2010).
- 2009 **L. GALLA**, D. GREIF, J. REGTMEIER AND D. ANSELMETTI: *Reversible single bacterial cell positioning in microfluidic PDMS devices* (poster), DPG Spring Meeting, Dresden, (2009).
- 2008 D. GREIF, **L. GALLA**, A. ROS AND D. ANSELMETTI: *Native UV laser-induced fluorescence detection for single cell analysis in quartz glass chips with anisotropic microchannels* (poster), DGfB-Meeting, Berlin, (2008).

#### IV. Curriculum Vitae

##### LUKAS GALLA

Born in Bielefeld, Germany June 6th 1985, married

##### SCHOOL EDUCATION

- 1996 – 2005 HELMHOLTZ-GYMNASIUM, Bielefeld  
Degree: Abitur with commendation by the German Physical Society (DPG)
- 1992 – 1996 JOSEFSCHULE (Elementary School), Bielefeld

##### STUDIES

- 2005 – 2008 BACHELOR-STUDIES in Nanophysics at Bielefeld University  
Degree: Bachelor of Science (B.Sc.)
- 2008 BACHELOR-THESIS at Bielefeld University  
Subject: „*Untersuchung neuartiger Mikrofluidik-Strukturen für die Analyse des Quorum Sensing des Sinorhizobium meliloti auf Einzelzellniveau*“  
Chair of Experimental Biophysics and Applied Nanoscience (Prof. D. Anselmetti)
- 2008 – 2010 MASTER-STUDIES in Nanophysics at Bielefeld University  
Degree: Master of Science (M.Sc.)
- 2010 MASTER-THESIS at Bielefeld University  
Subject: „*Parallele UV/VIS-LIF Detektion für die Einzelzellanalyse an SF9 & CHO-Zellen*“  
Chair of Experimental Biophysics and Applied Nanoscience (Prof. D. Anselmetti)

##### PHD STUDIES

- 2011– 2015 PHD-STUDIES in Experimental Physics at Bielefeld University  
Subject: „*Nanopore Modifications with Lipid Bilayer Membranes for Optical Tweezers DNA Force Measurements*“  
Chair of Experimental Biophysics and Applied Nanoscience (Prof. D. Anselmetti)